

Distribution Agreement

In presenting this thesis or dissertation as a partial fulfillment of the requirements for an advanced degree from Emory University, I hereby grant to Emory University and its agents the non-exclusive license to archive, make accessible, and display my thesis or dissertation in whole or in part in all forms of media, now or hereafter known, including display on the world wide web. I understand that I may select some access restrictions as part of the online submission of this thesis or dissertation. I retain all ownership rights to the copyright of the thesis or dissertation. I also retain the right to use in future works (such as articles or books) all or part of this thesis or dissertation.

Signature:

Charles R. Packard

Date

Minimal Models of Flocking

By

Charles R. Packard
Doctor of Philosophy

Physics

Daniel Sussman, Ph.D.
Advisor

Gordon Berman, Ph.D.
Committee Member

Justin Burton, Ph.D.
Committee Member

Luiz Santos, Ph.D.
Committee Member

Allesandro Veneziani, Ph.D.
Committee Member

Accepted:

Kimberly Jacob Arriola, Ph.D.
Dean of the James T. Laney School of Graduate Studies

Date

Minimal Models of Flocking

By

Charles R. Packard
B.S., Temple University, PA, 2019

Advisor: Daniel Sussman, Ph.D.

An abstract of
A dissertation submitted to the Faculty of the
James T. Laney School of Graduate Studies of Emory University
in partial fulfillment of the requirements for the degree of
Doctor of Philosophy
in Physics
2025

Abstract

Minimal Models of Flocking

By Charles R. Packard

Living systems provide an abundance of fascinating examples of non-equilibrium collective motion, from microscopic vortices of swimming bacteria to macroscopic murmurations in flocks of starlings. Understanding the mechanics of how simple interactions between biological agents can give rise to rich, complex patterns of behavior is one of the central concerns of the field of active matter. A cornerstone of this field is the collection of flocking models which, although initially formulated to study the behavior of flocks of birds, have had their application extended to a diverse range of biological and synthetic systems across many orders of magnitude in length scale. My contributions to this sub-field that I present in this dissertation include: (1) resolving contradictory observations within the literature about the fundamental nature of the flocking transition, (2) discovering a flocking model which neatly connects disparate avenues of research on the effect of time-delayed interactions and non-reciprocal field theory, and (3) revealing a new regime of low-Reynolds-number systems that flocking models can be applied to. I conclude by discussing my preliminary work on systems of cooperatively interacting follower and leader cancer cells, and introduce computational pipeline for inferring models of their interactions. A series of theoretical and experimental studies that one can do build upon this preliminary work are outlined.

Minimal Models of Flocking

By

Charles R. Packard
B.S., Temple University, PA, 2019

Advisor: Daniel Sussman, Ph.D.

A dissertation submitted to the Faculty of the
James T. Laney School of Graduate Studies of Emory University
in partial fulfillment of the requirements for the degree of
Doctor of Philosophy
in Physics
2025

Acknowledgments

I am incredibly grateful to Daniel Sussman for being the greatest advisor I could have hoped for when entering graduate school. Even during the busiest and hardest of times, he always maintained a positive group culture and enabled me to focus on my research while also giving me freedom to explore everything that interested me. I also have to acknowledge the wonderful, collaborative office environment created by Toler Webb, Tomilola Obadiya, Chengling Li, Haicen Yue, and Helen Ansell. Each of them has made my time in graduate school not just productive but a genuinely delightful experience.

Contents

1	Introduction	1
1.1	The Surprising Usefulness of Simplistic Models of Complex Systems	2
1.2	Minimal Agent-Based Models of Flocking	4
1.3	Minimal Field Theory Models of Flocking	9
1.4	Coarse-Graining Agent-Based Models Into Field Theories	14
1.5	High-Complexity, Deep-Learning Models of Flocking	18
1.6	Structure of Dissertation	19
2	Banded Phases In Topological Flocks	22
2.1	Introduction	24
2.1.1	Order-Disorder Transition In Metric Flocks	24
2.1.2	Hydrodynamic Theory of Traveling Waves	26
2.1.3	Topological Field Theory	30
2.2	Results	31
2.2.1	Model	32
2.2.2	Coarse-Grained Fields Statistics	33
2.2.3	Shape of Propagating Bands	35
2.3	Conclusion	37
3	Flocks With Hierarchical Reaction Times	39
3.1	Introduction	41

3.1.1	Measurements of Time-Delayed Interactions in Flocks	42
3.1.2	Time-Delay Models	44
3.2	Results	46
3.2.1	Hierarchical Time Delay Model	46
3.2.2	Emergence of PT Symmetry Phase	47
3.2.3	Phase Separation In the PT-Symmetric State	49
3.2.4	Self-Assembled Spatial Organization of Agents	49
3.3	Conclusion	53
4	Flocking and Vortex Phases In <i>Bos Taurus</i> Sperm Cells	55
4.1	Introduction	56
4.1.1	Hydrodynamics of Micro-swimmers	56
4.1.2	Collective Sperm Motility	58
4.1.3	Pulse-Induced Vortex and Flocking States	59
4.2	Results	60
4.2.1	Inferring A Density-Dependent Transition Via Machine Learning	61
4.2.2	Density Fluctuation Statistics	63
4.2.3	Persistent Turning Particle Model	65
4.2.4	Vortex-Flocking Phase Diagram	67
4.3	Conclusion	67
5	Deep Learning the Heterogeneous Dynamics and Morphology of Fol-	
	lower/Leader Cancer Cells	70
5.1	Introduction	71
5.1.1	Follower and Leader Cell Heterogeneity	72
5.1.2	Minimal Models of Monolayer Migration	74
5.2	Methods	77
5.2.1	Force Inference Graph Neural Network	77

5.2.2	Trajectory Extraction	78
5.2.3	Proof of Concept	82
5.2.4	Application To Heterogeneous Follower and Leader Cell Populations	86
5.3	Phenotypic Heterogeneity of Follower and Leader Cells	86
5.3.1	Population Statistics	88
5.3.2	Image-Based Classification	90
5.4	Conclusion	93
6	Conclusions	95
	Appendix A Hidden Non-Reciprocity In The Vicsek Model	97
	Appendix B Coarse-Graining The Vicsek Model	100
	Appendix C Non-Reciprocal Fluctuation Renormalization	104
C.1	Introduction	104
C.2	Perturbation expansion of equations of motion	105
C.3	Renormalized field dynamics	106
C.4	Renormalized free energy	108
C.5	Fluctuation expansion of non-reciprocal hydrodynamic corrections . .	110
C.6	Non-reciprocal corrections to renormalized hydrodynamics	114
C.6.1	Computation of correlators near the critical point	114
	Bibliography	119

List of Figures

1.1	Macroscopic and microscopic flocks. (a) Flock of starlings (image taken by Grahame Hopwood and borrowed from linestrust.org). (b) Swarming <i>Paenibacillus dendritiformis</i> bacteria [8].	2
1.2	Snapshots of Vicsek model flocks. Representative snapshots of a flocking state in the Vicsek model and a state close to criticality are shown in (a) and (b) respectively. Figures taken from Ref. [55].	4
1.3	Number fluctuation measurements in 2D and 3D flocking systems. (a) An example of how number fluctuations, δN , are measured from a configuration of particles using (red) sub-volume bins that contain an increasingly large expected number of particles, $\langle N \rangle$ (figure taken from Ref. [43]). (b) Number fluctuation scaling data for Vicsek model simulations in 2D and 3D [21], active colloidal particles [57], wild type <i>Bacillus subtilis</i> colonies in 2D [138], <i>Escherichia coli</i> colonies in 3D [68]. Inset shows scaling data for each system with fits to Eq. 1.9, while the main panel shows a scaling collapse with normalization by the fitting parameter A . Dashed black line in the main panel denotes a fit to the power-law $\langle N \rangle^{0.8}$	7

1.4	Cluster size distributions in 2D flocking systems. (a) Schematic example of four clusters of sizes 1, 2, 7, and 8 in the active Voronoi model (Figure taken from Ref. [54]). (b) The probability distribution of finding a cluster with n agents for the Vicsek model [21], active Voronoi model [54], active colloidal particles [59], wild type <i>Bacillus subtilis</i> colonies [138], colonies of <i>Serratia marcescens</i> [25] (all in 2D). Inset shows distribution data for each system with fits to the function $p(n) \propto A n^{-\zeta}$, and the main panel shows the scaling collapse.	8
1.5	Velocity fluctuations in a starling flock. Instantaneous state of individual birds within a starling flock of 1246 birds occupying a space with linear size $L = 36.5 m$ (a) The velocity vectors are shown and indicate that the flock is strongly ordered. (b) The individual velocity fluctuations, away from the global orientation in (a), are shown. Two large domains of strongly correlated birds are clearly visible. (Figure taken from Ref. [19]).	12
1.6	Anisotropic sound speed in a flock. Measured values of sound speeds (circles) at different orientations relative to the spontaneously selected flocking direction of a system are fit to the functional form of $c_{\pm}(\theta)$ predicted by Toner-Tu theory (solid lines).. (a) Sound speeds from a Vicsek model simulation are plotted in a Cartesian coordinate system (Figure taken from Ref. [122]) (b) Sound speeds from an active colloid experiment are plotted in a polar coordinate system (Figure taken from Ref. [41]). I note that the functional form being fit in both (a) and (b) is the same, and its shape simply changes depending on the effective values of the transport coefficients in the Toner-Tu descriptions of the flocks.	13

2.1 **Metric versus topological interactions.** (a) A time-lapse of two microtubules colliding and aligning their orientations (figure taken from Ref. [107]). An image of cells in an epithelial monolayer, where the cell nuclei are green and the cell-cell contacts are colored red and yellow (figure taken from Ref. [12]). 23

2.2 **Phase transition in the metric Vicsek model.** Numerical results are shown from simulations of the Vicsek model (Eqs. 1.1-1.2). (a) Schematic example of metric alignment interactions in the Vicsek model, where a (red) particle only aligns with neighbors within an interaction radius R_0 . (b) The critical noise strength (η_c) at which the order-disorder transition takes place is shown as a function of average global particle density; increasing density allows flocking phases to survive at larger noise strengths. (c) A snapshot of a large-scale simulation in the vicinity of the critical point η_c at a density of $\rho = 2$; spontaneously assembled meso-scale waves propagate through a background of disordered particles in the direction denoted by the red arrow. Figures taken from Refs. [21, 43]. 25

2.3 **Propagating waves in an active colloid suspension.** Experimental data for a system of self-propelled colloids. (a) Image of experimental setup, in which colloids have self-organized into a propagating wave around a circular track. (b) Particles in the space far away from the front of a propagating wave have a low density and are disordered. (c) The wave front is characterized by a phase separation between low-density/disordered and high-density/ordered states. (d) Within the propagating band, particles collectively flow together along the track. (e) The transition from homogeneously disordered to ordered states, with the intermediate phase coexistence regime, is shown as a function of colloid packing fraction (Φ_0). (f) A schematic representation of how active colloids become self-propelled via the Quincke instability in the presence of an external electric field (E); the torque generated by an unevenly distributed charge on the particle's surface overcomes the restoring torque of the electric field, leading to a translational speed U . Figures taken from Ref. [16, 14]. 27

2.4 **Density statistics of topological flocks.** (a) The distribution of different measurements of the polar order parameter field (Eq. 1.11) as a function of local density (Eq. 1.3) is shown for Vicsek model simulations with Voronoi (topological) and metric neighbors. (b) Giant number fluctuation scaling measurements at increasing system sizes, $L = 64, 128, 256$, with the dashed red line denoting a fit to the power law $\propto \langle n \rangle^{0.88}$. Figures taken from Ref. [44]. 31

2.5 **Order parameter distributions across the transition.** The probability density function, $p(\phi)$ of the polar order parameter field (Eq. 1.11) when computed using square bins with varying linear size ℓ are shown in the (a) disordered phase, (b) critical point, and (c) ordered phase. Simulation parameters are $v_0 = 2.0$ and $dt = 5 \times 10^{-3}$ 33

2.6 **Coarse-grained fields of a topological flock at criticality.** The density (ρ) and order parameter (ϕ) fields are computed from a single simulation snapshot in square bins of linear size ℓ . Simulation parameters are $v_0 = 2.0$ and $dt = 5 \times 10^{-3}$. These parameter values were chosen minimize the time for the simulation to converge to its steady-state. 34

2.7 **Structure of bands in topological flocks.** The time-average density field profiles (Eq. 2.5) for a system with $v_0 = 2.0$ and $v_0 = 0.5$ are shown in (a) and (b) respectively with solid black lines. The solid red lines denote fits to the phase-separated (Eq. 2.12) and soliton-like (Eq. 2.13) profiles predicted by Toner-Tu theory. 35

2.8 **Sensitivity of banded phases to time-step size.** The value of the banding order parameter (Eq. 2.17) is computed at various noise strengths across the phase transition for the density (ρ) and polar order parameter (ϕ) fields. Black data denotes simulations with $dt = 0.005$, and light blue data denotes simulations with $dt = 1.000$ 36

3.1 **Fore-aft non-reciprocity.** A schematic example of how a limited vision cone leads to fore-aft asymmetry between interacting agents within a flock. (a) An example of the possible neighbors for a single agent within a flock (b) Agent i interacts with j , but not vice-versa due to a limited vision cone. Figure taken from Ref. [35]. 40

3.2 **Hierarchical time-delayed interactions in pigeons.** (a) The trajectory of a small flock of GPS-carrying pigeons is shown, with different bird trajectories denoted by different colors. (b) Using trajectory data from (a) to compute velocities in Eq. 3.1, the interaction network between the pigeons is shown, with the inferred reaction time (τ_{\max}) labeling each pair (i, j) . Figure taken from Ref. [76]. 43

3.3 **Transition from flocking to PT-symmetric phase.** Simulation snapshots of the density (ρ) and transverse velocity (v_{\perp}) fields are shown on the top and bottom respectively. The transverse velocity field corresponds fluctuations in particle orientations away from the direction of global flocking (r_{\parallel}). Snapshots of the Toner-Tu flocking phase ($\eta = 0.10$) are shown in (a) and (c), and snapshots of the PT-symmetric phase ($\eta = 0.01$) are shown in (b) and (d). 48

3.4 **Emergence of non-Gaussian statistics.** (a) Probability density function of single particle orientations relative to the global flocking direction. (b) Binder cumulant, $U_L = 1 - \langle \theta_i^4 \rangle / 3 \langle \theta_i^2 \rangle^2$, is shown for system sizes $N = \{2^{11}, 2^{12}, 2^{13}, 2^{14}, 2^{15}, 2^{16}, 2^{17}\}$. In the flocking phase θ_i is normally distributed and $U \approx 0$, and deviations away from $U = 0$ denote non-Gaussianity. 50

3.5	Spontaneous ordering of time-delays.	(a) The response of our model to an instantaneous re-ordering of particle indices within our sequential update algorithm (described in Sec. 3.2.1) is shown at high noise strengths (red/orange) in the flocking phase, and low noise strengths (blue/purple) in the PT-symmetric phase. (b) Time-averaged profile of the transverse velocity field is denoted with the solid black line, and the profile of the non-reciprocal force field (Eq. 3.10) is denoted by the solid purple line. Dashed yellow lines indicate the positions of the interfaces between the counter-propagating bands of the PT-symmetric phase. Data was collected for a system of $N = 320000$ particles at a noise strength of $\eta = 0.005$	51
4.1	Vortex-forming behavior of pusher micro-swimmers.	(a) The effective viscosity (η_p) relative to the solvent viscosity (η_0) for <i>Escherichia coli</i> at different packing fractions (ϕ) and fixed shear rate ($\dot{\gamma}$) [69]. (b) Velocity field of a suspension of ram sperm cells; note that the vortices are all rotating counter-clockwise (i.e. there is a preferred chirality). Scale bar is $200 \mu m$ [30].	57
4.2	Viscoelastic fluid induced clustering.	A representative image of sperm cells moving in (a) an ordinary, Newtonian fluid and (b) a viscoelastic fluid. Scale bar is $50 \mu m$ (Figure taken from Ref. [124]).	59
4.3	Pulse-induced collective motion states.	Representative snapshots of the flocking (a) and vortex (b) states that arise when a transient hydrodynamic pulse is applied to a disordered suspension of sperm cells. White outlines denote cell segmentations, and blue arrows denote the tail-to-head orientation of each cell (Figure taken from Ref. [82]).	60

4.4	Vortex to flocking transition. The time-averaged polar order parameter and enstrophy are shown as a function of average global density for suspensions of sperm cells like those in Fig. 4.3. Each color here corresponds to a different experimental sample, and dashed lines in (a) denote fits to hyperbolic tangent functions.	62
4.5	Density fluctuation scaling in flocking states. Data shown here was obtained from flocks of sperm cells with the largest polar order values (highest densities) from Fig. 4.4. (a) The giant number fluctuation scaling is shown when fluctuations are computed within boxes of aspect ratio β (Eq. 4.2); for each value of β , the scaling was fit to Eq. 4.1, and the value of K' is plotted in the inset. (b) Density fluctuation correlation function measured in boxes separated by a distance $ \delta\mathbf{r} $ parallel to the flocking direction, $\delta\mathbf{r} = \delta\mathbf{r} \mathbf{e}_{\parallel}$ (black), and boxes separated in the transverse direction, $\delta\mathbf{r} = \delta\mathbf{r} \mathbf{e}_{\perp}$ (blue). The prediction from Eq. 4.4 is denoted by the dashed grey line.	64
4.6	Experimental and model trajectories. (a) Trajectories of dilute, isolated cells from our experiments. (b) Trajectories from our simulations of Eqs. 2.14,4.5,4.6 that were fit to the experimental data. . . .	66
4.7	Vortex to flocking phase diagram. The same data as in Fig. 4.4 is shown here, but with polar and vortex order parameters now shown as a function of both cell density and persistence time. Dashed black line denotes the order-to-disorder transition line obtained from simulations of Eqs. 4.5-4.6.	67

5.1	Schematic diagram of the role LCs play in cancer invasion.	
	Pericellular proteolysis is used to degrade the ECM and then forcibly deform the ECM in order to create spaces for them to elongate into. LCs also deposit matrix components such as fibronectin as they generate low-resistance tracks, which provides adhesion sites that enhance follower cells mobility (Figure taken from Ref. [128]).	71
5.2	Functional role of leaders. Snapshots of three different tumors composed of all follower cells except for a leader cell population fraction of 0%, 1% and 10% in (a)-(c) respectively. Images are taken 48 hours after spheroid are initially implanted in an extra cellular matrix composed of collagen. Figures taken from Ref. [62].	73
5.3	Functional role of followers. Pie charts show how often follower and leader cells (in isolation) make mitotic errors. Follower cells rarely make errors during cell division, while leaders are plagued by instabilities that result in cell death. Figures taken from Ref. [62].	74
5.4	Agent-based and hydrodynamic models of leader-cell invasion. (a) Simulation snapshot of a variant of Eqs. 5.1-5.2, showing local polarization of ‘bulk’ cells and protruding streams of cells. (b) Schematic of a minimal hydrodynamic model of multi-cellular streaming. Figures taken from Ref. [99] and Ref. [133] respectively.	75
5.5	Graph construction. Schematic example of how (a) an ensemble of simple particles are mapped to an all-to-all graph in Ref. [29], and (b) an monolayer of cells are mapped to a Voronoi graph in our work (white lines denote graph edges and orange arrows denote cell velocities).	79

5.6	Example of segmentation and tracking in a 2D monolayer.	
	(left) A snapshot of a monolayer of cells from an experiment is shown with the cytoplasm boundary contours predicted by a segmentation model shown in bright green. (right) The computationally tracked trajectory of each cell contour from the left plot is shown here, denoted by sequences of randomly colored circles at cells' centroids.	79
5.7	Quantifying cell-cell contact. While pixels denote the contours of cell nuclei in a monolayer. Green pixels denote the points that are shared between two cells.	81
5.8	Fitting cell shape to an ellipsoid. (left) a plot of the eccentricity (e) of a cell as a function of the ratio of its minor axis (b) to its major axis (a), with example plots of the ellipse at representative values of b/a . (right) Fits of to segmented cells to ellipses are denoted by red lines, with the corresponding eccentricity displayed on top.	82
5.9	Correlation between model predictions and observed values. The ability of performance of a model (Eq. 5.17) at predicting in a cell's velocity within a time-interval dt is shown. Predicted values are shown on the y -axis, and true values on the x -axis.	83
5.10	Results of training GNNs on experimental data. (a) The loss function and correlation coefficients of models trained via Eq. 5.17 are shown as a function of time-step size; correlation coefficients correspond to the same type of measurements as in Fig. 5.9. (b) A plot of the true cell velocities (green) and the predicted cell velocities (red) for the model with a value of $dt = 20$ that had the lowest loss value in (a). Note that cells which do not have red arrows correspond to cells that the segmentation and tracking packages were unable to track for the duration of the time interval $[t - dt, t + dt]$	84

5.11 **Learned pair-wise interaction.** The x and y components of the learned force (Eq. 5.15) for the optimal value of dt in Fig. 5.10 is shown on the left and right respectively. The y -axis is scaled by the average linear size of a cell (ℓ_0), and the x -axis is scaled by the characteristic speed $v_0 = \ell/dt$ 85

5.12 **Heterogeneity in follower and leader cell shapes.** Representative snapshots of follower and leader cells in pure, isolated populations are shown in (a) and (b) respectively. Note that leaders in (b) tend to be more elongated on average. Figure taken from Ref. [62]. 87

5.13 **Area and eccentricity statistics.** Data shown was collected from pure populations of either entirely follower (green) or entirely leader (red) cells. Top row shows data for the cross sectional areas of cells, where solid circles denote experimental data and dashed lines denote fits to Eq. 5.18. Middle row shows data for the eccentricity of cells, as defined in Fig. 5.8. The bottom row shows representative examples of the different cell configurations. 89

5.14 **Schematic diagram of classifier model.** We use a ResNet50 backbone that has been pre-trained on the *imagenet* dataset to detect a diverse range of features. Dense, fully-connected layers are then appended to the model to learn how to combine the features to predict the species of a cell. Figure taken from Ref. [126]. 91

5.15 **Cross validation of image classifier model.** The classification accuracy of a model trained on one day and tested on another day is listed for all possible pairs. Training accuracy is denoted by the diagonal elements. 92

5.16	Correlation between shape and dynamics. The average orientational alignment between a cell's axis of elongation (\mathbf{n}_i) with its instantaneous velocity vector (\mathbf{v}_i) for follower (F) and leader (L) cells at different values of eccentricity (as defined in Fig. 5.8).	94
C.1	The correlators in Eqs. C.73 and C.75 are plotted here to leading order in α	118

Chapter 1

Introduction

The collective motion of living systems, from the synchronized flight of starling flocks (Fig. 1.1a) to the coordinated migration of bacterial colonies (Fig. 1.1b), present striking examples of how large-scale order can emerge from simple local interactions. Despite the vast differences in scale and biological complexity, these systems share fundamental physical principles: organisms consume internally stored energy to maintain motility and align their motion with that of their neighbors (either by choice or by passive forces, such as steric interactions in the case of bacteria). This combination of behaviors is observed across a diverse range of systems – from microscopic scales in microtubules [107], cells [113], and spermatozoa [96], to macroscopic systems of worms [106] and sheep [46] – and raises a central question: can we construct minimal models that capture the essence of collective behavior without the full complexity of biological details? If so, what features are indispensable for emergent order, and which are incidental? To address these questions, physicists have developed agent-based models that distill flocking dynamics into basic alignment rules while coarse-graining system-specific details. When combined with field theories, these models provide a powerful framework for understanding non-equilibrium phenomena and universality classes in active matter systems¹. This chapter introduces the foundational models of

¹Active matter systems are those in which the constituent agents are self-propelled.

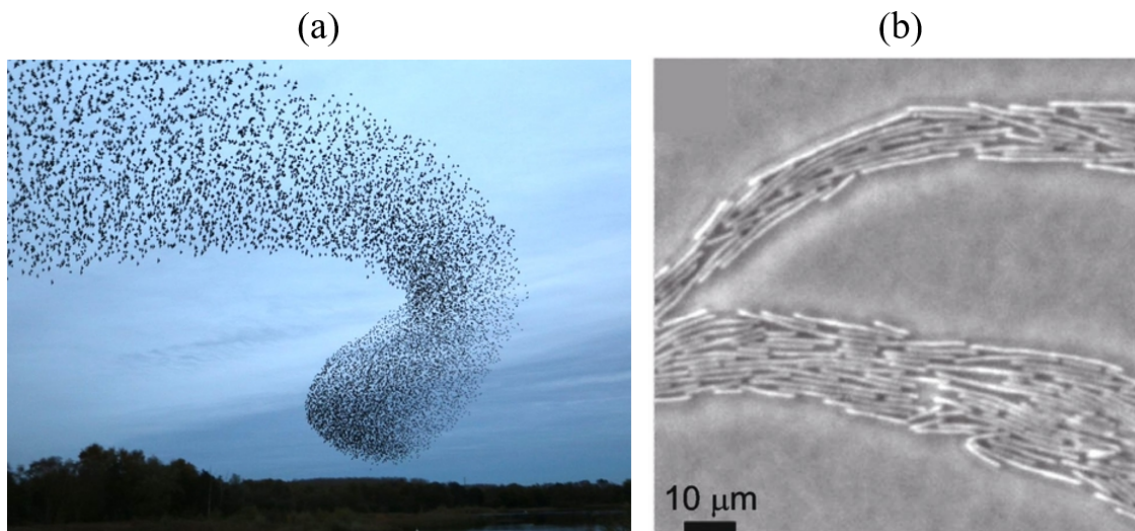


Figure 1.1: **Macroscopic and microscopic flocks.** (a) Flock of starlings (image taken by Grahame Hopwood and borrowed from linestrust.org). (b) Swarming *Paenibacillus dendritiformis* bacteria [8].

flocking, presents empirical evidence for universal behavior across living systems, and explores how coarse-grained theories bridge the gap between microscopic interactions and macroscopic collective motion.

1.1 The Surprising Usefulness of Simplistic Models of Complex Systems

When modeling complex systems composed of many interacting particles, there is always a trade-off between capturing the intricate details of a particular system and identifying the broader behavior of an entire class of systems. A well-known example of this trade-off comes from statistical physics, where different models of magnetism provide varying levels of detail and generality. At one extreme, density functional theory resolves the quantum-mechanical interactions of electrons, allowing for highly precise, material-specific predictions of magnetic properties [129]. However, this precision comes at a computational cost that makes it impractical for studying large-scale

statistical behavior. At the opposite end of the modeling spectrum, the Ising model abstracts away microscopic complexity, representing atomic-scale interactions as effective binary spins ($\sigma_i = \pm 1$) that interact via a simple energy function. Despite its simplicity, the Ising model successfully predicts universal properties of phase transitions, such as the emergence of ferromagnetism and the scaling of magnetization fluctuations near criticality [60].

A similar philosophy underlies models of fluid phase transitions. The van der Waals model for example, a mean-field description of gases composed of particles with finite volume and weak attractive forces, captures key macroscopic behaviors of liquid-gas coexistence, such as critical compressibility, while ignoring the atomic-level intricacies of intermolecular forces. The power of such simplified models lies in their ability to isolate the essential ingredients necessary to produce emergent behaviors. By focusing on general properties – such as dimensionality and symmetries – they provide deep insights into systems that would otherwise be computationally intractable or analytically unsolvable in full microscopic detail.

This same approach has proven invaluable in the study of active matter, i.e. systems composed of self-propelled agents such as birds, bacteria, or cells. The precise interactions governing these biological agents are highly complex, involving biochemical signaling, mechanical forces, and environmental feedback. Yet, by reducing individuals to simple, point-like agents that follow basic alignment rules, minimal models of flocking successfully capture the onset of collective motion across vastly different biological contexts [113, 107, 22, 106, 130]. Rather than attempting to model every microscopic detail, these coarse-grained descriptions highlight universal behaviors, providing not only a tractable framework for theoretical analysis but also a means to draw connections between seemingly disparate systems. In the following section, we introduce one such minimal model for studying flocking behavior, which serves as a foundational tool in understanding non-equilibrium phase transitions and exemplifies

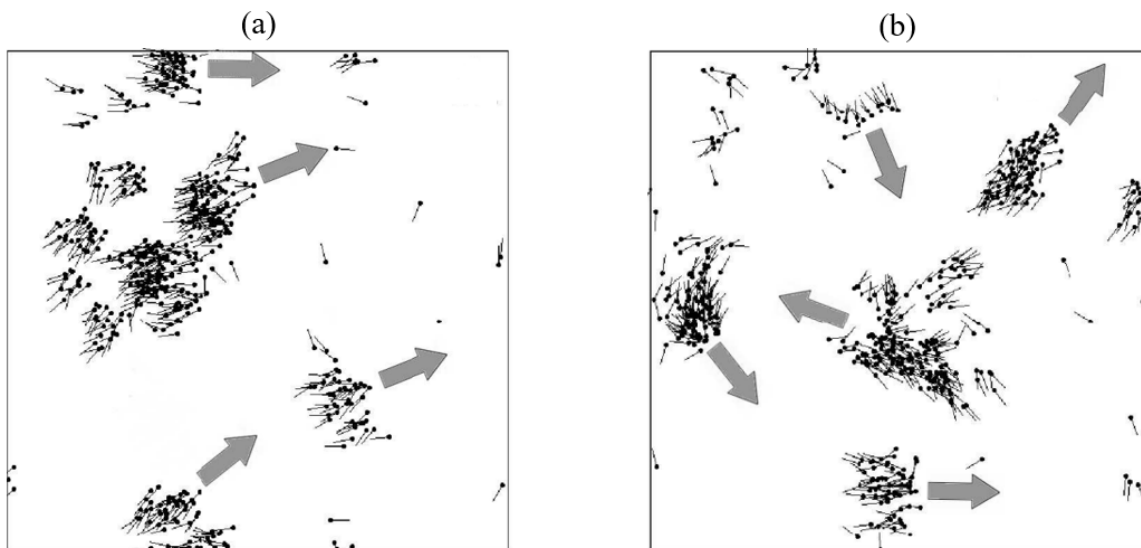


Figure 1.2: **Snapshots of Vicsek model flocks.** Representative snapshots of a flocking state in the Vicsek model and a state close to criticality are shown in (a) and (b) respectively. Figures taken from Ref. [55].

how simple rules at the microscopic scale can give rise to rich macroscopic phenomena in active matter systems.

1.2 Minimal Agent-Based Models of Flocking

The earliest work on modeling complex bird flocks as simple interacting particles did not originate from physics but rather from computer graphics. Reynolds' pioneering work introduced a computational model in which each 'boid' – a particle-like representation of a bird – follows a minimal set of behavioral rules: (1) avoid collisions, (2) match the velocity of neighbors, and (3) remain near the group [95]. Despite its simplicity, this model produced visually striking collective motion, mimicking the large-scale coordination observed in real flocks. However, visual similarity alone does not confirm that a model accurately captures the physical principles governing real-world flocking. A key scientific question is whether a flock composed of thousands of interacting boids' exhibits the same statistical and dynamical properties as biological flocks.

This question has been probed in the Vicsek model, a simplified but powerful theoretical framework for understanding collective motion in biological systems [127]. The Vicsek model refines Reynolds' approach by removing specific behavioral heuristics and instead describing agents as self-propelled particles governed by simple alignment interactions. In this model, all agents move under their own propulsion at a constant speed v_0 , such that their positions evolve in time according to

$$\mathbf{r}_i(t+1) = \mathbf{r}_i(t) + v_0 \hat{\mathbf{n}}_i(t), \quad (1.1)$$

where the unit vector $\hat{\mathbf{n}}_i$ represents the instantaneous orientation of the i^{th} particle. Note that time is discretized and that v_0 sets the only time-scale in the microscopic dynamics. Choosing length-scales such that each agent has a length of $\ell = 1$, then ℓ/v_0 sets the time-scale at which a particle will travel one full body length. Unlike in biological systems, where locomotion may involve flapping wings, swimming in a fluid, or crawling on a substrate, these details are intentionally coarse-grained away in Eq. 1.1. Instead, the essential ingredient is that each agent consumes energy to maintain self-propulsion, keeping the system in a non-equilibrium state.

The orientations of agents evolve by aligning with their local neighbors, subject to noise, such that

$$\hat{\mathbf{n}}_i(t+1) = \hat{N} \circ [\langle \hat{\mathbf{n}}_j(t) \rangle + \boldsymbol{\eta}_i(t)] \quad (1.2)$$

where \hat{N} is an operator that normalizes its argument to a unit vector, and $\boldsymbol{\eta}_i$ is a random Gaussian white noise term that introduces stochastic fluctuations. When noise is small relative to alignment interactions, the system undergoes a spontaneous symmetry-breaking transition: agents develop a 'global flocking direction' in which collective motion emerges (Fig. 1.2).

One of the most striking consequences of this transition is the emergence of anomalous density fluctuations in the ordered phase. In equilibrium fluids, density fluctua-

tions are well understood and are typically quantified using the density field which is defined in terms of delta functions by

$$\rho(\mathbf{r}, t) = \sum_{i=1}^N \delta[\mathbf{r} - \mathbf{r}_i(t)] . \quad (1.3)$$

To characterize spatial correlations in these fluctuations, one computes the static structure factor,

$$S(\mathbf{q}) \propto \langle |\delta\tilde{\rho}(\mathbf{q})|^2 \rangle , \quad (1.4)$$

where the tilde denotes the Fourier transform with wave vector \mathbf{q} , and $\delta\rho(\mathbf{r}, t) = \rho(\mathbf{r}, t) - \rho_0$ represents density fluctuations relative to the global average density ρ_0 . Note that the delta function has the inverse units of its arguments, and so ρ has the familiar dimensions of ℓ^{-d} , where ℓ is length and d is the number of spatial dimensions. The static structure factor is a dimensionless quantity though, and the proportionality factors are omitted in Eq. 1.4. In equilibrium systems, the structure factor is directly related to the isothermal compressibility (κ),

$$\kappa = \frac{S(|\mathbf{q}| \rightarrow 0)}{\rho_0 k_B T} . \quad (1.5)$$

A system with a large $S(0)$ is easily compressible, whereas a small $S(0)$ indicates that density fluctuations are strongly suppressed [93]. In ideal gases, where particles move independently, one finds $S(0) = 1$. In equilibrium fluids, the pair correlation function,

$$g(\mathbf{r}) = \langle \rho(\mathbf{r}')\rho(\mathbf{r} + \mathbf{r}') \rangle / \rho_0^2 \quad (1.6)$$

decays exponentially, ensuring that the long-wavelength limit of the static structure factor,

$$S(|\mathbf{q}| \rightarrow 0) = 1 + \rho_0 \int d^d \mathbf{r} [g(\mathbf{r}) - 1] \quad (1.7)$$

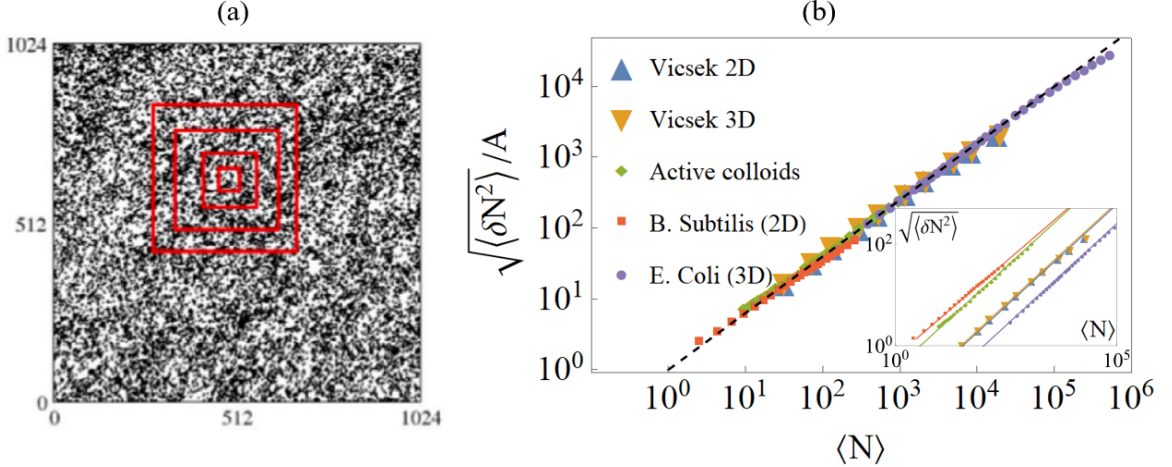


Figure 1.3: **Number fluctuation measurements in 2D and 3D flocking systems.** (a) An example of how number fluctuations, δN , are measured from a configuration of particles using (red) sub-volume bins that contain an increasingly large expected number of particles, $\langle N \rangle$ (figure taken from Ref. [43]). (b) Number fluctuation scaling data for Vicsek model simulations in 2D and 3D [21], active colloidal particles [57], wild type *Bacillus subtilis* colonies in 2D [138], *Escherichia coli* colonies in 3D [68]. Inset shows scaling data for each system with fits to Eq. 1.9, while the main panel shows a scaling collapse with normalization by the fitting parameter A . Dashed black line in the main panel denotes a fit to the power-law $\langle N \rangle^{0.8}$.

remains finite. A remarkable feature of flocking systems, however, is that the structure factor diverges in the long-wavelength limit as $S(\mathbf{q}) \propto |\mathbf{q}|^{-\gamma}$ with $\gamma > 0$, which, in an equilibrium setting, would be equivalent to an infinitely compressible system in the thermodynamic limit $L \rightarrow \infty$.

These anomalous density fluctuations, known as giant number fluctuations, can be quantified by relating the static structure factor to the variance of particle number fluctuations,

$$S(|\mathbf{q}| \rightarrow 0) \approx \frac{\langle \delta N^2 \rangle}{\langle N \rangle}, \quad (1.8)$$

where $\langle N \rangle$ is the expected number of particles in a sub-volume ℓ^d , and $\langle \delta N^2 \rangle$ is the variance in particle count. In equilibrium systems, number fluctuations scale as $\sqrt{\langle \delta N^2 \rangle} \propto \langle N \rangle^{0.5}$, whereas in flocking systems,

$$\sqrt{\langle \delta N^2 \rangle} \propto \langle N \rangle^\alpha \quad (1.9)$$

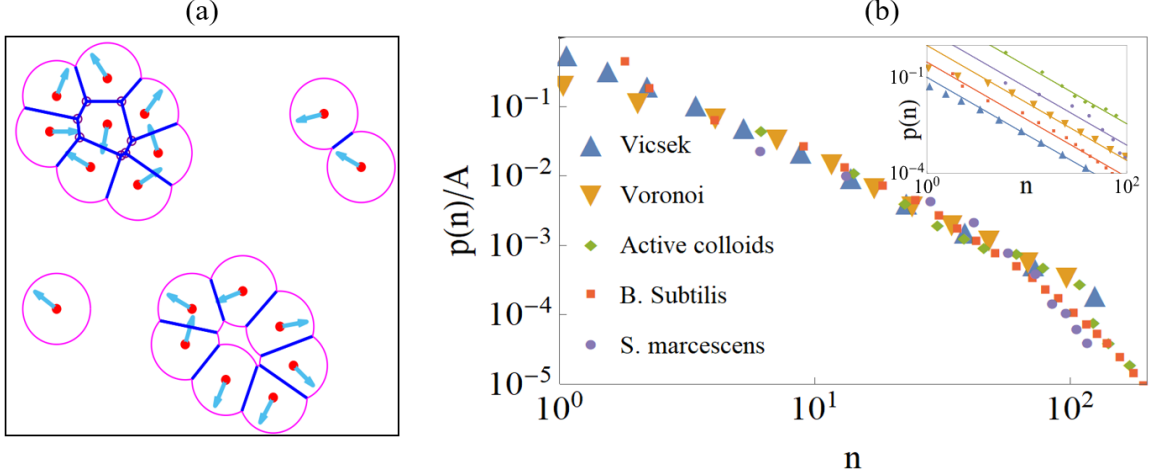


Figure 1.4: **Cluster size distributions in 2D flocking systems.** (a) Schematic example of four clusters of sizes 1, 2, 7, and 8 in the active Voronoi model (Figure taken from Ref. [54]). (b) The probability distribution of finding a cluster with n agents for the Vicsek model [21], active Voronoi model [54], active colloidal particles [59], wild type *Bacillus subtilis* colonies [138], colonies of *Serratia marcescens* [25] (all in 2D). Inset shows distribution data for each system with fits to the function $p(n) \propto A n^{-\zeta}$, and the main panel shows the scaling collapse.

where $\alpha > 0.5$. Giant number fluctuations have been observed in suspensions of active colloids² [57], protein filaments [100], bacterial colonies [138, 87, 68, 10], and confluent cell monolayers [39, 42, 137], all exhibiting similar scaling behavior (Fig. 1.3).

The emergence of giant number fluctuations in diverse active matter systems underscores the existence of universal statistical properties that transcend the microscopic details of individual agents. However, while structure factor scaling provides a rigorous mathematical signature of flocking universality, a more intuitive manifestation of this principle can be seen in the spatial organization of agents within a flock. In particular, the way individuals aggregate into clusters – self-organized groups of aligned agents – exhibits strikingly similar patterns across vastly different systems (Fig. 1.4). Whether in bacterial colonies, synthetic colloidal flocks, or simulated Vic-

²Active colloids are synthetic microscopic particles that exhibit self-propelled motion by exploiting physical or chemical asymmetries. Quincke rollers, for example, are dielectric with a charge imbalance between their Northern and Southern hemispheres; in the presence of an external electric field, these particles exhibit spontaneous rotational motion, leading to translational rolling motion along a surface (see Fig. 2.3f) [14].

sek models, collective motion often does not arise as a uniform state but rather as a dynamic network of coalescing and fragmenting clusters. This suggests that the same underlying physical mechanisms responsible for anomalous density fluctuations also govern the formation and distribution of flocking clusters, providing another robust indicator of universality in active matter systems.

1.3 Minimal Field Theory Models of Flocking

The Vicsek model provides a method for *numerically* studying flocking dynamics, capturing the essential features of collective motion in active matter systems. However, a complete theoretical understanding requires an *analytical* framework that describes the emergent macroscopic behavior from a coarse-grained perspective. The universality class that encompasses the Vicsek model, along with related models [140], is described by Toner-Tu theory [118]. Unlike agent-based models that track individual particles, this theory is formulated in terms of continuum fields, specifically the density field (Eq. 1.3) and the velocity field, defined by³

$$\mathbf{v}(\mathbf{r}, t) = \frac{1}{\rho(\mathbf{r}, t)} \sum_{i=1}^N v_0 \mathbf{n}_i(t) \delta[\mathbf{r} - \mathbf{r}_i(t)] . \quad (1.10)$$

The key insight by Toner and Tu was recognizing that the velocity field serves a dual role: it acts both as a hydrodynamic variable describing large-scale motion and as an order parameter that characterizes the onset of collective behavior. This is analogous to magnetization in the Ising model, which describes the transition from disorder to order in ferromagnetic systems. To make this analogy explicit, one defines an ‘order parameter field’,

$$\phi(\mathbf{r}, t) = \frac{|\mathbf{v}(\mathbf{r}, t)|}{v_0} , \quad (1.11)$$

³The definition of the velocity field in Eq. 1.10 is only valid in the thermodynamic limit, $N \rightarrow \infty$, at which point it becomes a smooth continuous function over space.

which quantifies the degree of local orientational order in the system. This allows the application of statistical field theory methods, particularly a Landau-Ginzburg free energy functional, to describe the emergence and stability of flocking states. This free energy functional provides a variational framework for studying non-equilibrium steady-states and their fluctuations by associating a cost to deviations of the order parameter from its steady-state value.

The core principle of Landau-Ginzburg theory is that, near a critical point, the large-scale behavior of a system is independent of microscopic details and instead governed by a small number of key properties: dimensionality and symmetries. For example, when the total number of agents in a flock is conserved, the density field evolution must obey the continuity equation:

$$\partial_t \rho + \nabla \cdot (\rho \mathbf{v}) = 0. \quad (1.12)$$

This principle also allows one to construct an effective free energy functional for the system (Eq.1.13) based solely on symmetry arguments. For instance, the Vicsek model's orientational dynamics (Eq.1.2) are rotationally invariant—meaning that globally rotating all agent orientations leaves the system unchanged. As a result, only terms respecting this symmetry appear in the free energy. One then obtains the Landau-Ginzburg free energy functional⁴.

$$F[\phi(\mathbf{r}, t), \nabla \phi(\mathbf{r}, t)] = \int_{\mathbb{R}^d} d^d \mathbf{r} \left[\frac{\alpha}{2} \phi^2 + \frac{\beta}{4} \phi^4 + \frac{D}{2} (\nabla \phi)^2 \right]. \quad (1.13)$$

Here In principle, higher-order terms such as ϕ^6 and $\nabla^4 \phi^2$ could be included, but they primarily affect mesoscopic behavior rather than large-scale macroscopic dynamics [47].

While Landau-Ginzburg theory effectively captures equilibrium phase transitions,

⁴Note that the symbol α is repeated in Eq. 1.13, but unrelated to the exponent in Eq. 1.9.

flocking is inherently an out-of-equilibrium phenomenon. The proper dynamical description is given by Toner-Tu hydrodynamics, which governs the evolution of the velocity field:

$$\partial_t \mathbf{v} + \lambda(\mathbf{v} \cdot \nabla) \mathbf{v} = -\frac{\delta F}{\delta \mathbf{v}} - \sigma \nabla \rho. \quad (1.14)$$

This equation is structurally similar to the Navier-Stokes equation of fluid dynamics⁵, with key modifications that account for the self-propelled nature of flocking particles. In a conventional fluid, the advection term has a prefactor of $\lambda = 1$, ensuring Galilean invariance (i.e., physics remains unchanged under a moving reference frame). However, in active matter systems, where particles maintain a fixed self-propulsion speed, Galilean invariance is broken, allowing λ to be an arbitrary parameter. This broken symmetry also allows for additional non-equilibrium advection terms – e.g., $(\nabla \cdot \mathbf{v})\mathbf{v}$ and $\nabla|\mathbf{v}|^2$ – to be present in Eq. 1.14, but we omit them and other permitted higher-order terms for the sake of conciseness here. The term $\sigma \nabla \rho$ represents an effective pressure that depends on density fluctuations, with σ denoting the compressibility of the system.

Together, Eqs. 1.13-1.12 define the Toner-Tu hydrodynamic equations, a widely studied framework that applies to a broad range of active matter systems, from bird flocks and bacterial swarms to synthetic colloidal rollers. While the specific values of the phenomenological parameters $\{\alpha, \beta, D, \lambda, \sigma\}$ depend on microscopic details – such as whether the agents are swimming bacteria or airborne starlings – the structure of the equations is expected to be universal and its flocking dynamics are governed by fundamental principles rather than system-specific interactions.

One of the greatest successes of Toner-Tu theory is its prediction of giant number fluctuations (Eq.1.9), a hallmark of flocking systems that has been observed in experiments across biological and synthetic active matter systems (Fig.1.3b). Beyond

⁵Note that upon taking the functional derivative in Eq. 1.14 that one obtains a viscous-like term $D\nabla^2 \mathbf{v}$.

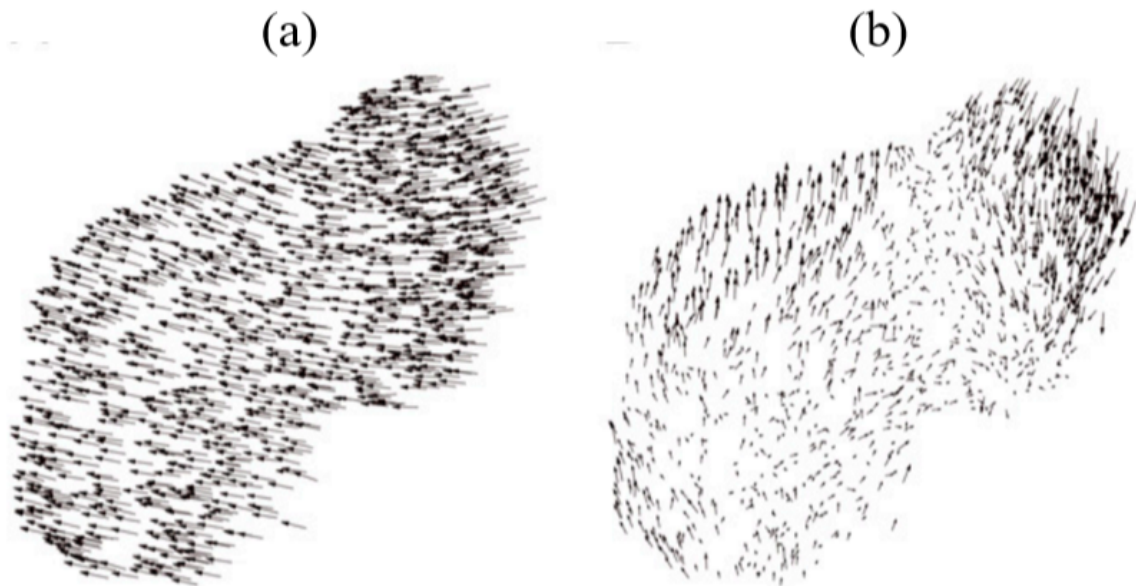


Figure 1.5: **Velocity fluctuations in a starling flock.** Instantaneous state of individual birds within a starling flock of 1246 birds occupying a space with linear size $L = 36.5 m$ (a) The velocity vectors are shown and indicate that the flock is strongly ordered. (b) The individual velocity fluctuations, away from the global orientation in (a), are shown. Two large domains of strongly correlated birds are clearly visible. (Figure taken from Ref. [19]).

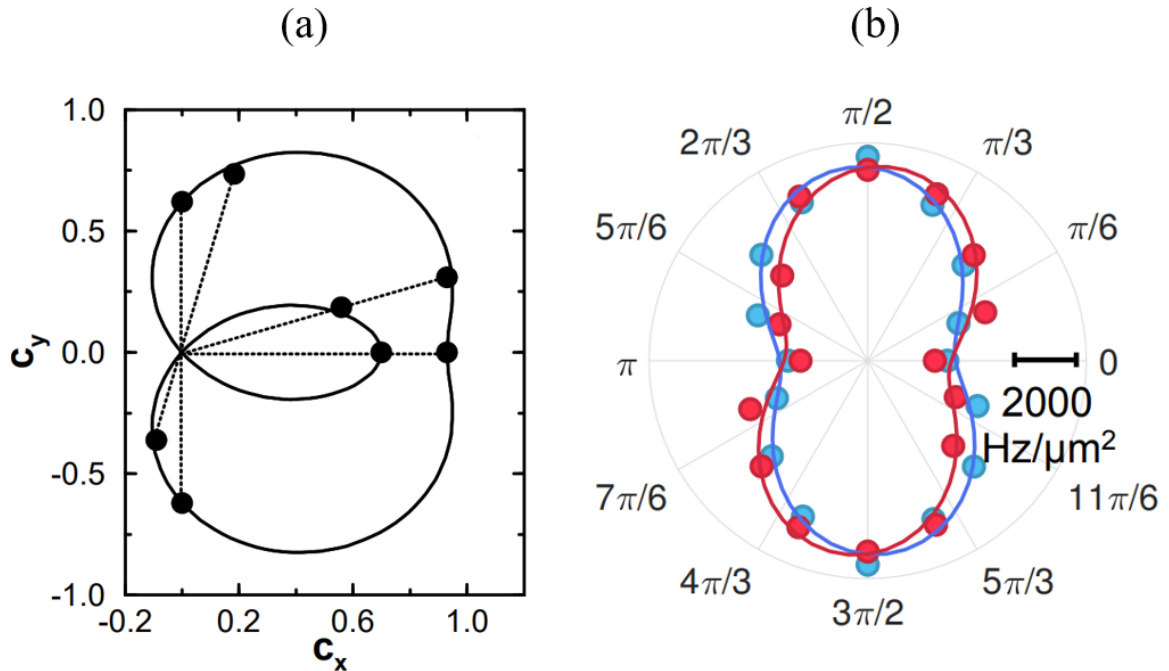


Figure 1.6: **Anisotropic sound speed in a flock.** Measured values of sound speeds (circles) at different orientations relative to the spontaneously selected flocking direction of a system are fit to the functional form of $c_{\pm}(\theta)$ predicted by Toner-Tu theory (solid lines).. (a) Sound speeds from a Vicsek model simulation are plotted in a Cartesian coordinate system (Figure taken from Ref. [122]) (b) Sound speeds from an active colloid experiment are plotted in a polar coordinate system (Figure taken from Ref. [41]). I note that the functional form being fit in both (a) and (b) is the same, and its shape simply changes depending on the effective values of the transport coefficients in the Toner-Tu descriptions of the flocks.

this prediction of the spatial structure of density fluctuations, Toner-Tu theory also describes how these density fluctuations should relax and propagate over time. Unlike in passive simple fluids where density fluctuations relax via Fickian diffusion, fluctuations in active fluids are advected and propagate throughout the system. In the ordered phase, where rotational symmetry is spontaneously broken and a flock has selected a collective motion direction, this propagation becomes anisotropic. That is, fluctuations in the velocity and density fields travel at different speeds depending on their orientation relative to the flocking direction. Transverse fluctuations – those perpendicular to the flock’s motion – correspond to Nambu-Goldstone modes, which are massless and long-lived. The fact that these modes are not damped and can propagate over arbitrarily long distances means that they remain correlated over large length scales (Fig. 1.5). In contrast, longitudinal fluctuations – those along the direction of motion – are quickly damped. Toner-Tu theory makes highly specific predictions about how exactly the speed of propagation changes as one looks at all orientations between the purely longitudinal and transverse directions [118]. These predictions have been proven correct in both Vicsek model simulations Fig.1.6a. as well as experiments on colloidal flocks Fig.1.6b.

As discussed in this section, further demonstrating the robustness of Toner-Tu theory in describing real-world flocking phenomena.

1.4 Coarse-Graining Agent-Based Models Into Field Theories

In Section 1.2 I discussed the key features of flocking systems that the Vicsek model seeks to incorporate. Then in Section 1.3 I reviewed how one can simply write down a field theoretic description of the Vicsek model based purely on its dimensionality and symmetries. There are more rigorous methods for directly coarse-graining

microscopic interactions into effective interactions between fields though. Rigorous Boltzmann-style calculations, for example, have provided great insight into how the phenomenological parameters in Eqs. 1.13-1.14 depend on microscopic parameters, such as self-propulsion speed [9]. The coarse-graining methods can be tedious, but useful in capturing subtle symmetry breaking that is present in some agent-based models and that is not accounted for in standard Toner-Tu hydrodynamics. In this section, I briefly walk through original work I've done on a lattice based approach to coarse-graining the Vicsek model, and an implicit non-reciprocity buried within it, into a modified Toner-Tu theory. This detour highlights the challenge of thinking about even the simplest models of flocking, and how we can overcome those challenges to build on our theoretical understanding of complex systems far from equilibrium.

In its original formulation, the Vicsek model (Eqs. 1.1-1.2) has particles interact by each particle adopting the average orientation of its neighbors. This interaction is written explicitly as:

$$\langle \mathbf{v}_j(t) \rangle_{j \in \mathcal{N}_i(t)} \equiv \frac{1}{|\mathcal{N}_i(t)|} \sum_{j \in \mathcal{N}_i(t)} \mathbf{v}_j(t), \quad (1.15)$$

where $|\mathcal{N}_i(t)|$ denotes the cardinality (size) of the set of neighbors $\mathcal{N}_i(t)$ of particle i at time t . Many variants of the Vicsek model with different alignment interactions have been proposed over the years, all of which yield the same transition to collective motion and differ only in their precise phase boundaries [140]. Among them the self-propelled XY model is popular for its connection to the traditional XY model of ferromagnetism and its amenability to analytical study [107, 75, 22, 106, 130]. Its

equations of motion are

$$\dot{\mathbf{r}}_i(t) = v_0 \mathbf{e}[\theta_i(t)] \quad (1.16)$$

$$\dot{\theta}_i(t) = \frac{-\partial_{\theta_i} H}{|\mathcal{N}_i(t)|} + \eta \zeta_i(t), \quad (1.17)$$

where H is the ferromagnetic Hamiltonian

$$H = \sum_{\langle ij \rangle} \cos(\theta_j - \theta_i). \quad (1.18)$$

The convention of having alignment interactions normalized by the number of interacting neighbors is present in this model, just as in Eq. 1.15, because dense aggregations of particles can otherwise lead to erroneous simulation behavior [26]. Overlooked in the literature though is the fact that this normalization introduces non-reciprocity into the interactions between particles.

In ordinary physical systems, particles respect Newton’s third law (action-reaction symmetry) and exert equal and opposite forces on one another, $\mathbf{f}_{ij} = -\mathbf{f}_{ji}$. In Eq. 1.17 though, the torques have the relation

$$f_{ij} + f_{ji} = -\partial_{\theta_i} H \left(\frac{1}{|\mathcal{N}_i|} - \frac{1}{|\mathcal{N}_j|} \right). \quad (1.19)$$

That is, there is a non-reciprocity associated with the interaction that is proportional to the inverse difference in how many neighbors each particle has. In the appendix, I show that the coarse-grained description of models with such non-reciprocity must include a “neighbor-number field”

$$\mathcal{N}_i(\mathbf{r}, t) = \sum_{i=1}^N |\mathcal{N}_i(t)| \delta[\mathbf{r} - \mathbf{r}_i(t)]. \quad (1.20)$$

The lowest order correction to Toner-Tu hydrodynamics (Eq. 1.14) that accounts for the effect of this additional field is given by

$$\partial_t \mathbf{v} + \lambda(\mathbf{v} \cdot \nabla) \mathbf{v} = -\frac{\delta \tilde{F}}{\delta \mathbf{v}} - \sigma \nabla \rho - g_2 \left(\nabla \frac{1}{\mathcal{N}} \cdot \nabla \right) \mathbf{v}, \quad (1.21)$$

where \tilde{f} is the modified free energy functional

$$\tilde{F}[\phi(\mathbf{r}, t), \nabla \phi(\mathbf{r}, t)] = \int_{\mathbb{R}^d} d^d \mathbf{r} \left[\frac{\alpha}{2} \phi^2 + \frac{\beta}{4} \phi^4 + \frac{D}{2} (\nabla \phi)^2 - g_1 \left(\nabla^2 \frac{1}{\mathcal{N}} \right) \phi^2 \right]. \quad (1.22)$$

Here $g_{1,2}$ are phenomenological coupling parameters. The g_2 term is particularly interesting because, unlike the g_1 term, it cannot be expressed as the gradient of a free energy. This is a consequence of the non-reciprocal, many-body microscopic dynamics (Eq. 1.19) which themselves cannot be derived from the gradient of a Hamiltonian.

Given the prominence of both the Vicsek model and Toner-Tu theory in the soft matter and non-equilibrium physics literature, one might wonder why no one has discovered the discrepancy between the standard flocking and neighbor-number modified flocking in previous numerical studies? As I shown in the appendix, this is because in the face of external noise-induced fluctuations, Eqs. 1.21-1.22 renormalize to the standard Toner-Tu hydrodynamics, but with modified transport coefficients that are functions of $g_{1,2}$:

$$\partial_t \mathbf{v} + \tilde{\lambda}(\mathbf{v} \cdot \nabla) \mathbf{v} = -\frac{\delta F}{\delta \mathbf{v}} - \tilde{\sigma} \nabla \rho, \quad (1.23)$$

$$F[\phi(\mathbf{r}, t), \nabla \phi(\mathbf{r}, t)] = \int_{\mathbb{R}^d} d^d \mathbf{r} \left[\frac{\tilde{\alpha}}{2} \phi^2 + \frac{\tilde{\beta}}{4} \phi^4 + \frac{\tilde{D}}{2} (\nabla \phi)^2 \right]. \quad (1.24)$$

Although large-scale flocking hydrodynamics are ultimately unperturbed by this particular case of neighbor-number non-reciprocity, similar asymmetries can indeed lead to entirely new collective behaviors [38]. This example emphasizes though the challenge in active matter physics of understanding how subtle, implicit features of micro-

scopic agent-based models can coarse-grain into anomalous effective field interactions.

1.5 High-Complexity, Deep-Learning Models of Flocking

In this introduction, I have reviewed the theoretical basis for highly simplistic microscopic and macroscopic flocking models, as well as the coarse-graining techniques that connect the two. I have also presented experimental evidence that these frameworks actually capture structural (Figs. 1.3 and 1.4) and dynamical (Fig. 1.6) features of real flocks. These models are still unphysical though and cannot predict the true trajectory of a large collection of biological agents.

It remains an open question what types of systems, if any at all, it is even possible to write down equations of motion that faithfully reproduce the motion of living agents. A branch of study utilizing deep-learning techniques has emerged in active matter physics though to answer this question. Significant progress has been made with approaches that write down the set of all hydrodynamic interactions that are permitted by symmetry and learn the fit these models to coarse-grained fields while encouraging sparse representations [110, 48]. Other machine learning methods exist though that discover representations for the functional form of particle interactions – rather than field interactions – without any presupposition of a model [29].

Most of these techniques have only been truly applied to synthetic data of active particles though. Some recent studies have attempted to tackle the full complexity of biological systems [120, 67], but the focus has been primarily on uncovering statistical correlations in heterogeneous cell behavior rather rather than true inference of the mechanical cell-cell forces exerted on one another.

1.6 Structure of Dissertation

Toner-Tu theory provides a powerful framework for describing the phenomenon of flocking and successfully captures aspects of large-scale behavior in many active matter systems. However, real biological and synthetic flocks often exhibit complexities beyond the scope of this minimal model and, as discussed in Section 1.4, it is not always obvious how these complexities affect the stability of flocking phases. While many systems conform to Toner-Tu predictions, others deviate in ways that suggest the existence of distinct universality classes. The challenge is not only to determine where the boundaries of the Toner-Tu universality class lie but also to understand what new macroscopic behaviors emerge when key assumptions – such as the rules creating interaction networks, instantaneity of interactions, or locality of interactions – are violated. Extending the classical flocking framework to account for these complexities requires addressing three fundamental questions: How do different interaction network structures affect macroscopic behavior? What are the consequences of time-delayed interactions for collective motion? And how does introducing long-range interactions mediated by an surrounding medium influence the stability of flocking states? Each of these questions remains an active area of research, and in this dissertation I explore how we can begin to make progress on each one.

One major unresolved issue involves the nature of how agents choose the set of neighbors they interact with. In classical physics, all particles interact with one another via long-ranged electromagnetic or gravitational forces that decrease with separation distance according to $|\mathbf{r}_i - \mathbf{r}_j|^{-2}$. When dealing with highly coarse-grained interactions in active matter physics though, the details of which particles interact with which, and how those interactions vary with separation distance, depend on the system in question. For example, in swarms of bacteria, alignment arises through the simple mechanism of steric collisions between the elongated bodies of bacterial [34], and thus models of bacteria have distance-dependent interactions with neighbors

within a single body length [51]. In contrast, birds might align with their k -nearest neighbors regardless of distance [19, 23], and sheep align with their Voronoi neighbors when migrating [46]. These differences raise the question of whether alignment based on metric interactions (where an intrinsic length scale determines interaction range) leads to fundamentally different macroscopic behavior than topological interactions (where alignment is based on neighbor count, independent of distance) [44]. Theoretical studies suggest that both classes should belong to the same universality class [28, 88], but numerical evidence remains inconclusive [44, 71]. In Chapter 2, this dissertation presents my publication in Ref. [81] new numerical evidence at previously inaccessible length and time scales to provide final conclusive evidence that both metric and topological flocks exhibit the same macroscopic phase behavior at the order-disorder phase transition.

A second fundamental challenge in active matter physics is the absence of instantaneous, reciprocal interactions in many real biological systems. Toner-Tu theory assumes that interactions are reciprocal—meaning if one agent exerts a force on another, the second simultaneously exerts an equal and opposite force in return. However, in real systems, this symmetry is frequently broken. Birds and sheep, for example, interact only with agents within their forward field of vision, introducing a fore-aft asymmetry [24]. In active colloidal suspensions, self-propelled particles interact non-reciprocally because they extract energy from the medium in order to generate momentum [98]. Recent studies suggest that such non-reciprocal interactions can lead to novel phases of matter that are fundamentally distinct from those described by equilibrium or near-equilibrium theories [38]. In Chapter 3, this dissertation investigates how breaking action-reaction symmetry through time-delayed interactions alters flocking behavior and whether it gives rise to entirely new collective phases.

A third challenge concerns the role of the surrounding medium in active matter

systems, an aspect overlooked in the original Toner-Tu framework, which was developed primarily for airborne bird flocks. In macroscopic systems with high Reynolds numbers⁶, hydrodynamic interactions are often negligible. However, at microscopic scales—where swimmers such as bacteria and sperm cells operate at low Reynolds numbers—the momentum imparted to the surrounding fluid introduces long-range hydrodynamic interactions that can destabilize conventional flocking states [2]. In such cases, Toner-Tu theory must be extended to incorporate fluid-mediated interactions and the conservation of momentum in the surrounding medium. Understanding how fluid coupling modifies flocking behavior is an open problem that this dissertation addresses through theoretical modeling and comparisons with experimental observations. In Chapter 4, this dissertation presents my publication in Ref. [82] examines flocking behavior in low Reynolds number environments and shows that, despite the strong coupling of the solvent to the swimming agents, there are parameter regimes where Toner-Tu theory is still predictive of the macroscopic behavior.

Finally, in Chapter 5 I present preliminary work which – rather than modeling biological systems with simplistic toy models – applies deep learning techniques to model collective cell migration. I explore how one might use a data-driven machine learning approach to both discover symbolic representations of cell-cell interactions, rather than assuming a functional form *a priori*.

⁶Reynolds number, the ratio of inertial to viscous forces, is a dimensionless quantity characterizing the flow pattern of a fluid.

Chapter 2

Banded Phases In Topological Flocks

In Chapter 1.3, I discussed how a phenomenological theory of flocking can be derived by focusing on the symmetries and conservation laws governing the system. However, when considering systems composed of complex biological agents, additional microscopic details can become significant. One such detail that has garnered considerable attention is the mechanism by which agents select their interacting neighbors.

The simplest interaction mechanism is the ‘metric’ alignment rule, where agents align with others within a fixed distance [21]. This approach is well-suited to systems like bacterial or microtubule suspensions, where steric collisions between elongated bodies create effective alignment interactions on a characteristic length scale defined by the size of the agent (Fig. 2.1a). In contrast, more complex systems may rely on ‘topological’ alignment rules, where agents interact with neighbors independent of their distance. For instance, starlings [18] and pigeons [23] have been observed to align with their seven nearest neighbors, adhering to a k -nearest neighbor rule. Similarly, in confluent monolayers of cells (Fig. 2.1b), interactions are determined by direct physical contacts, described by the Voronoi neighbor rule [12]¹.

¹A Voronoi tessellation is a partitioning of space into regions based on distance to a specified set

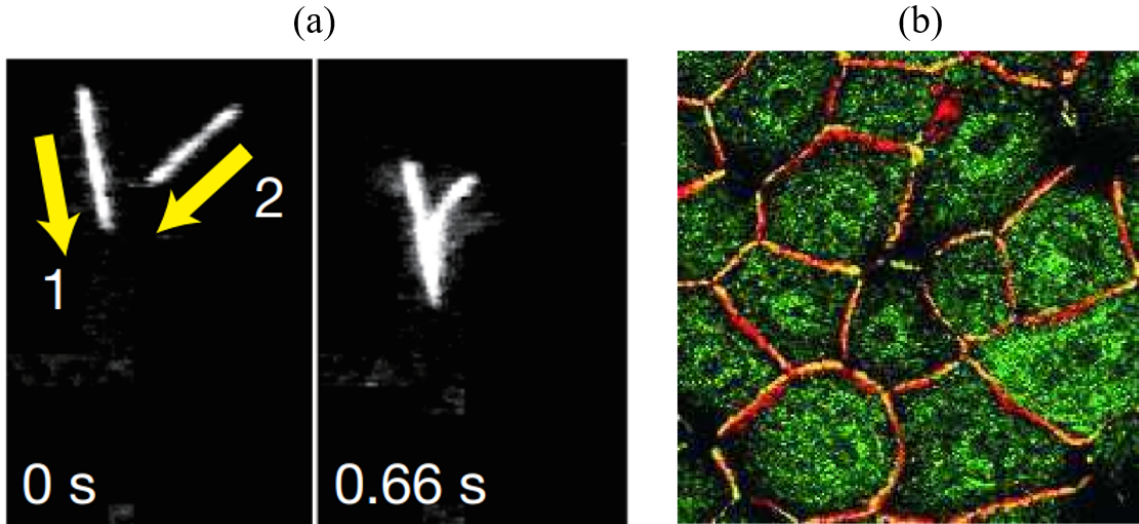


Figure 2.1: **Metric versus topological interactions.** (a) A time-lapse of two microtubules colliding and aligning their orientations (figure taken from Ref. [107]). An image of cells in an epithelial monolayer, where the cell nuclei are green and the cell-cell contacts are colored red and yellow (figure taken from Ref. [12]).

A long-standing debate in the field centers on whether these differences in microscopic alignment rules – metric versus topological – result in fundamentally different macroscopic flocking behaviors and distinct universality classes. Recent analytical work suggested that both metric and topological flocks might indeed belong to the same universality class with an order-disorder phase transition that is made discontinuous by the spontaneous formation of propagating, high-density, meso-scale ‘bands’ of particles [71]. Yet, numerical studies have provided conflicting evidence; while some Voronoi simulations indicate a continuous transition for topological flocks [44], other work on k -nearest neighbor models unambiguously report a discontinuous transition [71]. This discrepancy highlights the need for further investigation. Is it the case that different topologies for neighbor interactions, i.e. k -nearest neighbor versus Voronoi, actually do lead to different phase transitions? Or are disagreements in the literature the consequence of the phase transition being sensitive to factors such as system size and the precise method of numerical implementation? In this chapter I present my

of seed points, where each region contains all points closer to its seed than to any other.

work from Ref. [81] investigating this question.

2.1 Introduction

This chapter begins by examining the nature of the order-disorder phase transition in metric flocks, highlighting the mechanisms that drive collective motion and phase separation. I then introduce the hydrodynamic theory that governs wave propagation near the critical point, providing a theoretical framework for understanding phase separation in flocking systems. Finally, I present my PhD work, which resolves a key contradiction in the flocking literature: by performing large-scale simulations, I demonstrate that topological flocks exhibit the same universality class as metric flocks, confirming that their order-disorder transition is fundamentally discontinuous.

2.1.1 Order-Disorder Transition In Metric Flocks

In metric flocks, agents interact by aligning with all others within a fixed interaction radius (Fig. 2.2a). As a result, increasing the average particle density enhances the number of alignment interactions, promoting the emergence of collective order (Fig. 2.2b). Within the framework of Toner-Tu theory, this order-disorder transition can be understood by considering homogeneous steady-state solutions to Eq. 1.14, where spatial gradients vanish, reducing the dynamics to $\delta F/\delta \mathbf{v} = 0$. In this regime, the steady-state flock velocity magnitude is given by

$$\bar{v} = \sqrt{\frac{\alpha}{\beta}} \quad (2.1)$$

where α quantifies the strength of local alignment interactions relative to noise. When α is negative, the system is in a disordered state and the solution in Eq. 2.1 is not valid; instead, the only steady-states one obtains are $\bar{v} = 0$. A positive α ensures that alignment overcomes stochastic fluctuations, allowing the system to establish

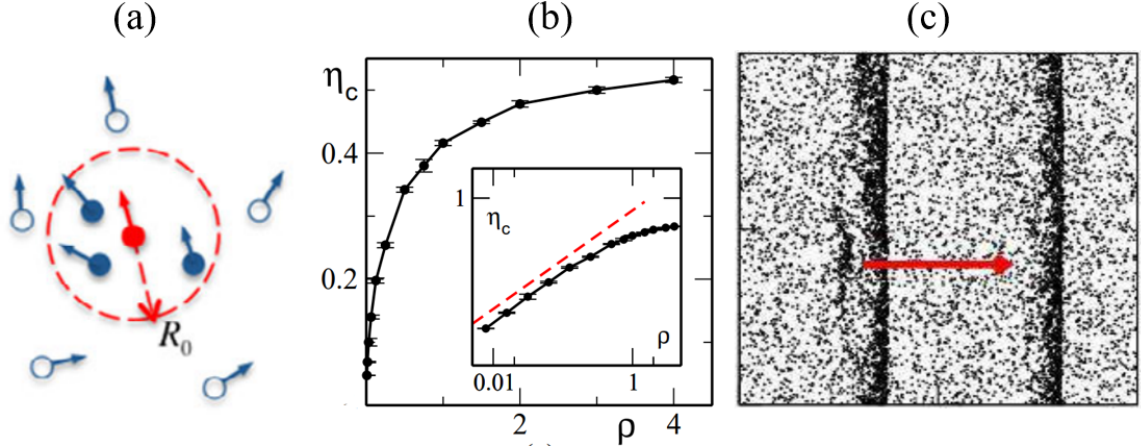


Figure 2.2: **Phase transition in the metric Vicsek model.** Numerical results are shown from simulations of the Vicsek model (Eqs. 1.1-1.2). (a) Schematic example of metric alignment interactions in the Vicsek model, where a (red) particle only aligns with neighbors within an interaction radius R_0 . (b) The critical noise strength (η_c) at which the order-disorder transition takes place is shown as a function of average global particle density; increasing density allows flocking phases to survive at larger noise strengths. (c) A snapshot of a large-scale simulation in the vicinity of the critical point η_c at a density of $\rho = 2$; spontaneously assembled meso-scale waves propagate through a background of disordered particles in the direction denoted by the red arrow. Figures taken from Refs. [21, 43].

global polar order. In metric flocks, local alignment strength is inherently tied to particle density, leading to a density-dependent form for α that can be approximated to leading order in ρ by

$$\alpha(\rho) = a_0(\rho - \rho_c), \quad (2.2)$$

where ρ_c represents the critical density required for ordering, and $a_0 > 0$ is a proportionality constant. Therefore, phase transition in metric flocks can be driven not only by tuning the strength of the noise acting on agents, but also by tuning the particle density (Fig. 2.2b). Despite the cartoonishly simple metric interaction rule for the Vicsek model shown in Fig. 2.2a, the predicted phenomenon of spontaneous self-organization into collective motion states at some critical density (Fig. 2.2b) has been observed in a diverse range of biological systems [113, 107, 82].

The Vicsek model predicts not only that metric flocks should have a density-

dependent phase transition between homogeneously disordered and ordered states, but that the transition should be discontinuous, with an intermediate inhomogeneous ‘banded phase’. As shown in Fig. 2.2c, one finds that near the critical point – at sufficiently large system sizes on the order of 10^5 particles – metric flocks do not uniformly flock in the same direction or remain globally disordered, but rather meso-scale ‘bands’ spontaneously form and begin propagating throughout the system. The formation, stability, and structure of these bands has been rigorously studied by the active matter physics community using agent-based models [131], Boltzmann-style coarse-graining methods [9, 73], and Toner-Tu hydrodynamics [104].

This unique flocking phase has even been robustly created in suspensions of active colloids [16]. As shown in Fig. 2.3, the transition between a disordered, isotropic ‘gas’ phase and a polar ‘liquid’ phase is separated by a well-defined banded phase qualitatively similar to Fig. 2.2c. The liquid/gas analogy is frequently used to describe phases of active matter because the banded phase is effectively a state of phase separation between ordered and disordered particles, similar to phase separation in the Van der Waals model of liquid-gas phase separation. In Fig. 2.3c, one can see that the moving front of a propagating wave is effectively an interface between a disordered region of particles and an ordered one. This analogy is made precise in the Toner-Tu description of banded phases [104].

2.1.2 Hydrodynamic Theory of Traveling Waves

By considering the nature of microscopic metric alignment interactions one arrives at the conclusion that local polar order should be proportional to local density (Eq. 2.2). How does this coupling affect the macroscopic field theory description of flocks though? Numerous studies have shown that, when $\alpha = \alpha(\rho)$, the homogeneous, ordered flocking state of Eq. 1.14 becomes linearly unstable to long-wavelength fluctuations near the critical point [73, 104, 71]. One can even precisely show that

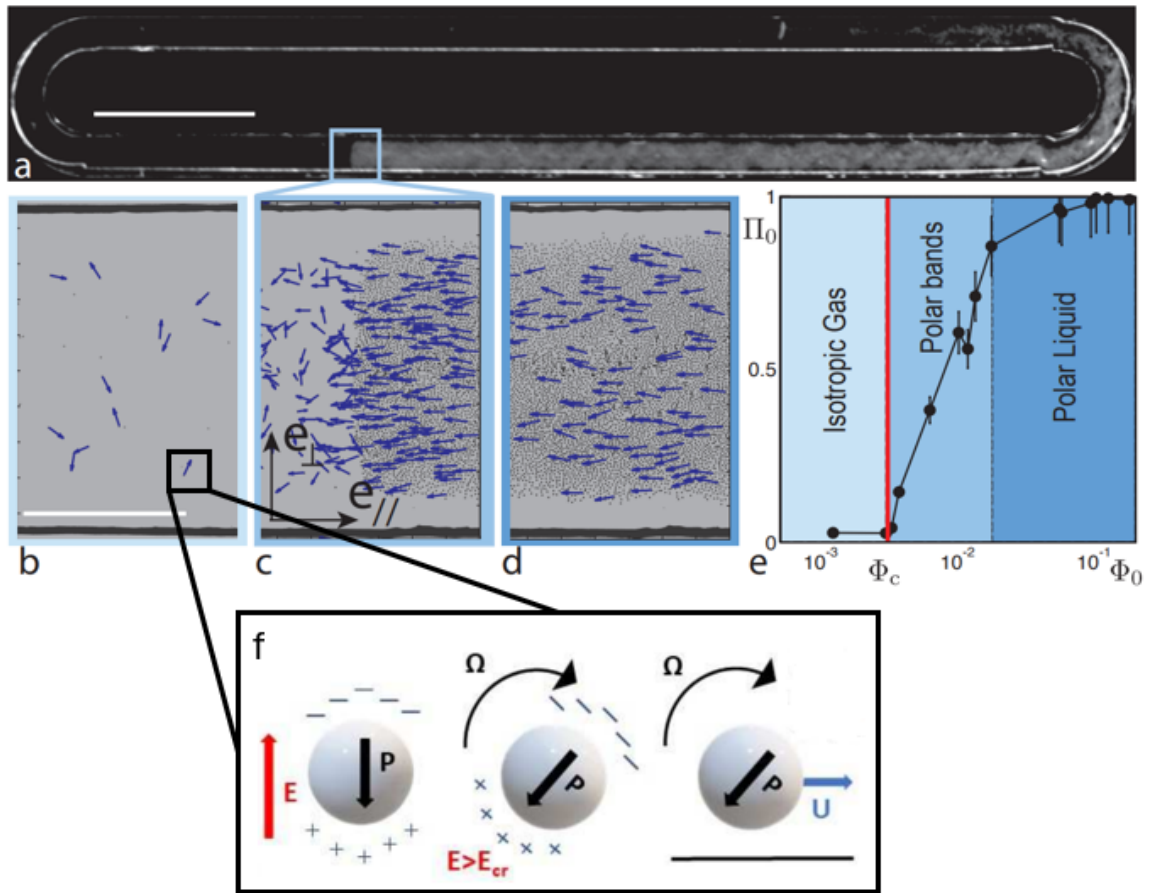


Figure 2.3: **Propagating waves in an active colloid suspension.** Experimental data for a system of self-propelled colloids. (a) Image of experimental setup, in which colloids have self-organized into a propagating wave around a circular track. (b) Particles in the space far away from the front of a propagating wave have a low density and are disordered. (c) The wave front is characterized by a phase separation between low-density/disordered and high-density/ordered states. (d) Within the propagating band, particles collectively flow together along the track. (e) The transition from homogeneously disordered to ordered states, with the intermediate phase coexistence regime, is shown as a function of colloid packing fraction (Φ_0). (f) A schematic representation of how active colloids become self-propelled via the Quincke instability in the presence of an external electric field (E); the torque generated by an unevenly distributed charge on the particle's surface overcomes the restoring torque of the electric field, leading to a translational speed U . Figures taken from Ref. [16, 14].

the instability conditions is [71]

$$\left| \frac{\partial \alpha}{\partial \rho} \right| > 0. \quad (2.3)$$

Qualitatively, one can understand Eq. 2.3 as implying that fluctuations in local density reinforce alignment, creating a feedback loop that amplifies density inhomogeneities. Toner-Tu theory thus agrees with simulations (Fig. 2.2) and experiments (Fig. 2.3) that the phase transition in metric flocks is discontinuous. Furthermore, the hydrodynamic framework can even predict the structure of the propagating bands observed near criticality.

The field theoretic understanding of band propagation begins by assuming the bands are spatially homogeneous along the transverse direction (r_{\perp}) and that the bands move at a characteristic velocity c in the direction of flocking (r_{\parallel}), permitting a transformation to the co-moving reference frame:

$$z = r_{\parallel} - ct. \quad (2.4)$$

Under these assumptions, the full two-dimensional system can be reduced to an effectively one-dimensional description:

$$\langle \rho(\mathbf{r}, t) \rangle_{r_{\perp}} = \rho(z), \quad (2.5)$$

$$\langle v_{\parallel}(\mathbf{r}, t) \rangle_{r_{\perp}} = v_{\parallel}(z), \quad (2.6)$$

$$\langle v_{\perp}(\mathbf{r}, t) \rangle_{r_{\perp}} = 0. \quad (2.7)$$

In this regime, the continuity equation for density (Eq. 1.12) simplifies to a linear relation between local density and the longitudinal velocity field:

$$\rho(z) = \rho_g + \frac{v_0}{c} v_{\parallel}(z). \quad (2.8)$$

This expression reveals that density variations are directly linked to the velocity fluctuations within the propagating band. Meanwhile, the equation of motion for the velocity field (Eq. 1.14) reduces to a Newtonian-like equation for $v_{\parallel}(z)$:

$$D\ddot{v}_{\parallel} = -f(v_{\parallel})\dot{v}_{\parallel} - \frac{dH}{dv_{\parallel}} \quad (2.9)$$

$$f(v_{\parallel}) = \left(c - \frac{\sigma v_0}{c} \right) - \lambda v_{\parallel} \quad (2.10)$$

$$H(v_{\parallel}) = -\frac{(\rho_c - \rho_g)}{2} v_{\parallel}^2 + \frac{v_0}{3c} v_{\parallel}^3 - \frac{\beta}{4} v_{\parallel}^4, \quad (2.11)$$

The function $H(v_{\parallel})$ plays the role of an effective potential governing the velocity profile, while the dissipative term $f(v_{\parallel})$ controls the stability of fluctuations. The solutions to these equations determine the steady-state structure of the propagating bands.

Solving Eqs. 2.9-2.11 yields two primary classes of solutions describing the propagating band structure. The first is a phase-separated profile:

$$v_{\parallel}^{\pm}(z) = A [1 + \tanh(k_{\pm}(z \pm z_0))] . \quad (2.12)$$

This solution corresponds to a band with a well-defined, symmetric density interface about its center, located at z_0 . The second solution describes an asymmetric soliton-like profile:

$$v_{\parallel}^{\pm}(z) \propto e^{k_{\pm}(z \pm z_0)} . \quad (2.13)$$

In large-scale simulations, such propagating bands are consistently observed at the order-disorder phase boundary, confirming these theoretical predictions [21, 73]. These results both qualitatively and quantitatively establish the nature of the order-disorder phase transition in metric flocks. In the following sections, I discuss our understanding of how the same instability mechanism and corresponding phase behavior manifests in topological flocks.

2.1.3 Topological Field Theory

The discussion so far has established that in metric flocks, local alignment strength depends on density, leading to a first-order phase transition marked by phase coexistence and propagating bands. This behavior arises because density fluctuations reinforce local alignment, creating a feedback loop that drives the instability. A natural question follows: does this same mechanism apply to topological flocks, where interactions are based not on metric distances but on a fixed number of nearest neighbors or a Voronoi-based interaction network?

At first glance, the answer appears to be no. Early numerical studies of topological flocking models directly measured the correlation between local density and local orientational order and found that while these quantities are positively correlated in metric flocks, they appear statistically independent in topological flocks (Fig. 2.4a). This suggests that the local alignment parameter α is effectively density-independent in topological flocks, i.e., $\partial\alpha/\partial\rho \approx 0$, implying that the instability mechanism responsible for phase coexistence in metric flocks should be absent. Consistent with this idea, agent-based simulations [44] and hydrodynamic calculations [88, 28] reported continuous phase transitions with no evidence of band formation or phase separation. However, recent theoretical developments challenge this long-standing view. A field-theoretic approach that accounts for the effects of renormalized hydrodynamics in the presence of stochastic fluctuations suggests that even if explicit density dependence is absent at the microscopic scale, long-wavelength fluctuations in density and polarization can dynamically couple, effectively introducing an emergent dependence of α on ρ [71]. This renormalized hydrodynamic framework predicts that topological flocks should, in fact, undergo a first-order transition, complete with phase coexistence and propagating bands—contradicting earlier numerical results [44].

There are two possibilities for the discrepancy within the literature: either the choice of topological interaction network (i.e. k -nearest neighbor vs. Voronoi tes-

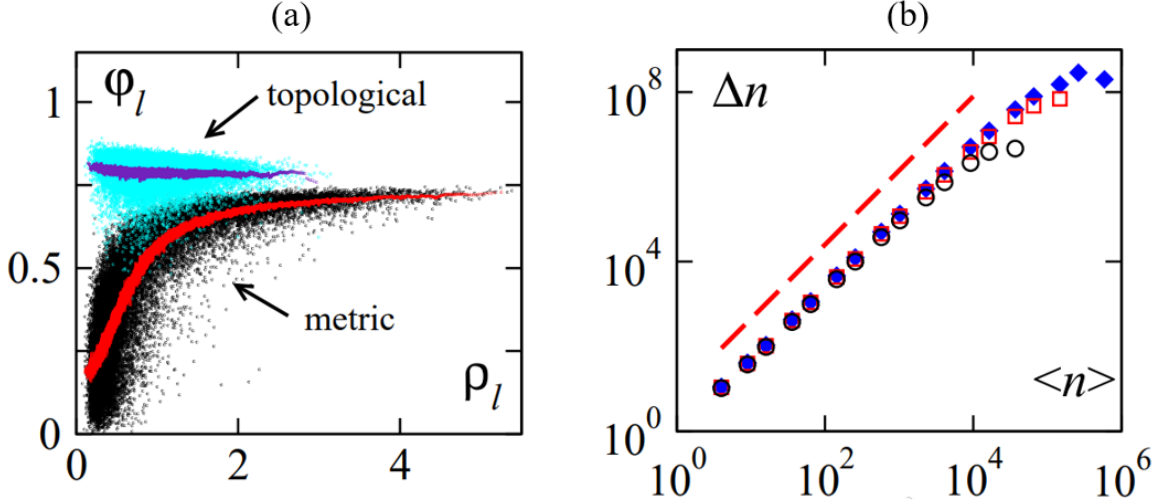


Figure 2.4: **Density statistics of topological flocks.** (a) The distribution of different measurements of the polar order parameter field (Eq. 1.11) as a function of local density (Eq. 1.3) is shown for Vicsek model simulations with Voronoi (topological) and metric neighbors. (b) Giant number fluctuation scaling measurements at increasing system sizes, $L = 64, 128, 256$, with the dashed red line denoting a fit to the power law $\propto \langle n \rangle^{0.88}$. Figures taken from Ref. [44].

sellation) leads to different phase transitions, or numerical errors such as finite-size effects are at play in one of the models [44, 71]. To address this issue, we performed large-scale simulations using a GPU-accelerated simulation package [111], enabling us to reach system sizes and timescales far beyond those of previous studies. This approach allows us to systematically test whether Voronoi flocks exhibit phase coexistence just as metric and k -nearest neighbor have been found to, or whether it belongs to a distinct class of flocking models.

2.2 Results

In this section, I present original research on the order-disorder transition in topological (Voronoi) flocking systems. Our findings reveal that the macroscopic phase behavior is highly sensitive to two often-overlooked numerical details: the numerical integration time-step size and the spatial resolution used to compute coarse-

grained fields. By systematically extending simulations to the thermodynamic and time-continuous limits, we demonstrate that the order-disorder transition in topological flocks is fundamentally discontinuous, marked by the emergence of propagating density waves at the critical point. However, in the discrete-time limit, where conventional simulations typically operate, the transition appears continuous across all computationally feasible system sizes – potentially explaining prior conflicting results in the literature [44]. Moreover, our analysis confirms that the structure of the propagating bands precisely matches the predictions of Toner-Tu theory (Eqs. 2.12-2.13), exhibiting true phase separation between ordered and disordered regions. This agreement between numerical results and hydrodynamic theory reinforces the universality of flocking behavior [71].

2.2.1 Model

In our study, rather than working with the Vicsek model (Eqs. 1.1-1.2), which is intrinsically time-discrete, we employ a self-propelled XY-like model [26, 140] where the positions and orientations of particles evolve in time according to

$$\frac{d\mathbf{r}_i(t)}{dt} = v_0 \begin{bmatrix} \cos \theta_i(t) \\ \sin \theta_i(t) \end{bmatrix}, \quad (2.14)$$

$$\frac{d\theta_i(t)}{dt} = -\nabla_{\theta_i} H + \eta \zeta_i(t). \quad (2.15)$$

Here v_0 is the self-propulsion speed, and the energy of particle i is given by

$$H[\{\theta_i(t)\}] = -\alpha \sum_{j \in \mathcal{N}_i(t)} \cos[\theta_i(t) - \theta_j(t)]. \quad (2.16)$$

The parameter α sets the interaction strength of the polar alignment. In all results reported here, we simulate incredibly large systems of $N = 1280000$ particles at a

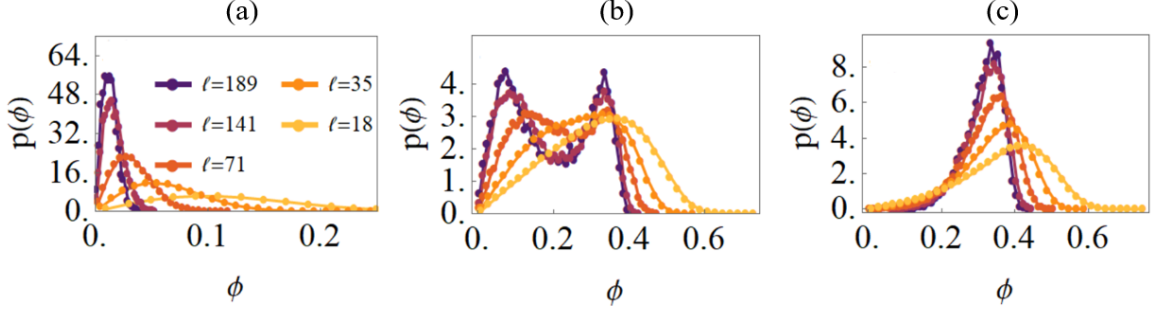


Figure 2.5: **Order parameter distributions across the transition.** The probability density function, $p(\phi)$ of the polar order parameter field (Eq. 1.11) when computed using square bins with varying linear size ℓ are shown in the (a) disordered phase, (b) critical point, and (c) ordered phase. Simulation parameters are $v_0 = 2.0$ and $dt = 5 \times 10^{-3}$.

density of $\rho_0 = 1.0$. The interaction strength is set to $\alpha = 1/6$, with 6 being the average number of Voronoi neighbors in a flat, periodic, two-dimensional system.

2.2.2 Coarse-Grained Fields Statistics

Running simulations of Eqs. 2.14-2.16 in the time-continuous limit ($dt \rightarrow 0$), we compute the probability density function, $p(\phi)$, of the coarse-grained polar order parameter field (Eq. 1.11) across the phase transition. In a continuous phase transition scenario, we expect $p(\phi)$ to vary across the phase transition, with a maximum variance at the critical point, but always remain Gaussian since the field $\phi(\mathbf{r}, t)$ should be fluctuating about the mean value of the homogeneous steady-state. In a discontinuous transition, $p(\phi)$ should become bimodal at the critical point since $\phi(\mathbf{r}, t)$ is instead fluctuating about an inhomogeneous steady-state that is a coexistence of both a disordered and ordered phase. In Fig. 2.5 I show that which scenario one observes in the Voronoi model strongly depends on the length-scale that one is using to compute the coarse-grained field $\phi(\mathbf{r}, t)$. When local values of polar order are computed using sub-volume bins of length ℓ containing $\mathcal{O}(10^2)$ particles, the transition appears continuous. At larger length-scales though, averaging over $\mathcal{O}(10^4)$ particles, the transition is revealed to truly be discontinuous. The qualitative change in the coarse-grained

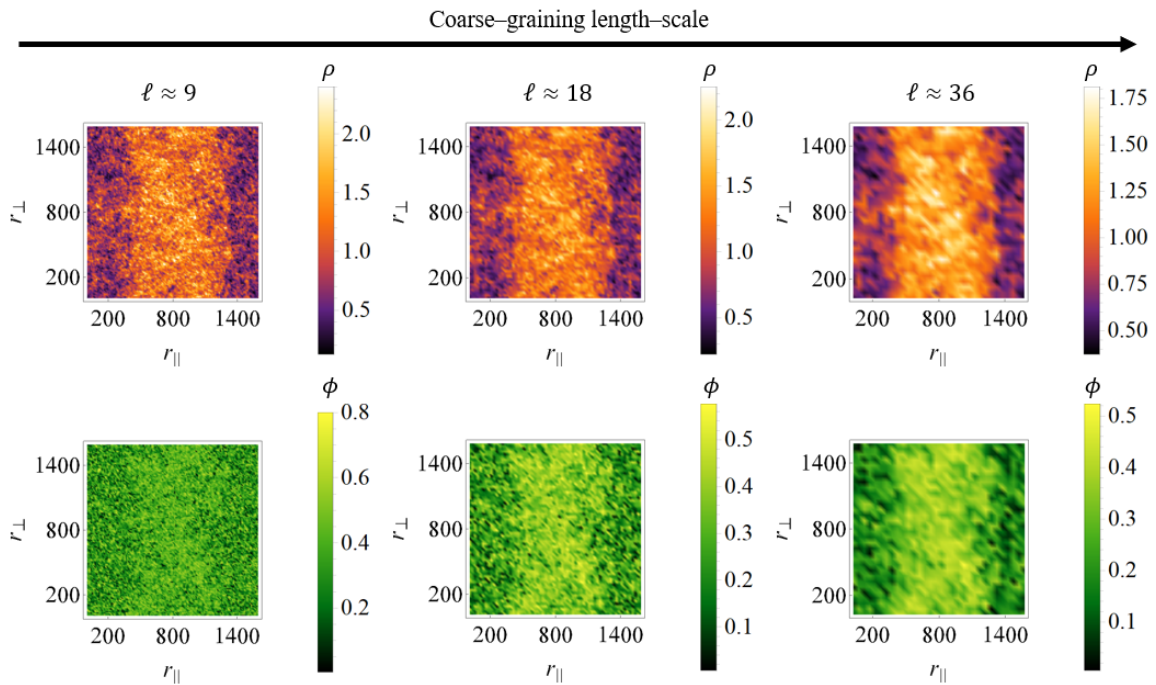


Figure 2.6: **Coarse-grained fields of a topological flock at criticality.** The density (ρ) and order parameter (ϕ) fields are computed from a single simulation snapshot in square bins of linear size ℓ . Simulation parameters are $v_0 = 2.0$ and $dt = 5 \times 10^{-3}$. These parameter values were chosen minimize the time for the simulation to converge to its steady-state.

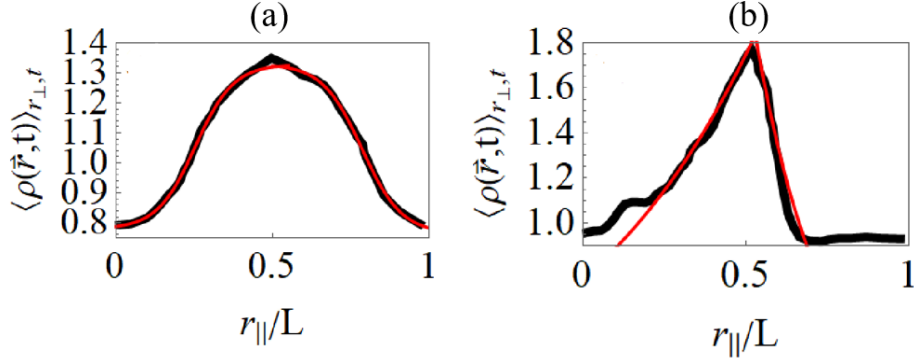


Figure 2.7: **Structure of bands in topological flocks.** The time-average density field profiles (Eq. 2.5) for a system with $v_0 = 2.0$ and $v_0 = 0.5$ are shown in (a) and (b) respectively with solid black lines. The solid red lines denote fits to the phase-separated (Eq. 2.12) and soliton-like (Eq. 2.13) profiles predicted by Toner-Tu theory.

fields as a function of the length-scale ℓ is shown in Fig. 2.6. These observations confirm that topological flocks do indeed exhibit the same critical behavior as metric flocks, and in the following section I show that even the internal structure of the propagating bands coincides with metric models.

2.2.3 Shape of Propagating Bands

As discussed in Chapter 2.1.2, Toner-Tu theory not only predicts the existence of a banded phase, but also gives precise details about how the fields should be structured within the propagating bands. In Fig. 2.7 I show that our simulations indeed conform to field theory expectations: at high self-propulsion speeds we observed phase-separated profile dynamics, while at low speeds the profile becomes asymmetric. How is it that we obtain such clean agreement with field theory whereas previous numerical studies – which even conducted finite-size scaling analyses [44] – observed continuous phase transitions?

The original formulation of the Vicsek model (Eq. 1.2) is inherently time-discrete, which established a convention in the literature of working in a large time-step ($dt = 1.0$) regime [44, 26, 71]. Our work has been conducted in the time-continuous regime ($dt \rightarrow 0$). To evaluate the stability of the banded phases we observe to time-step size,

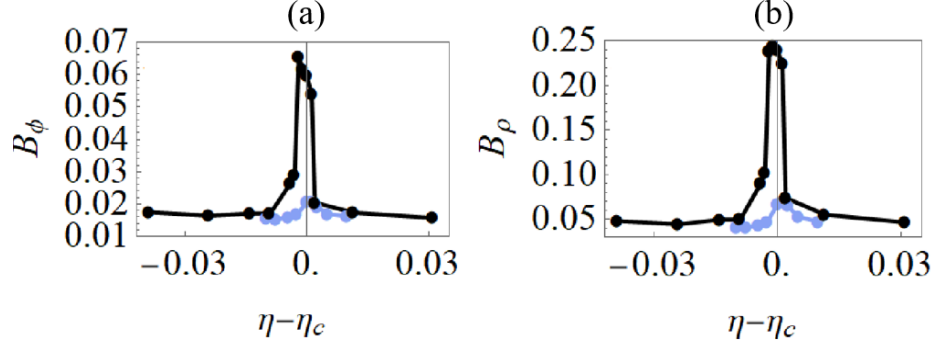


Figure 2.8: **Sensitivity of banded phases to time-step size.** The value of the banding order parameter (Eq. 2.17) is computed at various noise strengths across the phase transition for the density (ρ) and polar order parameter (ϕ) fields. Black data denotes simulations with $dt = 0.005$, and light blue data denotes simulations with $dt = 1.000$.

we look at the value of a ‘banding order parameter’ for a field profile $f(z)$,

$$B_f = \left\langle \left(f(z) - \langle f(z) \rangle_{r_{||}} \right)^2 \right\rangle_{r_{||}}, \quad (2.17)$$

which is simply the variance of the profile. In a homogeneous phase, either ordered or disordered, the profile is uniformly distributed over the length of the system and B_f vanishes. In a banded phase though, B_f becomes non-zero and indicates the presence of inhomogeneous structure. Computing this order parameter for both the density and polar order parameter field across the phase transition, we show that the banded phase only manifests in the continuous time limit, whereas in the discrete time limit the phase transition appears smooth (Fig. 2.8). This provides a resolution to the contradictory evidence in the literature about why earlier numerical studies on Voronoi flocks observed continuous phase transitions despite performing rigorous finite-size scaling analysis [44].

2.3 Conclusion

Our work conclusively demonstrates that Voronoi flocks exhibit the same discontinuous phase transition as both k -nearest neighbor and metric flocks. Moreover, we establish that the structure of the banded phase precisely conforms to the predictions of Toner-Tu theory, reinforcing the remarkable predictive power of hydrodynamic descriptions in active matter systems. Our results confirm the theoretical framework proposed in Ref. [71], which suggests that all flocking systems – whether metric or topological – exhibit an emergent coupling between density and orientational fluctuations, even when no explicit microscopic mechanism for such coupling is present.

A particularly intriguing observation in our simulations is that, unlike metric and k -nearest neighbor flocks, Voronoi flocks consistently form only a single propagating band. In contrast, metric models typically produce multiple bands that arrange themselves in a periodic fashion throughout the system (e.g., Fig. 2.2c) [21, 71]. We speculate that the absence of an intrinsic microscopic length scale in the Voronoi model results in the lack of a characteristic macroscopic length scale in the emergent banding pattern. However, a precise field-theoretic understanding of how length scale selection operates in these systems remains an open question.

A natural extension of this work would be to explore whether so-called ‘cross-sea’ phases arise in topological flocks. In large-scale simulations of the Vicsek model, an additional phase has been observed in which two perpendicular wavevectors define a complex banding structure [65]. Whether this phase is a universal feature of flocking models or an emergent property specific to metric interactions remains unknown. Further numerical and analytical studies of topological flocking models may provide crucial insight into the universality of this phenomenon.

The results presented in this chapter highlight the robustness of Toner-Tu universality in flocking systems, even when microscopic interaction rules differ significantly. However, while metric and topological flocks share the same macroscopic behavior,

real biological collectives often introduce additional broken symmetries that can fundamentally alter their universality class. In the following chapter, we turn our attention to such biological complexities, focusing on flocking systems with asymmetric and non-reciprocal interactions. Specifically, we investigate how time-delayed interactions introduce novel dynamical phenomena beyond the standard Toner-Tu framework.

Chapter 3

Flocks With Hierarchical Reaction Times

In the previous chapter, we demonstrated that despite fundamental differences in how interacting neighbors are selected, both metric and topological flocks belong to the same Toner-Tu universality class. This result aligns with the principle that coarse-grained flocking dynamics are governed by symmetries and conservation laws – specifically, rotational symmetry and mass conservation – both of which remain unchanged between these interaction rules (as discussed in Chapter 1.3). However, real biological systems introduce additional complexities, often breaking fundamental symmetries in ways that profoundly alter collective behavior, leading to entirely new universality classes.

One prominent example is the vision-based perception that drives topological interactions in bird flocks. While enabling alignment with nearest neighbors regardless of their distance, this sensory constraint also introduces fore-aft asymmetry and non-reciprocity in interactions [18, 23], as illustrated in Fig. 3.1. Unlike traditional flocking models, where interactions are assumed to be reciprocal, birds interact with others in their forward field of view but are often unaffected by those behind them. Non-

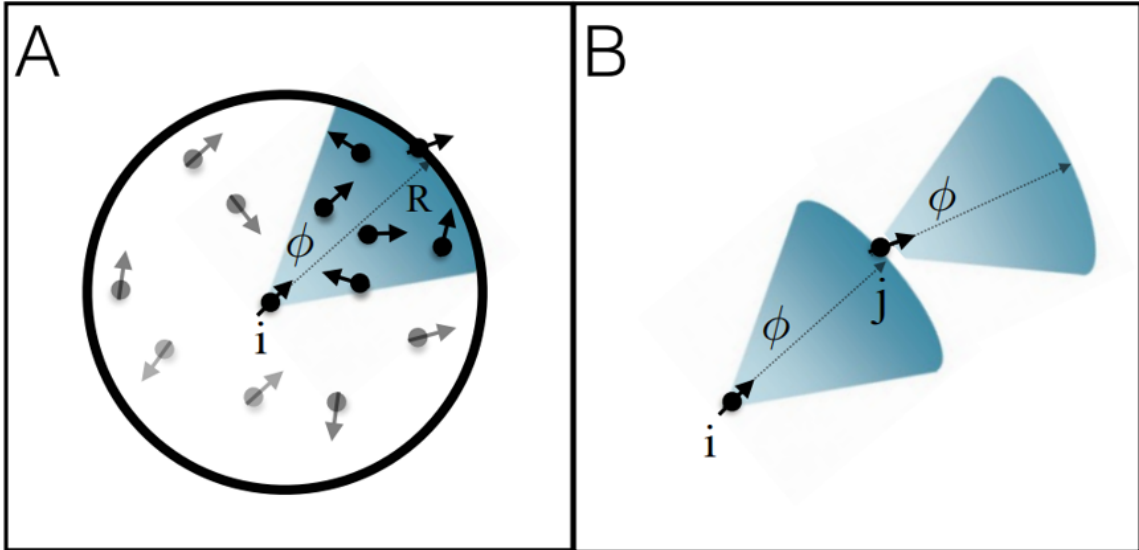


Figure 3.1: **Fore-aft non-reciprocity.** A schematic example of how a limited vision cone leads to fore-aft asymmetry between interacting agents within a flock. (a) An example of the possible neighbors for a single agent within a flock (b) Agent i interacts with j , but not vice-versa due to a limited vision cone. Figure taken from Ref. [35].

reciprocal flocking theories that incorporate this asymmetry predict a new universality class distinct from standard Toner-Tu dynamics [24, 31]. Notably, while Toner-Tu theory predicts that information propagates diffusively and is density-dependent, fore-aft asymmetric interactions lead to density-independent, ballistic information transmission, a crucial feature for smooth turns in real bird flocks [6].

Another fundamental asymmetry in biological flocking arises from reaction time differences among agents. Unlike idealized models where all agents respond instantaneously, real animals exhibit delays in perception and decision-making, which can vary among individuals due to differences in sensory processing and cognitive ability. This hierarchy¹ in reaction times leads to structured, leader-follower dynamics, which play a key role in collective decision-making [76, 45, 3, 46]. In these systems, leaders initiate movement decisions, and nearby agents respond with delays that re-

¹Within the biological literature [76, 46], a ‘hierarchy’ of reaction times is used synonymously with, what one calls in physics, a ‘distribution’ of reaction times. The fact that the distribution can be ordered, and that the ordering leads to effective “follower” and “leader” roles makes the term hierarchy linguistically useful.

flect their individual processing constraints. Consequently, the flock does not evolve synchronously, but instead follows a temporally staggered, hierarchical pattern.

The impact of heterogeneous reaction times on flocking behavior has been explored in recent studies [83], but significant gaps in our understanding remain. Most existing models assume a homogeneous time delay across all agents [35, 52, 40], which does not accurately capture the complexity of real social flocks. In this chapter, we introduce a new model of hierarchical time-delayed interactions and show that breaking interaction symmetry through heterogeneous time delays leads to a novel parity-time (PT) symmetry-breaking phase transition within the Toner-Tu flocking framework. Our results provide new insight into the role of temporal asymmetries in collective motion and extend the current understanding of flocking dynamics beyond the assumptions of instantaneous, reciprocal interactions.

3.1 Introduction

Before introducing our novel model for hierarchical flocking and its associated phase transitions, we first review empirical evidence of hierarchical structures in natural flocks. We then discuss the current theoretical understanding of time-delayed interactions in flocking systems, highlighting key findings and open questions. Before jumping into the following section, I first note that observations and measurements of reaction times on both humans and animals are abundant in the psychological and kinesiology literature [11, 64, 92]. These studies have rigorously established cognitive limits and variances in the reaction time of cognitive agents to sensory stimulus. The literature I review here in this chapter employs more speculative methods of inferring reaction times than other experiments performed in controlled settings, and should therefore be properly scrutinized. Their overall conclusions though, namely that there is a heterogeneous distribution of reaction times in natural flocks, is well established

by other studies [58].

3.1.1 Measurements of Time-Delayed Interactions in Flocks

A widely used method for inferring pair-wise interactions and quantifying time delays in biological systems is the velocity-velocity correlation function [76], defined as

$$C_{ij}(\tau) = \langle \mathbf{v}_i(t) \cdot \mathbf{v}_j(t + \tau) \rangle, \quad (3.1)$$

which measures how well the velocity of agent j at time $t + \tau$ aligns with the velocity of agent i at time t . The delay τ that maximizes $C_{ij}(\tau)$, denoted as τ_{\max} , provides an estimate of the reaction time of agent j in response to changes in agent i 's orientation. Figure 3.2 illustrates how this method can be used to reconstruct hierarchical interaction networks in flocks. This approach has revealed dynamic leader-follower structures in various animal groups. For example, in foraging bat pairs [45], herds of sheep [46], and packs of dogs [3], individuals interchangeably assume leader and follower roles over time. In contrast, homing pigeon flocks exhibit more stable hierarchies, with specific birds consistently maintaining leadership across multiple flights [76, 77]. These findings indicate that reaction time asymmetries are a fundamental feature of collective motion in social biological systems.

Despite its utility, the correlation function method has a critical limitation: correlation does not imply causation. That is, while strong correlations between individuals' velocities suggest leader-follower dynamics, they do not confirm whether changes in one bird's motion actively influence another's behavior. To address this, an alternative approach, the optimal causal entropy principle (oCEP), explicitly incorporates causality into the analysis of hierarchical networks [23]. The oCEP method quantifies causation by analyzing how much information one agent's past behavior provides

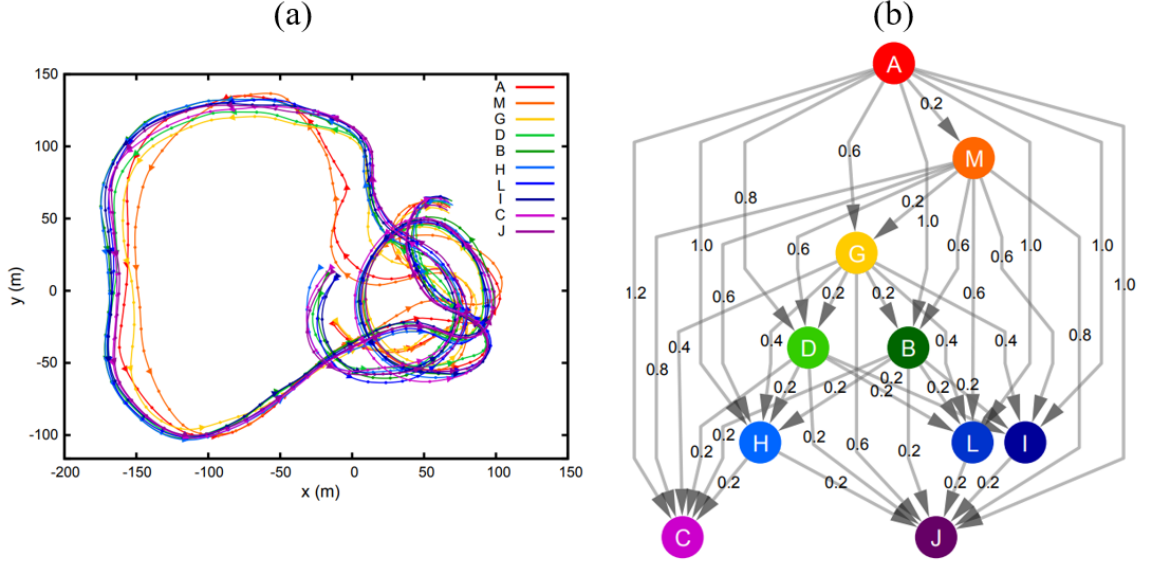


Figure 3.2: **Hierarchical time-delayed interactions in pigeons.** (a) The trajectory of a small flock of GPS-carrying pigeons is shown, with different bird trajectories denoted by different colors. (b) Using trajectory data from (a) to compute velocities in Eq. 3.1, the interaction network between the pigeons is shown, with the inferred reaction time (τ_{\max}) labeling each pair (i, j) . Figure taken from Ref. [76].

about another agent's future state. It does so by computing the causal entropy,

$$C_{Y \rightarrow Z|X} = H(X^{(t+\tau)}|Z^{(t)}) - H(X^{(t+\tau)}|Z^{(t)}, Y^{(t)}), \quad (3.2)$$

where $H(X|Y)$ is the conditional Shannon entropy,

$$H(X|Y) = - \sum_{x,y} p(x|y) \log p(x|y). \quad (3.3)$$

This formulation measures the reduction in uncertainty about an agent's future velocity ($X^{(t+\tau)}$) given knowledge of another agent's past state ($Y^{(t)}$), after controlling for shared external influences ($Z^{(t)}$). Applied to pigeon flocks, this method reproduces the hierarchical structure inferred using correlation functions but with an explicit causal interpretation [23].

These studies highlight that time delays in biological collectives are not merely an

artifact of measurement, but an inherent property of collective decision-making. Leaders influence followers through a cascade of delayed interactions, shaping the flock's collective motion in a hierarchical manner. Unlike the case of biologically-inspired topological models in the previous section, time-delayed interactions do fundamentally change the underlying symmetries of the system. Whereas the orientational dynamics in Eq. 2.15 with instantaneous interactions are time-reversible, time-delayed interactions mean that there truly is an asymmetry between the system evolving forward in time and backward in time. In the following section, the current understanding of how this additional symmetry breaking modifies standard Toner-Tu hydrodynamics is reviewed.

3.1.2 Time-Delay Models

Time-delayed interactions in flocking models introduce profound changes to the stability and dynamics of collective motion. One of the most striking effects of increasing delay is the transition in information propagation from diffusive to ballistic behavior. In systems with short delays, information about orientation spreads gradually, leading to diffusive adjustments in collective motion. However, as delays increase, information propagates in a ballistic manner, leading to wave-like, coherent maneuvers across the system [40, 52].

Beyond altering information transmission, time delays also impact the stability of flocking phases. Numerical studies on a three-dimensional Vicsek-like model have shown that increasing delay initially strengthens order before ultimately driving a transition from ordered to disordered motion [52]. A similar effect has been observed in two-dimensional flocking models, where reaction time heterogeneity leads to disordering transitions [83]. These findings highlight a non-monotonic effect of delay: short delays can reinforce order by filtering out fast fluctuations, but longer delays introduce competing alignment dynamics, ultimately leading to instability.

Furthermore, delays also introduce new dynamical phases in flocking models. In addition to standard coherent flocking and fully disordered motion, recent research has identified an intermediate patchy phase, where regions of ordered motion coexist with pockets of disorder [83]. This state emerges at intermediate delay values and is characterized by localized clusters of aligned agents moving within a background of randomized motion. Such hybrid phases suggest that delays can drive complex spatiotemporal structures not captured by traditional flocking models. Time-delayed interactions can also induce oscillatory and metastable states which arise due to the memory effects inherent in delayed interactions, leading to periodic bursts of order and disorder. This phenomenon has been experimentally validated in robotic swarm systems, where delays could be precisely controlled [114].

The above findings illustrate the diversity of behaviors that arise when time-reversal symmetry is broken in flocking models via delayed interactions. While models with a single, homogeneous time-delay can be systematically analyzed [52], real biological flocks exhibit heterogeneous delays. The challenge in incorporating delay heterogeneity lies in determining an appropriate distribution of delay times. The simple case of a Gaussian distribution has been studied [83], but tracking a distribution of delays requires maintaining long system histories, which becomes computationally prohibitive for large-scale simulations involving $N > 10^5$ agents [21]. As a result, most studies on time-delayed interactions have been constrained to small-scale systems with $N < 10^4$ agents [109, 35, 83]. To advance our understanding of how hierarchical and distributed time delays affect large-scale flocking dynamics, we introduce a novel model that both represents possibly the simplest choice for delay heterogeneity that one could write down and enables computationally efficient simulations.

3.2 Results

Here I present my original work on studying the effect of hierarchical time-delayed interactions on flocking phases. First, a novel time-delayed model is introduced. Next, I show how the model exhibits a spontaneous parity-time (PT) symmetry breaking not seen in conventional flocking models. Finally, I rigorously demonstrate that the new phase behavior is the result of a self-assembled spatial organization of particles based on their intrinsic time-delay.

3.2.1 Hierarchical Time Delay Model

Here we perform numerical simulations of Eqs. 2.14-2.16 with N agents in $L \times L$ periodic domains with a fixed density $\rho_0 = 1.0$, self-propulsion speed $v_0 = 0.5$, and a time-step size $dt = 1.0$, but with the following modification: over the discrete time-step, agents sequentially update their positions in time intervals $\tau = dt/N$. In the first interval, $[t, t + \tau]$, the particle with index $i = 1$ first updates its orientation with the Hamiltonian $H[\{\theta_1(t), \dots, \theta_N(t)\}]$ (given by Eq.2.16). In the next interval, $[t + \tau, t + 2\tau]$, the particle with index $i = 2$ updates its orientation in the same manner, but with the Hamiltonian now having the form $H[\{\theta_1(t - \tau), \theta_2(t), \dots, \theta_N(t)\}]$. Similarly, when particle $i = 3$ updates its orientation, the Hamiltonian is $H[\{\theta_1(t - 2\tau), \theta_2(t - \tau), \theta_3(t), \dots, \theta_N(t)\}]$. This pattern continues such that the Hamiltonian of the i^{th} agent is²

$$H_i = H \left[\{\theta_k(t - (i - k)\tau)\}_{k=1}^i \cup \{\theta_k(t)\}_{k=i}^N \right] \quad (3.4)$$

Consequently, the polar alignment force exerted on particle i by particle j ,

$$\mathbf{f}_{ij} = -\nabla H_i, \quad (3.5)$$

²The symbol \cup denotes the union of two sets.

will violate Newton's second law, $\mathbf{f}_{ij} \neq -\mathbf{f}_{ji}$ because $H_i \neq H_j$. Note that this non-reciprocity is unique to models with heterogeneous time-delays [83], while systems with homogeneous time-delays simply have Eq.2.16 replaced by $H = H[\{\theta_i(t - \tau)\}]$ [35]. In the rest of this chapter, I will discuss how the non-reciprocal forces produced by the time-delays in our model drives a novel parity-time (PT) symmetry-breaking phase transition.

3.2.2 Emergence of PT Symmetry Phase

In Chapter 2 I showed that the topological flocking model (Eq. 2.14-2.16) exhibits a disorder-to-order transition as the noise strength (η) is decreased past some critical value η_c . In the ordered phase, there is a global orientation ($\hat{\mathbf{r}}_{\parallel}$) that the system is moving in, and motion transverse to this global orientation ($\hat{\mathbf{r}}_{\perp}$) are regarded as undamped, long-lived fluctuations away from global order. In our simulations with the hierarchical Hamiltonian (Eq. 3.4), the same physics occurs and the model exhibits a standard Toner-Tu flocking phase (Fig. 3.3a,c). As we continue to decrease the noise strength though, a second phase transition emerges in which transverse fluctuations in the velocity field away from the global flocking direction become segregated into bulk bands (Fig. 3.3b,d). This inhomogeneity is reminiscent of the phase separation in the banded phase of the standard flocking model (Fig. 2.6). Whereas the transition from the disordered to banded phase in the standard flocking model is accompanied by a spontaneous rotational symmetry breaking – as the system develops a global direction of motion – the transition to the new phase in Fig. 3.3b,d is accompanied by the spontaneous emergence of a parity-time (PT) symmetry. That is, in a periodic system of size L and a global flocking speed of c , there is the following equivalency:

$$v_{\perp} \left(\mathbf{r}, t + \frac{L}{c} \right) = -v_{\perp} \left(\mathbf{r}, t + \frac{L}{2c} \right). \quad (3.6)$$

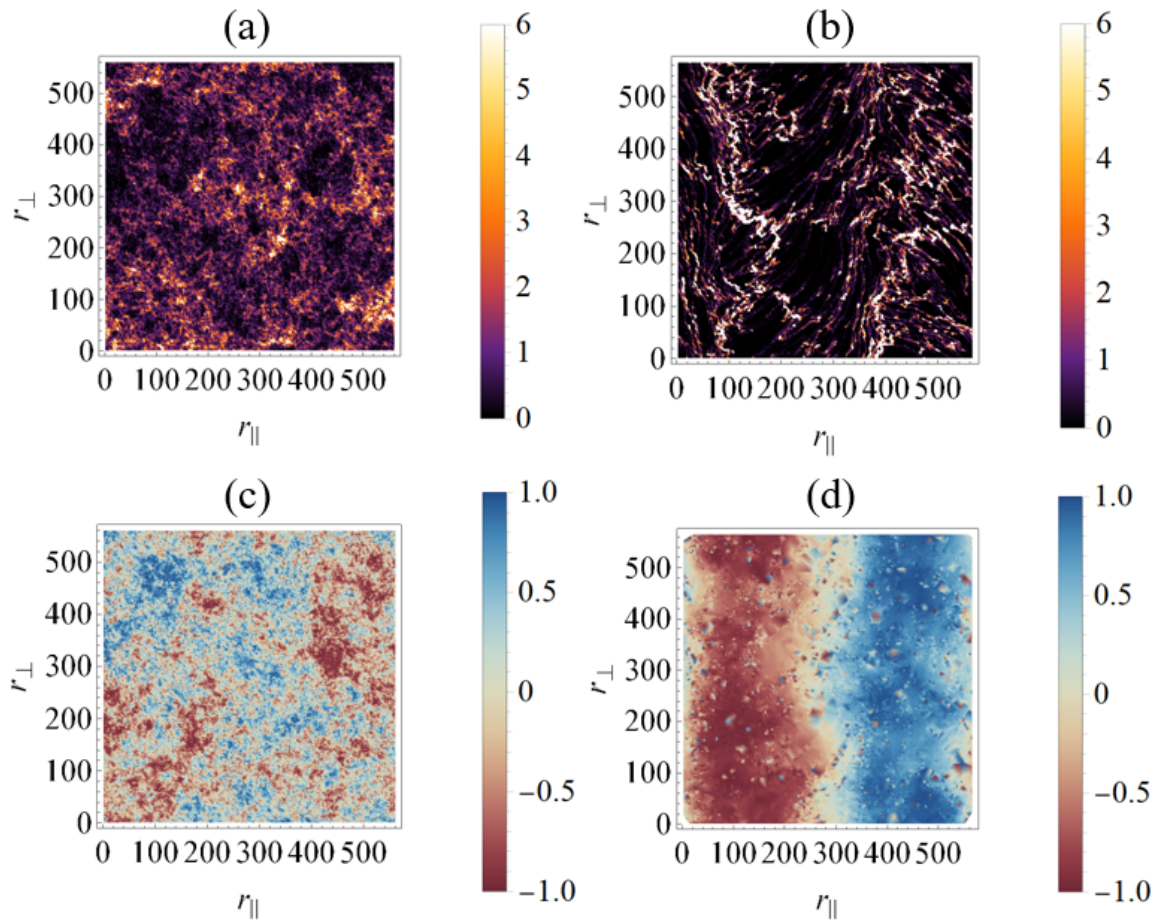


Figure 3.3: **Transition from flocking to PT-symmetric phase.** Simulation snapshots of the density (ρ) and transverse velocity (v_{\perp}) fields are shown on the top and bottom respectively. The transverse velocity field corresponds fluctuations in particle orientations away from the direction of global flocking (r_{\parallel}). Snapshots of the Toner-Tu flocking phase ($\eta = 0.10$) are shown in (a) and (c), and snapshots of the PT-symmetric phase ($\eta = 0.01$) are shown in (b) and (d).

This expresses the fact that propagating the pattern for a time L/c , i.e. one full ‘lap’ around the periodic domain, is equivalent to propagating for half of a lap followed by an inversion in the direction of transverse velocity fluctuations. In the flocking phase (Fig. 3.3c), transverse velocity fluctuations are disordered and decay (albeit at long time-scales relative to longitudinal fluctuations), so Eq. 3.6 does not hold and the symmetry is broken.

3.2.3 Phase Separation In the PT-Symmetric State

To quantitatively describe the flocking to PT-symmetric phase transition, we look at the statistics of the transverse velocity fluctuations. In Fig. 3.4a I show how particle orientations are distributed relative to the global flocking direction (i.e. $\theta_i = 0$ indicates a particle is perfectly aligned with the rest of the flock’s center-of-mass motion). In the standard flocking phase θ_i is normally distribution about zero. As lower noise strengths though, fluctuations away from the global direction of motion begin to (seemingly) paradoxically increase and a bimodality appears in the distribution. In analogy with the appearance of the banded phase in Fig. 2.5 – and its associated coexistence of disordered and ordered regions of space – the PT-symmetric phase we observe in this model can be regarded as a coexistence of counter-propagating ($+r_{\perp}$ and $-r_{\perp}$) bands. This novel state is shown to be robust to a finite-size scaling analysis in Fig. 3.4b. shows that this non-Gaussian behavior persists in the thermodynamic limit. In the following section, I show that this phase separation is a direct consequence of the presence of time-delayed interactions within our model.

3.2.4 Self-Assembled Spatial Organization of Agents

Here we study how the macroscopic dynamics of the PT-symmetric phase are related to the microscopic time-delays in our model. In Fig. 3.5a, we examine the system’s response to an “index shuffling” operation, where the indices of particles in the model’s

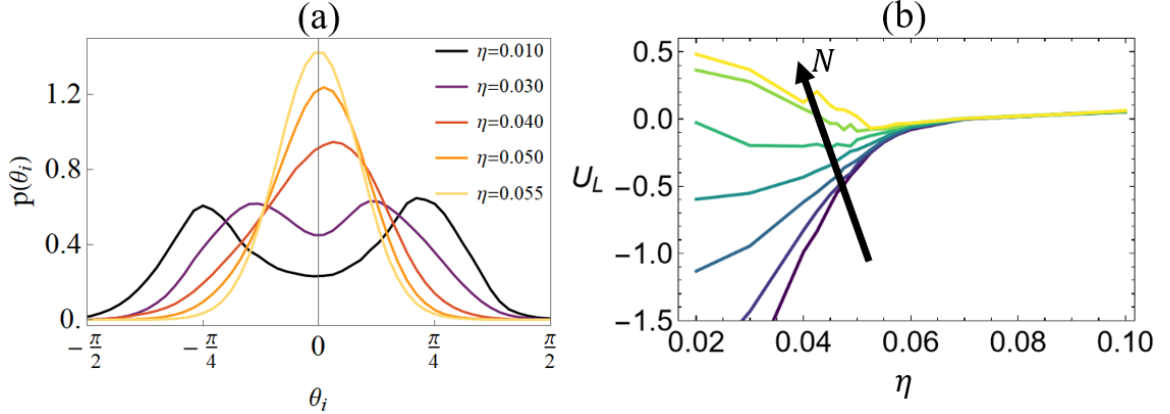


Figure 3.4: **Emergence of non-Gaussian statistics.** (a) Probability density function of single particle orientations relative to the global flocking direction. (b) Binder cumulant, $U_L = 1 - \langle \theta_i^4 \rangle / 3 \langle \theta_i^2 \rangle^2$, is shown for system sizes $N = \{2^{11}, 2^{12}, 2^{13}, 2^{14}, 2^{15}, 2^{16}, 2^{17}\}$. In the flocking phase θ_i is normally distributed and $U \approx 0$, and deviations away from $U = 0$ denote non-Gaussianity.

update sequence are randomly reassigned. This generates a new hierarchy within the sequential update process. In the homogeneous ordered phase, this operation has no impact on the stability of the flocking state. However, in the PT-symmetric phase, it disrupts global polarization. This result confirms that the introduction of time-delay in our model is directly linked to the emergence of the novel phase patterning. To further investigate this connection, we next analyze the precise mechanism by which time-delayed interactions give rise to the observed macroscopic dynamics.

As discussed in Section 3.2.1, incorporating a time-delay into the model also induces non-reciprocal interactions between agents. While a general analytical expression for these non-reciprocal forces cannot be explicitly derived, they can be computed numerically as:

$$f_{ij}^{\text{res}} = f_{ij} + f_{ji}. \quad (3.7)$$

When Newton's second law ($f_{ij} = -f_{ji}$) holds, f_{ij}^{res} vanishes. Otherwise, f_{ij}^{res} quantifies the residual non-reciprocal piece of the pair-wise interaction that arises from time-delays. One might expect though that these pair-wise non-reciprocal forces will be randomly oriented in space (because they arise from an abstract index ordering

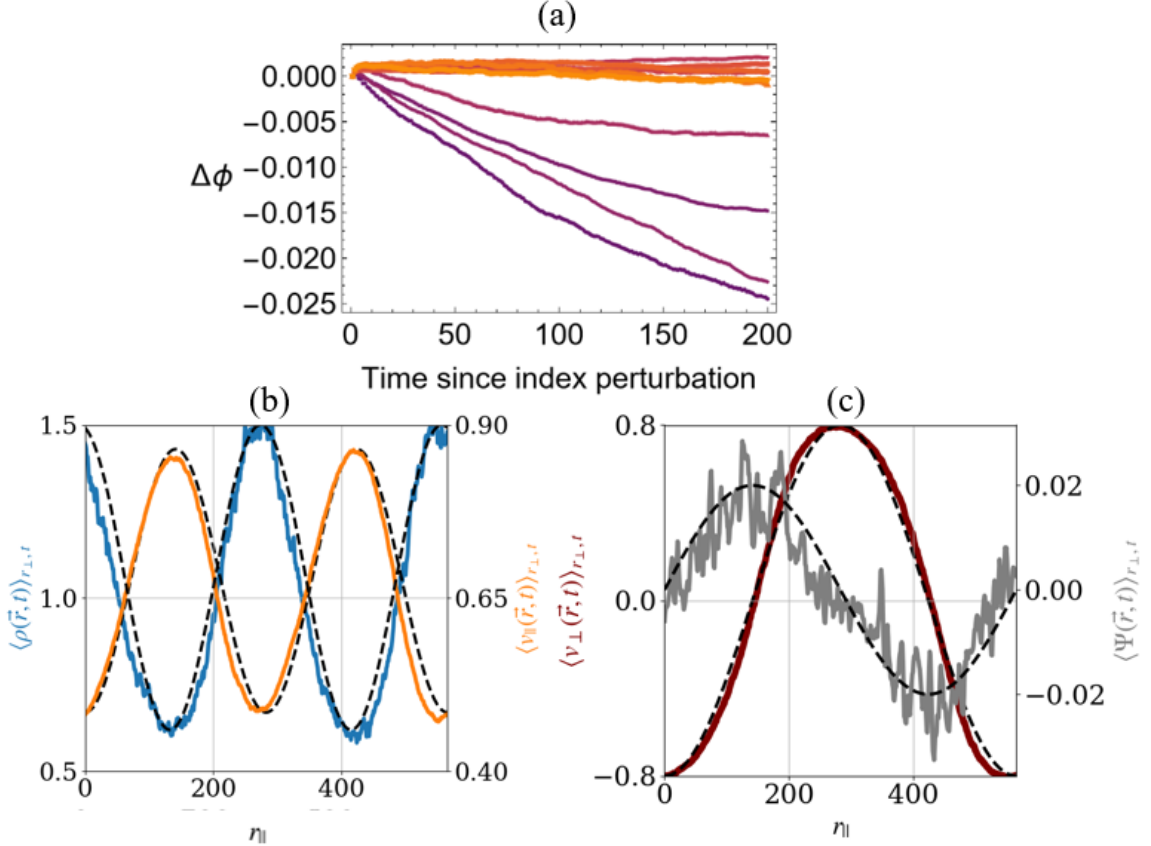


Figure 3.5: **Spontaneous ordering of time-delays.** (a) The response of our model to an instantaneous re-ordering of particle indices within our sequential update algorithm (described in Sec. 3.2.1) is shown at high noise strengths (red/orange) in the flocking phase, and low noise strengths (blue/purple) in the PT-symmetric phase. (b) Time-averaged profile of the transverse velocity field is denoted with the solid black line, and the profile of the non-reciprocal force field (Eq. 3.10) is denoted by the solid purple line. Dashed yellow lines indicate the positions of the interfaces between the counter-propagating bands of the PT-symmetric phase. Data was collected for a system of $N = 320000$ particles at a noise strength of $\eta = 0.005$.

that has no intrinsic spatial structure) and, on average, cancel each other out. To test whether these non-reciprocal forces actually generate new collective motion at macroscopic scales that would not be present in the synchronously updating system of Chapter 2, I calculate the difference between Eq. 2.16 and Eq. 3.4 and define

$$\Psi_i = -\nabla_{\theta_i} H_i - \nabla_{\theta_i} H. \quad (3.8)$$

This quantity denotes the total force on particle i after subtracting the motion that would arise in the reciprocal model.

To capture the macroscopic effects of these forces Ψ_i acting on all particles in our model, we apply the coarse-graining methodology from Section 1.3 and define an effective non-reciprocal force field as:

$$\Psi(\mathbf{r}, t) = \sum_{i=1}^N \Psi_i(t) \delta[\mathbf{r} - \mathbf{r}_i(t)], \quad (3.9)$$

Exploiting the symmetry of the PT-symmetric phase along the transverse direction (Fig. 3.3)—similar to the approach in Eqs. 2.5-2.7—we compute the average non-reciprocal force along the flocking direction ($r_{||}$):

$$\Psi(r_{||}, t) = \langle \Psi(\mathbf{r}, t) \rangle_{r_{\perp}}. \quad (3.10)$$

In the flocking phase we find that $\Psi(r_{||}, t) \approx 0$. This is unsurprising given that the microscopic pair-wise forces (Eq. 3.7) have no intrinsic spatial organization and emerge only from the random arrangement of particles with different time-delays. While we might expect that locally a particle might have a strong force ψ_{ij} acting on it, there is no reason to expect that the pair-wise forces would not simply cancel such that $\Psi(\mathbf{r}, t) \approx 0$ at large scales. However, in Fig. 3.5c, we illustrate how this effective force field coherently acts on PT-symmetric phases: in the bulk of each

counter-propagating band $\Psi(r_{\parallel}, t)$ vanishes, but at the two interfaces of the bands $\Psi(r_{\parallel}, t)$ exerts strong (relative to the noise strength) torques on the particles. At one interface, these torques are clockwise, while at the other they are counter-clockwise. The appearance of any non-zero steady-state non-reciprocal force field is shocking because it hints at a deeper underlying collective organization that arises from the hierarchical distribution of time-delays.

3.3 Conclusion

In this chapter, we explored how time-delayed interactions reshape collective motion by introducing non-reciprocal forces. Rather than acting as a minor perturbation, time delays fundamentally reorganize the system's macroscopic behavior, leading to the spontaneous formation of counter-propagating bands stabilized by a structured non-reciprocal force field. The emergence of a PT-symmetric phase in our system is, in retrospect, unsurprising. Recent field theoretic work by Fruchart et al. demonstrates that non-reciprocity is a hallmark of non-equilibrium systems, and whenever such interactions are present, we should expect PT-symmetric phases to emerge [38]. Non-reciprocal field theory also predicts the critical point in the transition to the PT-symmetry phase has the special property of being an exceptional point (the critical junctures where eigenmodes of two non-reciprocally coupled degrees of freedom coalesce). In our work, we focused on characterizing the mechanisms that give rise to the PT symmetric phase of our model, and a natural extension of our findings would be to investigate the critical behavior of the flocking to PT-symmetric transition in greater detail. Evidence of an exceptional point would be signaled by the coalescence of density and transverse velocity field fluctuations (i.e. the slow modes of the system that relax at much longer time-scales than longitudinal fluctuations); this measurement has been previously made in simulated and experimental flocks

[122, 41].

Beyond further numerical study of our model, the effectively one-dimensional structure of the PT-symmetric phase we observe makes it highly amenable to a field-theoretic study. This is a very special case, because time-delayed field theories typically take the form of integro-differential equations involving convolution operations with a memory kernel. Obtaining non-trivial analytic solution in such models is nearly impossible. Our work suggests that a more fruitful path towards a field theoretic understanding of time-delayed systems may be to replace convolution operations with a coarse-grained non-reciprocal force field. The model studied here presents an ideal case to test this hypothesis on. As discussed in Section 2.1.2, we already know how to study the dynamics inhomogeneous, patterned states in flocking models by imposing additional symmetry constraints on the Toner-Tu equations of motion [104]. In our model, we identify sinusoids as the inhomogeneous pattern selected by the PT-symmetry constraint. Eqs. 1.12-1.14.

Another natural question that this work raises is how does the nature of the PT symmetric phase change when interactions are metric rather than topological?

Chapter 4

Flocking and Vortex Phases In *Bos Taurus* Sperm Cells

Up to now in this dissertation, flocking agents have been referred to as “self-propelled” without concern for the origin or mechanism of their propulsion. In reality, an agent’s motion comes from forces exerted on its surrounding medium. For instance, a bird flaps its wings against the air, while a bacterium drives itself forward by beating its flagella against the surrounding fluid. Implicit in Vicsek-like active matter models is the assumption that the force exerted by the agents on the surrounding medium dissipates rapidly (and thus does not generate long-ranged interactions). Consequently, momentum is not conserved in such models. Systems for which this approximation is valid are termed “dry” active matter, and the collective behaviors they exhibit are governed primarily by local alignment and noise [20]. However, at microscopic scales where agents swim in low-Reynolds-number conditions, the approximation breaks down as the flow fields created by the agents decay slowly ($\propto 1/r$) and mediate long-ranged interactions [135].

In such “wet” active matter systems, hydrodynamic theory tells us that polar or-

dered flocking states are inherently unstable, because long-ranged interactions create feedback loops where small perturbations grow while being convected throughout the system [1]. Instead, low-Reynolds-number swimmers frequently self-organize into turbulent-like states characterized by spontaneously forming vortices that interact with one other and can form complex mesoscale patterning in suspensions of microswimmers [96, 107, 130]. However, experiments have found that we *Bos taurus* sperm cells can be induced into polar flocking states that – while ultimately unstable – are extremely long-lived. In this chapter, I discuss my work from Ref. [82] studying the structural properties of these transient flocking states and show that, surprisingly, many aspects of their behavior still conform to standard Toner-Tu theory despite the complex, external fluid mechanics involved in their interactions.

4.1 Introduction

I begin this chapter by reviewing the physics of local force flow fields created by agents moving in a low-Reynolds-number fluid. Then I focus on the specific case of swimming sperm cells and their complex hydrodynamic interactions. Then, I discuss the phenomena of emergent flocking and vortex states that emerge in suspensions of sperm cells under the application of a transient external pulse.

4.1.1 Hydrodynamics of Micro-swimmers

In wet active matter systems, self-propelled agents, often termed *micro-swimmers*, exhibit diverse motility strategies and are typically classified based on their hydrodynamic interactions with the surrounding fluid [36]. The two primary categories are *pushers* and *pullers*. Pushers, such as motile bacteria [5] and spermatozoa [82], generate thrust by expelling fluid backward with rear-mounted flagella, thereby creating an extensile force-dipole flow field. This propulsion mechanism leads to hydrody-

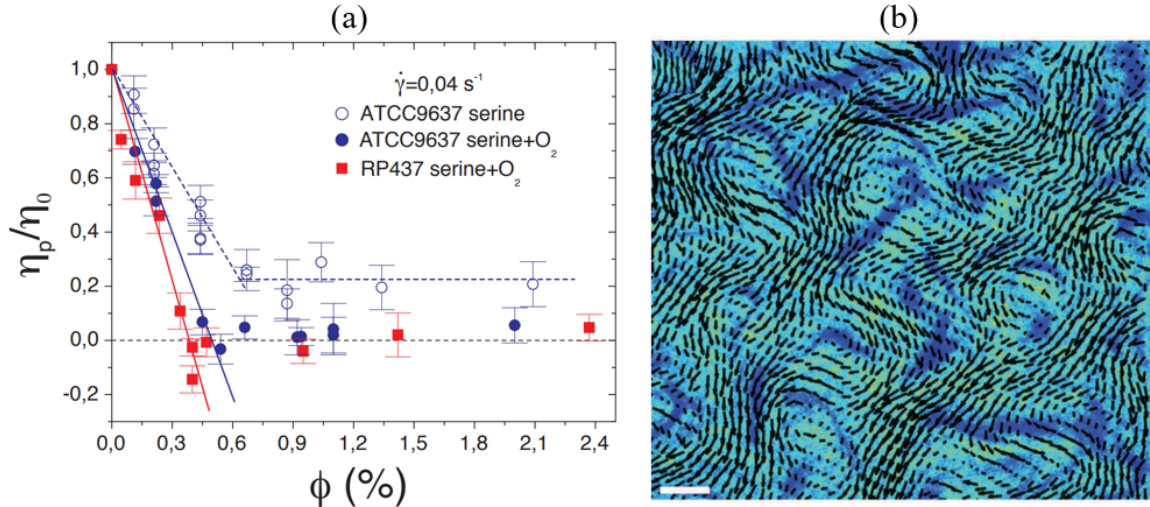


Figure 4.1: **Vortex-forming behavior of pusher micro-swimmers.** (a) The effective viscosity (η_p) relative to the solvent viscosity (η_0) for *Escherichia coli* at different packing fractions (ϕ) and fixed shear rate ($\dot{\gamma}$) [69]. (b) Velocity field of a suspension of ram sperm cells; note that the vortices are all rotating counter-clockwise (i.e. there is a preferred chirality). Scale bar is $200 \mu m$ [30].

dynamic instabilities that can induce collective motion and large-scale correlated flows, but not global polar ordered states [36]. Conversely, pullers, exemplified by the biflagellate algae *Chlamydomonas reinhardtii*, utilize front-mounted cilia to pull fluid inward, producing a contractile dipole flow that tends to stabilize their trajectories and suppress large-scale collective effects [132].

Pushers have garnered significant attention because their characteristic extensile stress generation can effectively reduce the viscosity of the suspending fluid [49]. Unlike passive suspensions, where viscosity typically increases with concentration, active suspensions of pushers such as motile bacteria *E. coli* and *B. subtilis* can exhibit a viscosity lower than that of the solvent, $\eta_p < \eta_0$ [69, 51]. This reduction in effective viscosity has been observed in bacterial swarms [72] and dense sperm cell suspensions [30]. In extreme cases, highly active micro-swimmer suspensions can transition into a regime resembling superfluidity, where the resistance to shear vanishes entirely (Fig. 4.1a). This unique hydrodynamic effect allows pushers to form self-sustaining vortices [51], which can further self-organize into intricate vortex

lattices [96, 130].

While pusher-type microswimmers can profoundly alter their fluid environment through viscosity reduction and vortex formation, the biological significance of these effects depends on the functional demands of the system. In bacterial suspensions for example, active turbulence leads to Lévy walks which are hypothesized to be advantageous for nutrient diffusion, resource acquisition, and several other biologically relevant objectives [74]. In contrast, sperm cells have a singular objective: navigating the complex and dynamic female reproductive tract to fertilize the egg. The efficiency of this transport is shaped not only by the motility of individual cells but also by emergent collective behaviors that arise from interactions with surfaces, neighboring sperm, and the viscoelastic fluids that fill the reproductive tract.

4.1.2 Collective Sperm Motility

As sperm traverse the female reproductive tract—a labyrinth of confined, mucus-laden, and actively flowing channels—their swimming behaviors are continuously modulated by environmental factors. The ability of sperm to navigate through these conditions depends on their capacity to adapt their swimming modes, exploit cooperative dynamics, and respond to external flows. In bulk fluids, sperm cells exhibit a three-dimensional (3D) helical swimming pattern [36]. In the presence of a solid boundary though, sperm tend to accumulate due to hydrodynamic and steric forces, leading to a distinct “slithering” swimming behavior characterized by increasing directional persistence [78]. Even the interactions between cells depends intricately on the external environment.

Unlike simple Newtonian fluids, the female reproductive tract contains viscoelastic mucus, which exhibits both dissipative and elastic properties [124]. This fluid gives rise to a hydrodynamic coupling between cells that produces sperm clusters, where individual cells align and swim cooperatively; these clusters enhance progres-

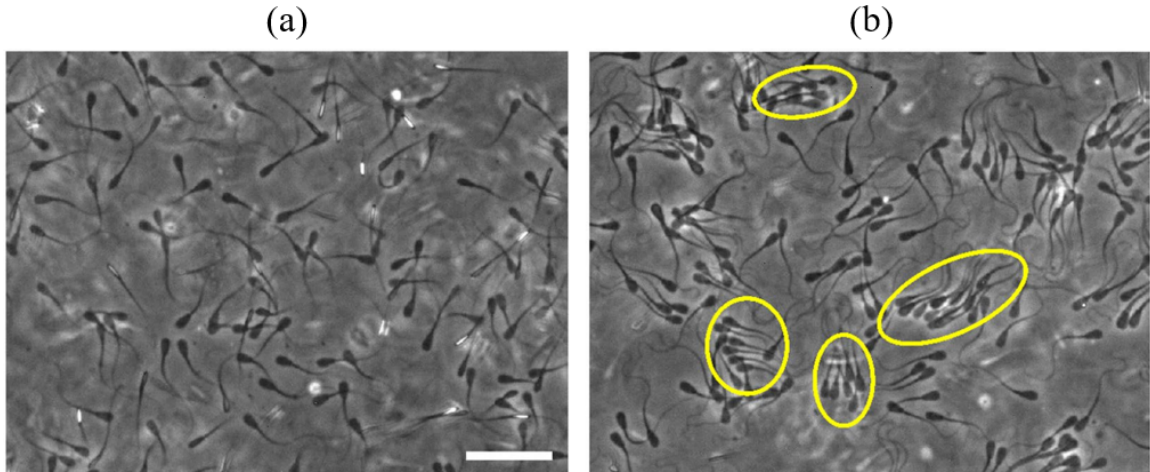


Figure 4.2: **Viscoelastic fluid induced clustering.** A representative image of sperm cells moving in (a) an ordinary, Newtonian fluid and (b) a viscoelastic fluid. Scale bar is $50\mu m$ (Figure taken from Ref. [124]).

sive motility, increasing both velocity and directional stability by reducing random re-orientations induced by shear forces [134, 90]. Experiments have also shown that clustering in viscoelastic fluids enhances the ability of sperm to swim upstream, known as rheotaxis, allowing them to exploit flow gradients to move against external forces [123, 136]. In the following section, I discuss how this polar alignment in the face of an external flow generates flocking-like states not seen in other suspensions of pusher-type microswimmers.

4.1.3 Pulse-Induced Vortex and Flocking States

Unlike other microscopic systems which can spontaneously self-organize into a flocking state at high densities, such as active colloids [41] and keratocytes [113], sperm cells do not exhibit flocking behavior on their own. Instead, dense suspensions of sperm exhibit turbulent dynamics like that shown in Fig. 4.1b. As mentioned in the previous section though, when subjected to an external flow field, they align *against* the flow and swim collectively in the same direction [123, 90]. Recent experiments have further shown that when the external flow is applied as a transient pulse, the sperm cells

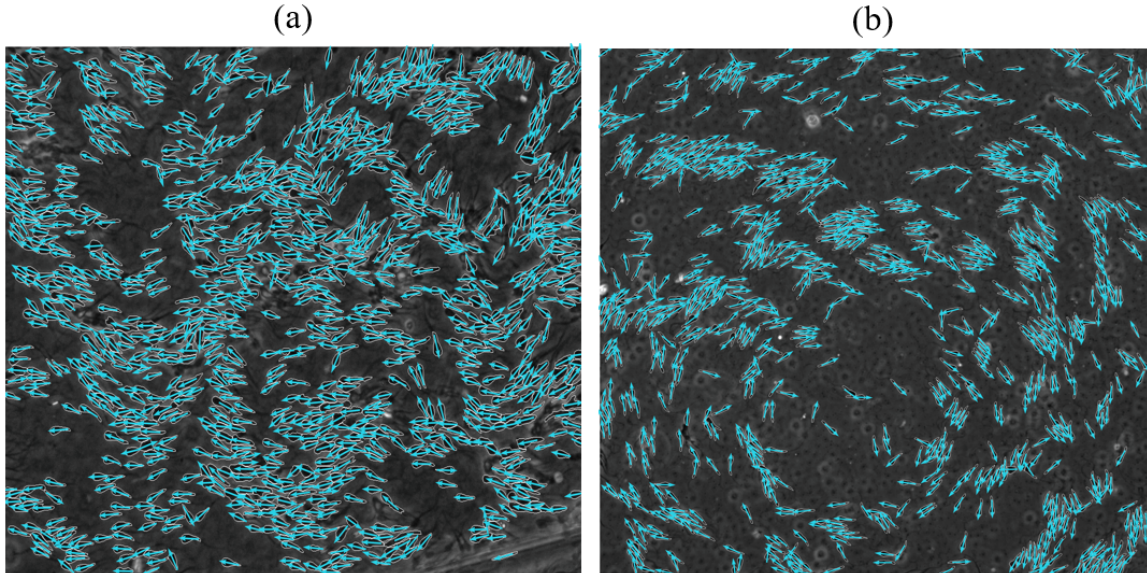


Figure 4.3: **Pulse-induced collective motion states.** Representative snapshots of the flocking (a) and vortex (b) states that arise when a transient hydrodynamic pulse is applied to a disordered suspension of sperm cells. White outlines denote cell segmentations, and blue arrows denote the tail-to-head orientation of each cell (Figure taken from Ref. [82]).

undergo a fascinating transition into either a macroscopic vortex state or a flocking state, as depicted in Fig. 4.3. Remarkably, this polarized state persists for nearly an hour after the flow is removed [82]. The pulse-induced flocking state is particularly intriguing from a theoretical standpoint, as it provides a rare opportunity to test the predictions of Toner-Tu theory in a regime where hydrodynamic interactions with the surrounding fluid play a dominant role. In the remainder of this chapter, I present original research conducted on pulse-induced collective motion in sperm cells and its implications for the validity of Toner-Tu theory in strongly fluid-coupled active matter systems.

4.2 Results

This section summarizes the results of the paper Ref. [82]. Collaborators Chih-Kuan Tung and Lisa Manning oversaw the experimental data collection that produced

microscopy videos of cell suspensions. I created a machine-learning image analysis pipeline for extracting quantitative information from microscopy videos and performed all simulations, and Daniel Sussman conceived of the project and facilitated the collaboration.

4.2.1 Inferring A Density-Dependent Transition Via Machine Learning

Our primary objective in this study was to investigate the dynamics of the pulse-induced flocking states observed in Fig. 4.3. However, before addressing the flocking behavior, we sought to understand why the cells occasionally transitioned into vortex states instead. Is there an externally tunable control parameter that determines which state the cells self-organize into? If so, want to study flocking states furthest away from the vortex-flocking transition point. Or, does the collective behavior depend on intrinsic cell properties that cannot be directly controlled?

To obtain quantitative insights into the two states, we trained a *cellpose* segmentation model to extract cell positions and orientations from individual frames of microscopy videos [105]. The segmentation model produces a high-precision mask of each individual cell, denoted by the white contour lines in Fig. 4.3. The cell orientations (\mathbf{n}_i) were determined based on the head-tail asymmetry in their segmented contours. From this data, we were able to construct coarse-grained density and velocity fields (Eq.1.10) from vast amounts of experimental video data, and categorize the collective motion states of each cell suspension by the polar order parameter and enstrophy of the velocity fields.

Enstrophy, which quantifies the magnitude of circulation in a fluid, was derived from the vorticity field $\omega(\mathbf{r}, t) = \nabla \times \mathbf{v}(\mathbf{r}, t)$. As shown in Fig. 4.4, the average global cell density emerged as a key control parameter in determining whether the cells formed a vortex or a flocking state. Specifically, vortex states predominated

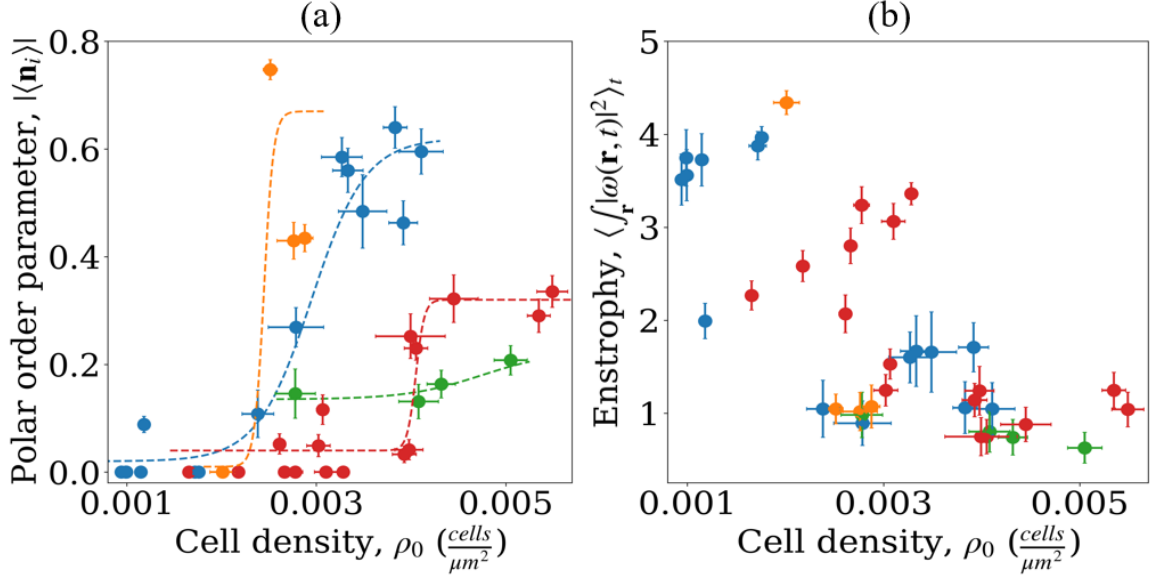


Figure 4.4: **Vortex to flocking transition.** The time-averaged polar order parameter and entropy are shown as a function of average global density for suspensions of sperm cells like those in Fig. 4.3. Each color here corresponds to a different experimental sample, and dashed lines in (a) denote fits to hyperbolic tangent functions.

at low densities, while flocking states emerged at higher densities. This behavior is reminiscent of the order-disorder transition in metric flocks (discussed in Chapter 2.1.1), though with a crucial distinction: at low densities, rather than remaining disordered, the cells self-organized into coherent vortex structures.

It is clear from Fig. 4.4 that density alone does not control the transition between vortex and polar states. Different samples at identical densities can exhibit a wide range of polar order values, which suggests that there is at least one other parameter intrinsic to the cells within samples that controls the transition. I return to this point later later in this section. For now, I note that this analysis informs us that flocking states in our experiments are most stable at high densities, and so we make comparisons with Toner-Tu theory in this regime.

4.2.2 Density Fluctuation Statistics

Toner-Tu theory provides remarkably precise and easily-tested predictions about the statistical properties of density fluctuations in flocks. Beyond predicting the scaling exponent for giant number fluctuations (Eq. 1.9), it also asserts that the scaling coefficient depends on the specific shape of the ‘counting box’ used to measure these fluctuations [117]. According to the theory, giant number fluctuations follow the scaling relation:

$$\sqrt{\langle \delta N^2 \rangle} \equiv \Delta n = K' \langle n \rangle^\alpha, \quad (4.1)$$

where $\alpha = 0.8$ and K' is a shape-dependent factor that scales with the aspect ratio

$$\beta = \frac{\ell_{\parallel}}{\ell_{\perp}}, \quad (4.2)$$

in which ℓ_{\parallel} and ℓ_{\perp} represent the lengths of the counting box parallel and perpendicular to the flocking direction, respectively. The theory predicts that this shape dependence follows the relation:

$$K' = \beta^{-1/5}. \quad (4.3)$$

As shown in Fig. 4.5a, the sperm cell flock exhibits giant number fluctuations with a scaling exponent of 0.74, which is remarkably close to the theoretical prediction of $\alpha = 0.8$. Additionally, the magnitude of the fluctuations decreases as the counting box becomes increasingly elongated along the flocking direction, approaching the shape of a ‘needle’. Although the precise scaling with β deviates quantitatively from the predicted value (Fig. 4.5a, inset), the qualitative agreement with Toner-Tu theory is striking, demonstrating the robustness of its predictions even in strongly fluid-coupled systems. These anomalous, anisotropic density fluctuations arise in Toner-Tu theory

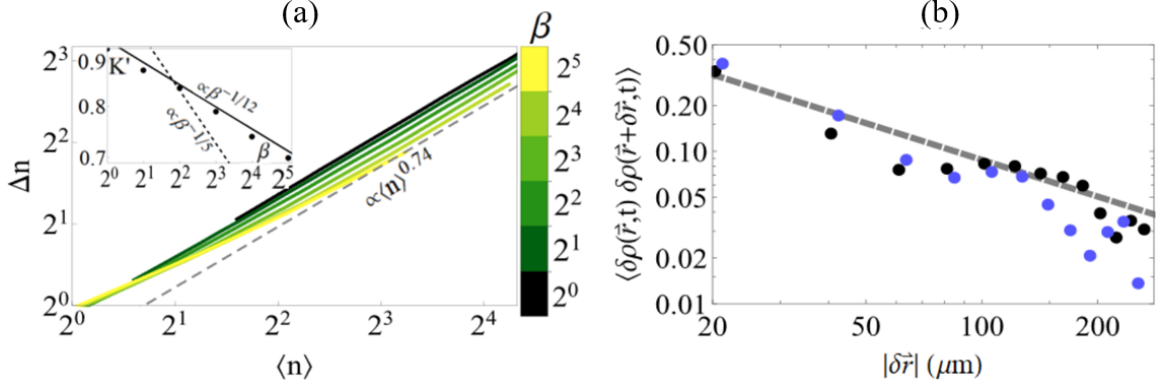


Figure 4.5: **Density fluctuation scaling in flocking states.** Data shown here was obtained from flocks of sperm cells with the largest polar order values (highest densities) from Fig. 4.4. (a) The giant number fluctuation scaling is shown when fluctuations are computed within boxes of aspect ratio β (Eq. 4.2); for each value of β , the scaling was fit to Eq. 4.1, and the value of K' is plotted in the inset. (b) Density fluctuation correlation function measured in boxes separated by a distance $|\delta\mathbf{r}|$ parallel to the flocking direction, $\delta\mathbf{r} = |\delta\mathbf{r}|\mathbf{e}_{\parallel}$ (black), and boxes separated in the transverse direction, $\delta\mathbf{r} = |\delta\mathbf{r}|\mathbf{e}_{\perp}$ (blue). The prediction from Eq. 4.4 is denoted by the dashed grey line.

from long-ranged correlations of the form

$$\langle\delta\rho(\mathbf{r}, t)\delta\rho(\mathbf{r} + \delta\mathbf{r}, t)\rangle \propto |\delta\mathbf{r}|^{-\alpha}, \quad (4.4)$$

where $\alpha = 0.8$. Directly measuring this correlation function is challenging [70], but we find reasonable agreement with our experimental data Fig. 4.5b.

These results demonstrate that, at very high cell densities, wet active matter systems with hydrodynamically coupled cells may still be described by standard Toner-Tu theory. What about at lower densities though, where the system develops significant vorticity (Fig. 4.4b)? In the following section I discuss how one can con

4.2.3 Persistent Turning Particle Model

The mechanism underlying the vortex-flocking transition in our experiments remains an open question. Direct numerical simulations of wet active matter systems become computationally prohibitive as the number of agents increases, owing to the necessity of calculating both fluid momentum and long-range particle-particle interactions. Consequently, when studying collective dynamics involving thousands to millions of interacting agents, it is essential to adopt a coarse-grained description [47] that captures the effects of hydrodynamic interactions [34].

The persistent turning model offers a useful framework for describing microswimmers that continuously reorient while maintaining a characteristic trajectory curvature [75]. In this model, particle positions are updated via self-propulsion as in Eq. 2.14, while their orientational dynamics evolve according to:

$$\dot{\theta}_i(t) = \frac{1}{|\mathcal{N}_i|} \sum_{j \in \mathcal{N}_i} \sin(\theta_i - \theta_j) + \omega_i(t) \quad (4.5)$$

$$\dot{\omega}_i(t) = -\frac{1}{\tau} \omega_i(t) + \sqrt{\frac{2}{\tau}} \sigma_\omega \zeta_i(t), \quad (4.6)$$

where \mathcal{N}_i is the set of neighbors within a radial distance ℓ with which the i^{th} cell aligns its orientation, θ_i . The rotational noise ω_i obeys an Ornstein-Uhlenbeck process, with ζ_i a zero mean, unit variance Gaussian, that is characterized by the persistence time τ and standard deviation σ_ω . The correlations $\langle \omega(t) \omega(t') \rangle \propto e^{-(t-t')/\tau}$ of the rotational noise introduces persistent turning to the model, which at sufficiently large τ and small σ_ω may compete with the alignment interactions to produce macroscopic vortex phases [75]. This model has been successfully applied to study various forms of self-organized collective behavior, including vortex lattice formation in microtubule suspensions [107], collective oscillations in *E. coli* suspensions [22], dynamic network formation in *C. elegans* [106], and vortex crystallization in *S. marcescens* suspensions

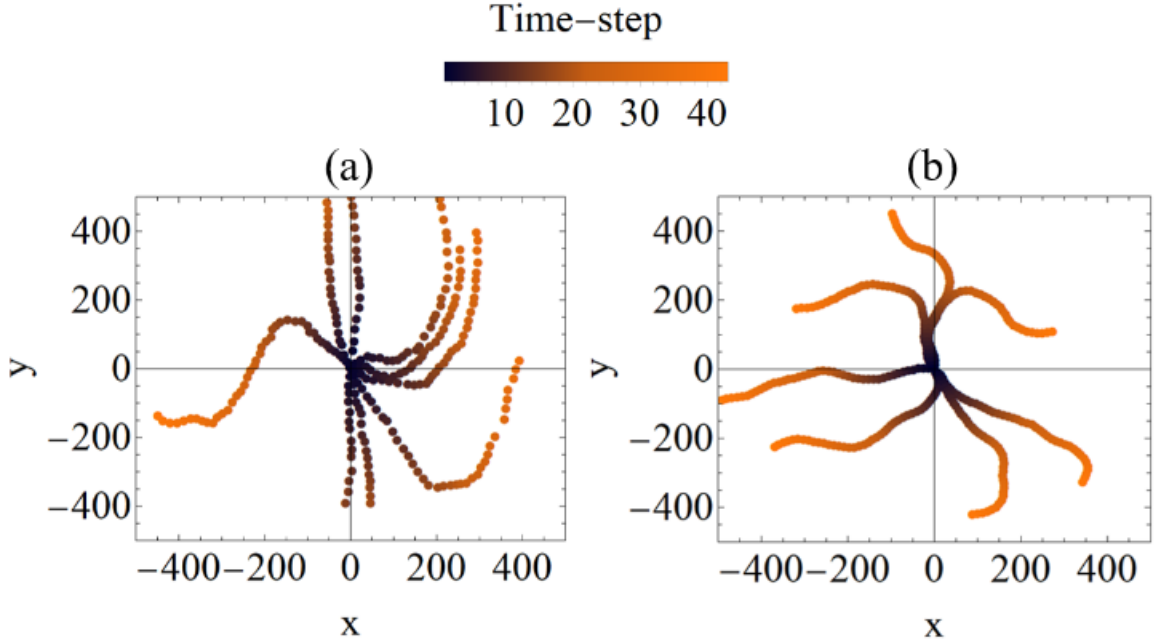


Figure 4.6: **Experimental and model trajectories.** (a) Trajectories of dilute, isolated cells from our experiments. (b) Trajectories from our simulations of Eqs. 2.14,4.5,4.6 that were fit to the experimental data.

[130]. The persistence time plays a key role in this model’s vortex-forming phase behavior. When $\tau = 1$, particles “forget” their current rotational frequency at each time-step, and the dynamics of θ_i are dictated by polar alignment interactions. At large values of τ though, ω_i becomes correlated in time and introduces a persistent turning, rotational motion to θ_i that compete with polar alignment.

Here, we seek to use this model to understand the vortex phase that arises in Fig. 4.3b. To do so, we fit the free parameters in Eqs. 2.14,4.5,4.6 to the experimental data in dilute conditions where cell motion is dominated by the random swimming motion of isolated cells. The self-propulsion speed (v_0) is estimated by the sample mean displacement of cells’ heads between successive video frames. The estimates for the noise strength (σ_ω) and memory time (τ) are obtained by fitting the statistics of θ_i to an Ornstein-Uhlenbeck process [82]. As shown in Fig. 4.6, this fitting procedure yields smoothly curving trajectories that qualitatively resemble those observed in

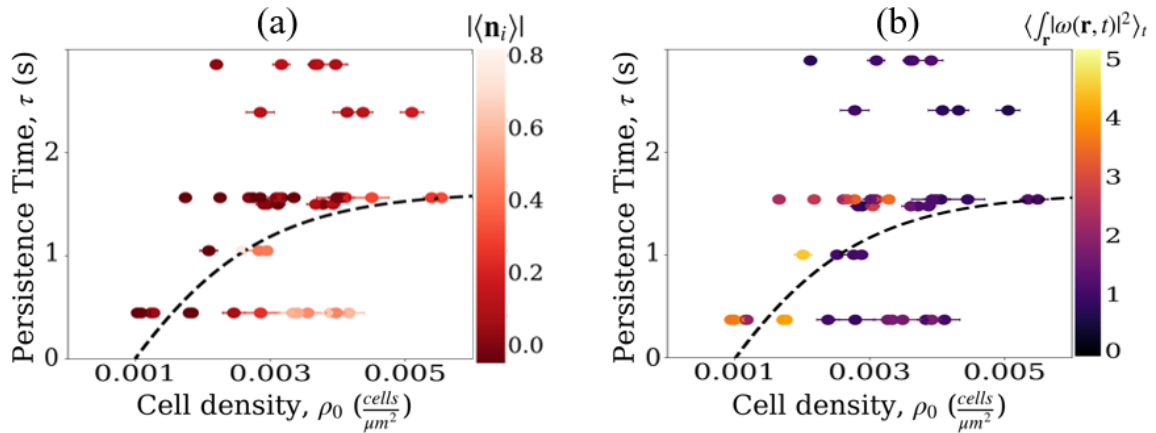


Figure 4.7: **Vortex to flocking phase diagram.** The same data as in Fig. 4.4 is shown here, but with polar and vortex order parameters now shown as a function of both cell density and persistence time. Dashed black line denotes the order-to-disorder transition line obtained from simulations of Eqs. 4.5-4.6.

experiments.

4.2.4 Vortex-Flocking Phase Diagram

Having identified cell density and persistence time as likely control parameters in our toy model of sperm cell vortex and flocking states, we compare the theoretical phase boundary with experimental observations. Fixing the self-propulsion speed and noise strength in our model, we systematically study the $\rho_0 - \tau$ phase diagram and find a line of critical points that separate polar flocking states and globally disordered states. In Fig. 4.7 I show that the phase boundary is remarkably close to the phase boundary separating vortex and flocking states in our experiments.

4.3 Conclusion

In this chapter, we have demonstrated that long-lived flocking states of *Bos taurus* sperm cells can be induced through transient pulsed flow in a viscoelastic medium. The emergent collective behavior is well-captured by numerical simulations of a persistently turning variant of the Vicsek model, which accounts for the intrinsic long-

lived orientational correlations observed in individual sperm trajectories within this quasi-2D environment. Notably, we have also identified giant number fluctuations and transverse density correlation statistics that align, both qualitatively and quantitatively, with the expectations of Toner-Tu theory [117].

This agreement between experimental observations and theoretical predictions is particularly noteworthy given that Toner-Tu theory, in its original formulation, neglects momentum conservation between self-propelled agents and their surrounding fluid. Such an omission is significant for microswimmers, where hydrodynamic interactions are non-negligible. Prior theoretical work has suggested that flocking should be inherently unstable in low-Reynolds-number active fluids [1]. The persistence of collective order in our system, despite these constraints, may be partially explained by the proximity of sperm to a solid substrate, which alters the surrounding hydrodynamic field [97]. However, substrate-induced damping would also be expected to reduce the sperm-sperm alignment interactions that facilitate collective motion [56]. Another intriguing possibility is that sperm cells may directly transfer momentum to the substrate, a hypothesis that has been proposed for decades in biological studies [89] but remains without definitive quantitative validation. The results presented here provide new evidence in support of this hypothesis, although further investigation is required to conclusively establish its role.

Beyond the physical mechanisms underlying these collective states, the broader biological implications of the observed swimming patterns remain uncertain. While collective motion is widely observed across biological systems spanning many length scales, the functional significance of sperm flocking or vortex states is unclear. Our experiments, conducted in a biologically relevant viscoelastic medium under transient pulsed flow, reveal that sperm exhibit prolonged polar order, consistent with predictions from Toner-Tu theory. However, in physiological settings, sperm navigate complex, three-dimensional environments en route to fertilization. Recent work

on active fluids on curved surfaces [103]—such as epithelial cell motion along the gut [97]—has prompted extensions of Toner-Tu theory to account for topological constraints [102]. By analogy, the azimuthal flocking modes predicted in tubular geometries [102] may suggest a potential biological function for the vortex phase, such as acting as a transient storage or reservoir mechanism for sperm cells.

Finally, our findings bear relevance to agricultural assessments of male fertility. While human sperm motility is typically evaluated via optical microscopy, such tools are often unavailable in field settings for livestock breeding. Instead, *mass motility*—the collective movement of sperm cells—has been employed as a crude diagnostic for fertility [32]. However, this approach is often unreliable, as sperm concentration and collective swimming speed are not always positively correlated [63]. The mechanisms governing mass motility remain poorly understood, with evidence suggesting contributions from both intrinsic sperm properties, such as head morphology [15, 85], and extrinsic factors, including fluid rheology [53]. The results presented here provide a novel approach to assessing mass motility by linking it to the fundamental swimming dynamics of individual sperm, offering a more mechanistic perspective on the emergence of collective sperm motion.

Chapter 5

Deep Learning the Heterogeneous Dynamics and Morphology of Follower/Leader Cancer Cells

All of the systems discussed in this dissertation up to now have been composed of only a single “species”. In nature though, heterogeneous populations interact with each other (e.g., via cooperation or competition) at both microscopic and macroscopic scales. A particularly striking and highly relevant example of heterogeneous interacting active agents is the case of metastatic tumors. These tumors are not composed of a single type of cancer cell, but instead a diverse micro-ecosystem where cancerous cells differentiate into distinct ‘leader’ and ‘follower’ subpopulations [128, 91]. Leader cells (LCs) play a critical role by creating pathways through the extracellular matrix (ECM), enabling tumor invasion toward nearby blood vessels and facilitating metastasis (see Fig. 5.1). The precise role of follower cells remains under investigation, with some studies suggesting they are merely non-invasive cancer cells and others proposing that they actively support leader cell proliferation [62]. There is clear evidence, however, that the interactions between leader and follower cells exhibit non-reciprocal

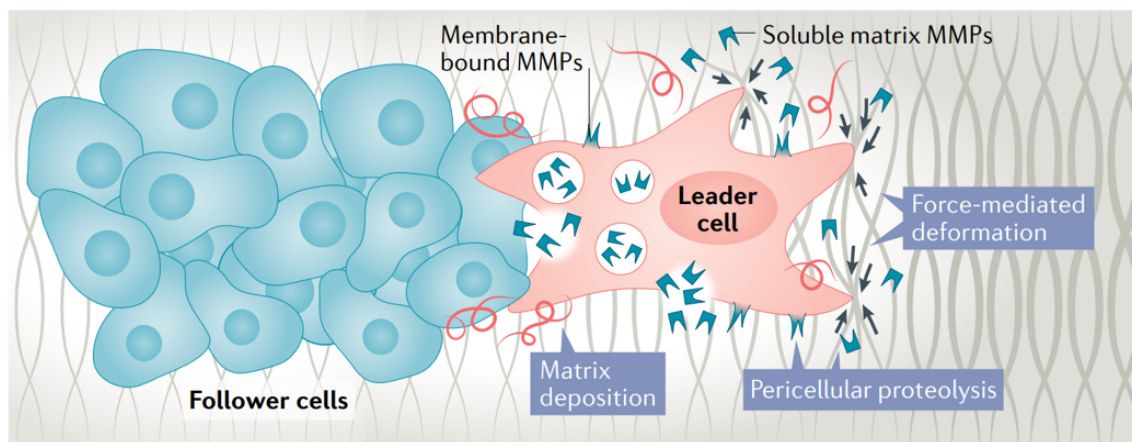


Figure 5.1: **Schematic diagram of the role LCs play in cancer invasion.** Pericellular proteolysis is used to degrade the ECM and then forcibly deform the ECM in order to create spaces for them to elongate into. LCs also deposit matrix components such as fibronectin as they generate low-resistance tracks, which provides adherence sites that enhance follower cells mobility (Figure taken from Ref. [128]).

interactions with one another at a coarse-grained level [50]. The presence of leader cells complicates cancer treatment, as conventional chemotherapy can inadvertently increase the proportion of aggressive leader cells in the tumor microenvironment [61].

This chapter focuses on the cooperative interactions among heterogeneous cancer cell populations within the tumor microenvironment, exploring methods for learning coarse-grained representations of these interactions, and how such representations can enhance our understanding of tumor metastatic potential.

5.1 Introduction

In this section, I review the diversity of biological settings in which emergent leader-like behavior manifests, and their relevance to clinical outcomes. The existing active matter frameworks for studying the dynamics of leader-induced multi-cellular streaming are then discussed, as well as the areas in which future work can improve on.

5.1.1 Follower and Leader Cell Heterogeneity

As previously mentioned, leader cells are vaguely defined by their functional role of generating low-resistance tracks through which other follower cells may invade out from the primary tumor [17]. The lack of a more formal definition is due to the sheer variety of ways that leader cells can manifest [128]; in fact, in a variety of settings the leaders are not cells at all but rather cancer-associated fibroblasts [7, 37, 94]. Leader-like activity has even been reported in wound healing of healthy tissue [80, 33]. Additionally, leader cell specialization is not restricted to cancers in any particular bodily location, and has been experimentally observed in brain [79], breast [86, 139], bladder [119], and lung [62, 108] cancer cells. Across these diverse settings though, ‘leaders’ are consistently identified as a sub-population of cells with uniquely persistent trajectories that stimulate the activity of nearby cells.

Regardless of the exact setting and bio-chemical mechanism by which leader and follower cells interact with one another, the macroscopic phase behavior of the tumor that arises from their interactions remains effectively the same: starting from a uniform configuration (i.e. a spheroid or a monolayer sheet), leader cells appear at the interface of the cells and the surrounding medium and generate invading multi-cellular streams. In wound-healing experiments on scratched monolayers of healthy tissues, this behavior is referred to as ‘fingering’ [101] because of its resemblance to the viscous fingering at the interface of two equilibrium fluids. In tumor metastasis experiments, this behavior is called ‘collective invasion’ [139]. This collective behavior is not a generic feature of homogeneous cellular aggregates, but rather has been directly attributed to the presence of leader cells. As shown in Fig. 5.6, a tumor composed solely of follower cells is non-invasive and remains stationary over time. As leader cells are introduced though, multi-cellular streams of cells begin protruding from the tumor. *In vivo* experiments have found that the tumors exhibiting multi-cellular streaming of cells are highly correlated with proximity to blood vessels, whereas tumors with

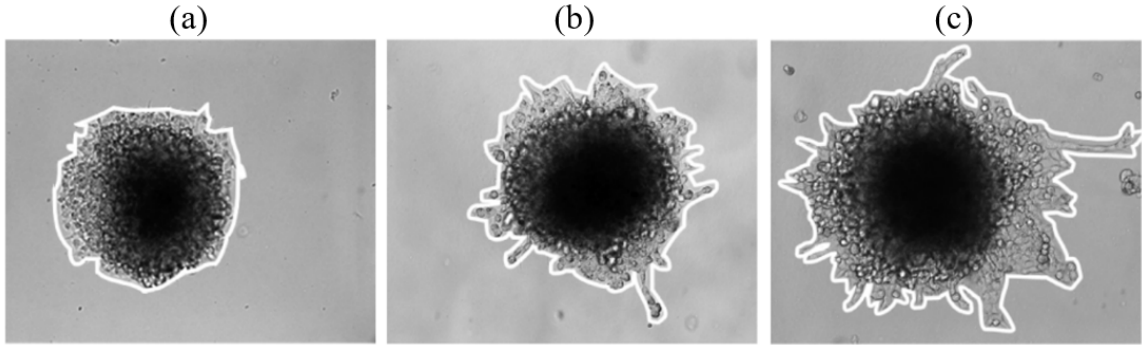


Figure 5.2: **Functional role of leaders.** Snapshots of three different tumors composed of all follower cells except for a leader cell population fraction of 0%, 1% and 10% in (a)-(c) respectively. Images are taken 48 hours after spheroid are initially implanted in an extra cellular matrix composed of collagen. Figures taken from Ref. [62].

only single cell invasion have no proximity correlation, suggesting that this mode of collective dynamics is a key step in tumor metastasis [84].

While the functional role of leader cells is intuitive and ubiquitous, that of follower cells is less clear. In some experiments on breast cancer cells, leaders were found to effectively just be high-energy followers which, upon depleting their energy, exchange positions and roles with a trailing follower [139]. In other experiments on lung cancer cells, followers secreted a chemical (VEGF) that reduced the number of error made by leaders during mitosis (Fig. 5.3). This latter case is particularly interesting because follower cells are not passive agents, but instead interact cooperatively with leader cells and can be essential for sustained collective invasion [62, 50].

A natural question that arises from these observations is: can one can construct a phenomenological theory of tumor metastasis for a binary of system of follower and leader cells with non-reciprocal interactions? And subsequently, could we use such a model to better understand the mechanical instability that leads “collective invasion”? In the next section, I review some approaches taken in the literature to construct minimal agent-based and hydrodynamic models of leader-cell-induced collective invasion.

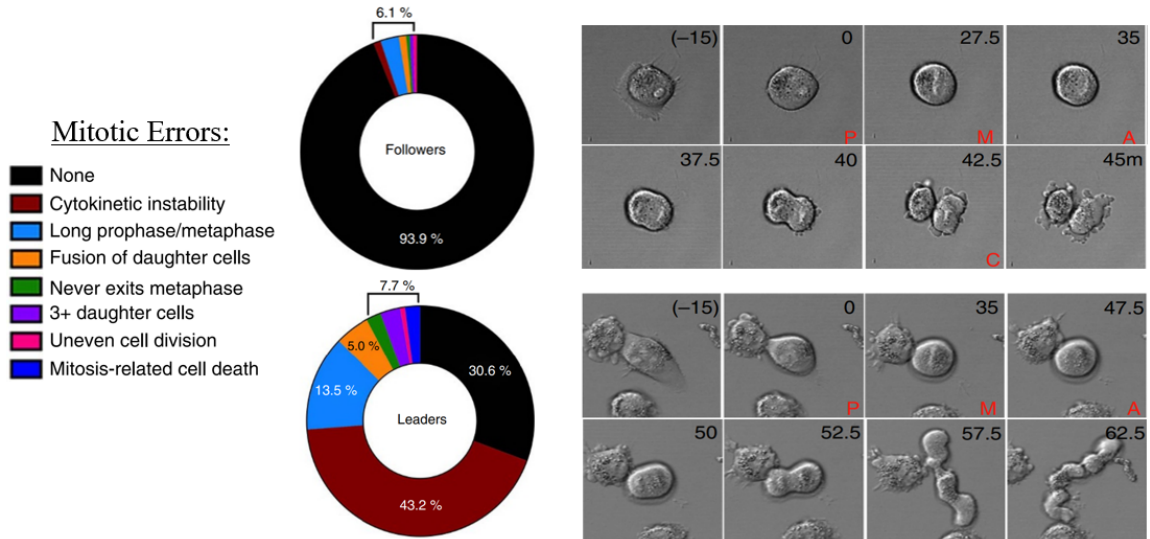


Figure 5.3: **Functional role of followers.** Pie charts show how often follower and leader cells (in isolation) make mitotic errors. Follower cells rarely make errors during cell division, while leaders are plagued by instabilities that result in cell death. Figures taken from Ref. [62].

5.1.2 Minimal Models of Monolayer Migration

The simplest agent-based model that statistically captures the collective motion of cells in a confined, actively moving epithelium is [101]

$$\frac{d\mathbf{v}_i}{dt} = -\alpha\mathbf{v}_i + \sum_j \left[\mathbf{f}_{ij}^{\text{alignment}} + \mathbf{f}_{ij}^{\text{att-rep}} \right] + \sigma\boldsymbol{\eta}_i, \quad (5.1)$$

where the noise ($\boldsymbol{\eta}_i$), representing a random motility force generated by the cell, evolves via an Ornstein-Uhlenbeck process (as in Chapter 4.2.3)

$$\frac{d\boldsymbol{\eta}_i}{dt} = -\frac{1}{\tau}\boldsymbol{\eta}_i + \sigma\boldsymbol{\zeta}_i. \quad (5.2)$$

In addition to capturing the statistical behavior of cells in the ‘bulk’ of an epithelium [101], it also contains the essential ingredients to spontaneously generate multi-cellular streams [99].

There have been several attempts to reproduce experimentally observed epithelial

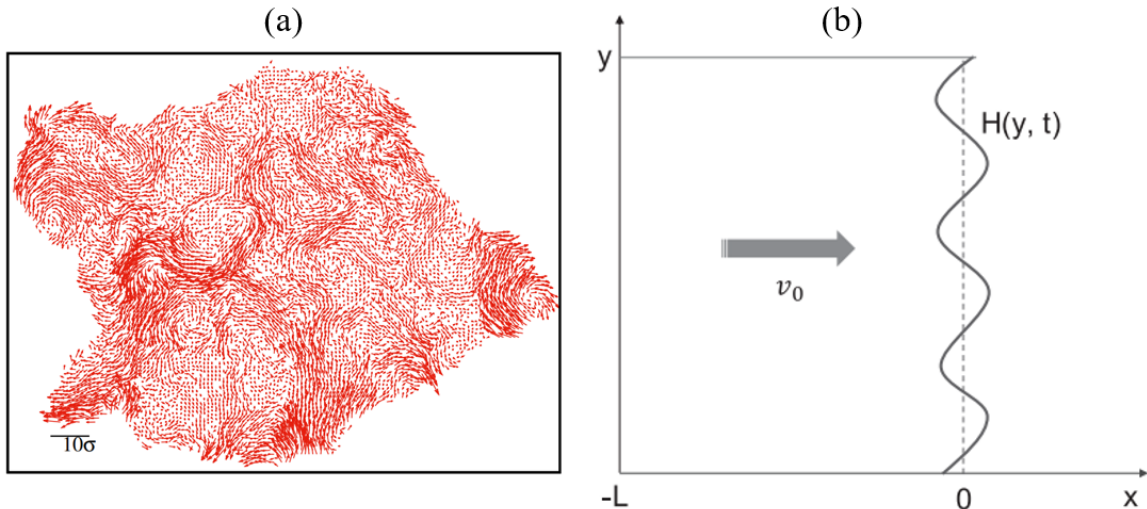


Figure 5.4: **Agent-based and hydrodynamic models of leader-cell invasion.** (a) Simulation snapshot of a variant of Eqs. 5.1-5.2, showing local polarization of ‘bulk’ cells and protruding streams of cells. (b) Schematic of a minimal hydrodynamic model of multi-cellular streaming. Figures taken from Ref. [99] and Ref. [133] respectively.

fingering during wound healing with this model [101, 116]. However, in order to capture the structure of the epithelial fingers – e.g. a decreasing cell density from the bulk to the tip of a stream and a highly polarized velocity field – several additional terms need to be added to the model which, while biologically motivated, are rather arbitrary and *ad hoc* in their implementation [116]. In the same vein, one can include information about the role of cell rheology in multi-cellular streaming and study shape-based cell dynamics, as in the vertex model [111, 112], but parameter phase space is so large when doing so that a systematic study of it is intractable [66].

Even with just Eqs. 5.1-5.2, the cell-cell interaction term, $\sum_j [\mathbf{f}_{ij}^{\text{alignment}} + \mathbf{f}_{ij}^{\text{att-rep}}]$, alone can have up to eight free parameters itself, in addition to the other three free parameters $\{\alpha, \sigma, \tau\}$. Some studies have carefully tuned these parameters to obtain simulations that reproduce experimental observations [101, 116], but their physical meaning is ambiguous. The conventional method to circumvent the issue of a large parameter space in agent-based models is to instead study the coarse-grained dynamics of the agents’ density and velocity fields.

For example, one model of leader-driven multi-cellular streaming is a modified Toner-Tu theory (Eqs. 1.13-1.12) which imposes incompressibility condition

$$\nabla \cdot \mathbf{v} = 0, \quad (5.3)$$

and takes the transport coefficient α in the free energy functional (Eq. 1.13) to be

$$\alpha(f) = a_0 + f a_1, \quad (5.4)$$

where f is a curvature based force that decays away according to

$$\frac{\partial f}{\partial t} = -r f + D_f \nabla^2 f, \quad (5.5)$$

but which has the boundary condition on the leading front

$$f|_{\text{leading front}} = q^2 h. \quad (5.6)$$

Eqs. 5.4-5.6 represent a phenomenological description of leader cell dynamics in that the leading edges of the active fluid, where leader cells are typically found, have higher levels of activity (α) than the bulk fluid [133]. Other hydrodynamic models have found that multi-cellular streaming arises from more conventional mechanisms such as cell-substrate friction [121] or a kinematic instability [4]. Some models even take into account cell-division and consider a growing tumor invading a passive surrounding fluid [13].

Still absent in the literature is an experimentally informed model of multi-cellular streaming that fully takes into account the non-reciprocal interactions of follower and leader cells. A key difficulty in constructing such a model is that the complexity of Eq. 5.1 was substantial even for a single-species of cell. Constraining the parameter

space of a two-species model would be a significant challenge. Another issue is that even if we could write down such a model and fit it to experimental data, the values that get will be ambiguous and arbitrary to the specific functional forms we choose to constrain the cell-cell interactions to. In the following section, I discuss a potential method that, rather than asserting a specific model and fitting it to data, instead leverages neural networks to “discover” symbolic forms for the interactions governing monolayer cell dynamics.

5.2 Methods

In this section I review the theory of force inference neural networks [29], and then discuss my application of it to living cellular monolayers. The experimental system considered here is not the two-population follower/leader systems of cancer cells previously discussed, but a single-species population of MDCK cells in a monolayer. The implementation is available as a *Python* package at <https://github.com/crpackard/monolayer-gnn>.

5.2.1 Force Inference Graph Neural Network

The method we use is motivated by Cranmer et al.’s work in Ref. [29], in which they designed a graph neural network model that could learn approximate symbolic expressions for the interactions between particles from solely their trajectory data. Within the model, each particle is represented as a graph node, as schematically depicted in Fig. 5.5a. Each node is equipped with a *feature vector* containing a list of degrees of freedom that the interaction between pairs of particles may depend on, say, position and velocity

$$\mathbf{n}_i(t) = \{\mathbf{r}_i(t), \mathbf{v}_i(t)\}. \quad (5.7)$$

Each node is also given a *label vector* containing the degrees of freedom that we wish to predict, say, acceleration \mathbf{a}_i . The neural network is then trained to learn the pair-wise interaction, $\phi(\mathbf{n}_i, \mathbf{n}_j)$, which (when summed over all interacting neighbors) predicts the label vector. In the case where one is predicting the accelerations of particles via

$$\mathbf{a}_i^{\text{predicted}}(t) = \sum_{j \in \mathcal{N}} \phi(\mathbf{r}_i(t), \mathbf{v}_i(t), \mathbf{r}_j(t), \mathbf{v}_j(t)) \quad (5.8)$$

the pair-wise interaction can be directly interpreted as Newtonian-like forces. If this graph neural network model can be trained to predict the instantaneous acceleration of all objects in a system, then ϕ becomes equivalent to a high-dimensional representation of the pair-wise interaction. Methods such as symbolic regression can then be used to approximate ϕ with a low-dimensional functional expression that can be further analytically studied.

In Cranmer et al.’s work, this force inference technique was applied to synthetic datasets of particles interacting via classical forces such as harmonic, gravitational, Coulomb forces, etc., and the graph structure is trivially all-to-all. In my work, I apply force inference to cellular monolayers which have a significantly more complex graph structure (see Fig. 5.5b). In the following section I review how I employ segmentation and tracking models to construct these monolayer graphs and extract cell features.

5.2.2 Trajectory Extraction

My *Python* package (<https://github.com/crpackard/monolayer-gnn>) extracts single-cell trajectories from microscopy videos of monolayers by creating a pipeline that passes raw video data, frame-by-frame, through a segmentation model [105], after which a probabilistic Bayesian inference neural network tracks individual cell identities across sequential frames by comparing their segmentations [125]. An example output of the segmentation model is shown in Fig. 5.6a, and the tracked motion of

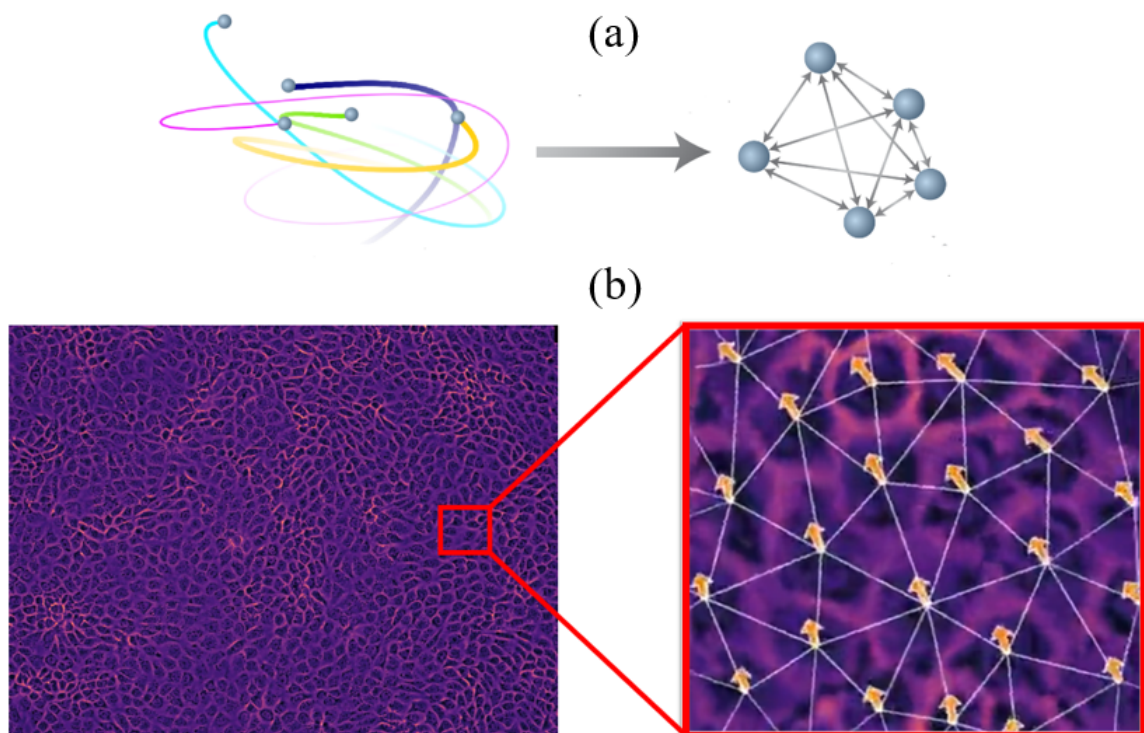


Figure 5.5: **Graph construction.** Schematic example of how (a) an ensemble of simple particles are mapped to an all-to-all graph in Ref. [29], and (b) an monolayer of cells are mapped to a Voronoi graph in our work (white lines denote graph edges and orange arrows denote cell velocities).

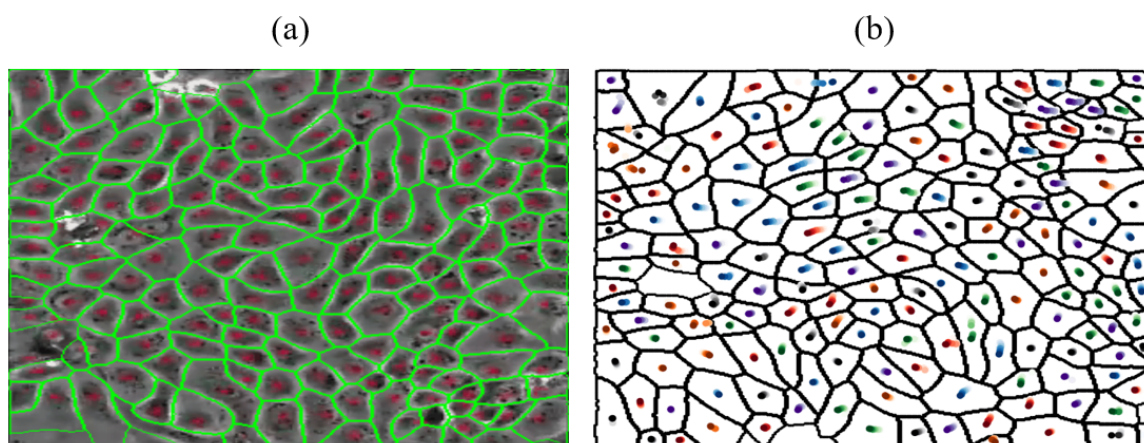


Figure 5.6: **Example of segmentation and tracking in a 2D monolayer.** (left) A snapshot of a monolayer of cells from an experiment is shown with the cytoplasm boundary contours predicted by a segmentation model shown in bright green. (right) The computationally tracked trajectory of each cell contour from the left plot is shown here, denoted by sequences of randomly colored circles at cells' centroids.

the cells in Fig. 5.6b.

The output of the above process is a time-series of cell contours for hundreds or even thousands of cells. Seeking a particle-based representation of cells, we define cell dynamics in terms of the centroid, $\mathbf{r}_i(t)$, of each cell. The instantaneous velocity and acceleration of a cell is then defined using finite-differences as

$$\mathbf{v}_i(t) \approx \frac{\mathbf{r}_i(t + dt) - \mathbf{r}_i(t)}{dt} \quad (5.9)$$

and

$$\mathbf{a}_i(t) \approx \frac{\mathbf{r}_i(t + dt) - 2\mathbf{r}_i(t) + \mathbf{r}_i(t - dt)}{dt}. \quad (5.10)$$

This information alone is sufficient to train a model via Eq. 5.17 and seek an effective force law – or, equivalently, an intercellular potential – between cells.

In traditional cellular models, like the Voronoi and vertex models [111], one would now resort to computing the set of neighbors (i.e. graph edges, \mathcal{N}) in Eq. 5.17 using the instantaneous configuration of centroid positions. This method yields graphs that like in Fig. 5.5b. Here though, we have access to the full cell contour data which allows us to not only measure which cells are in physical contact with each other, but also quantify the degree of contact. For example, in Fig. 5.7 I train a segmentation model to identify the nuclear boundary (rather than the cytoplasmic boundary) of each cell, and then evaluate the lines of contact between all nuclei.

The cell contour data can be used for more than quantifying the connections between cells. We can, for example, instead of coarse-graining cells into point particles, we could instead coarse-grain them into ellipses defined by

$$\frac{(x' - x_0)^2}{a^2} + \frac{(x' - y_0)^2}{b^2} = 1, \quad (5.11)$$

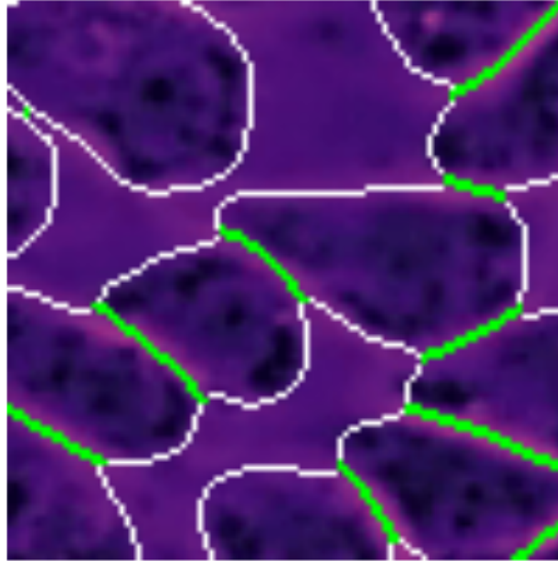


Figure 5.7: **Quantifying cell-cell contact.** While pixels denote the contours of cell nuclei in a monolayer. Green pixels denote the points that are shared between two cells.

where x' and y' are the rotated coordinates

$$\begin{bmatrix} x' \\ y' \end{bmatrix} = \begin{bmatrix} \cos \theta & \sin \theta \\ -\sin \theta & \cos \theta \end{bmatrix} \begin{bmatrix} x - x_0 \\ y - y_0 \end{bmatrix}. \quad (5.12)$$

Instead of only having a centroid (x_0, y_0) , in this representation cells are now also characterized by major (a) and minor (b) axes, and an orientation (θ). Now, instead of Eq. 5.13, we have the feature vector

$$\mathbf{n}_i(t) = \{\mathbf{r}_i(t), \mathbf{v}_i(t), a_i(t), b_i(t), \theta_i(t)\}, \quad (5.13)$$

which allows us to learn more complex representations for the interactions between two cells. An example of ellipse fits to cells of various shapes is shown in Fig. 5.8. This is only one example of a shape-based model that could be studied with the force inference technique presented here. Alternatively, we could Fourier transform the cell contour and use the first n Fourier modes as node features in the graph neural

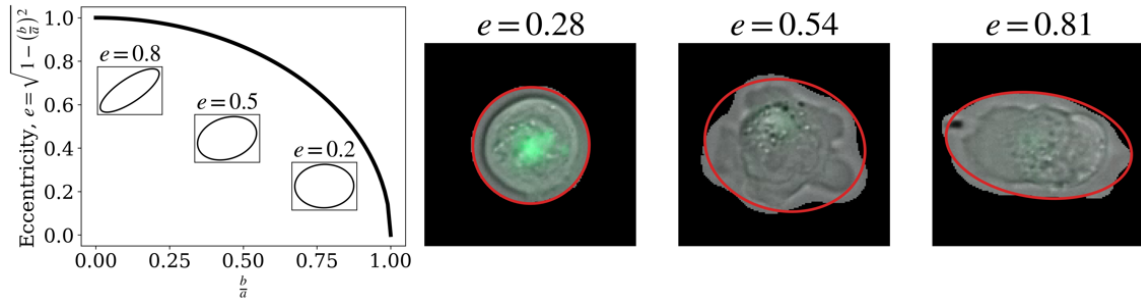


Figure 5.8: **Fitting cell shape to an ellipsoid.** (left) a plot of the eccentricity (e) of a cell as a function of the ratio of its minor axis (b) to its major axis (a), with example plots of the ellipse at representative values of b/a . (right) Fits of to segmented cells to ellipses are denoted by red lines, with the corresponding eccentricity displayed on top.

network. These ideas are pure conjecture at the moment though. Before speculating any further, in the following section I provide preliminary evidence that the graph neural network method outlined here can indeed learn effective pair-wise interactions between cells in the simple case of point particle representations, as in Eq. 5.17.

5.2.3 Proof of Concept

The limiting factor in applying the force inference graph neural network model to living tissues is the need for a substantial amount of high-resolution microscopy video data. At present, I have not been able to acquire and study a large number of datasets, but Thomas Angelini kindly shared a dataset of an MDCK monolayer in fluid-like state with which I could test the model on [27]. After extracting trajectories from all cells within the dataset, I trained a model to predict cell accelerations via Eq. 5.17. In Fig. 5.9 I show that the model does indeed learn an effective pair-wise interaction between cells that predicts their change in cell velocities. There is a nuance to this training procedure though.

Within Eq. 5.17 the time-step size dt with which one computes cell velocities and accelerations is a free parameter. When the time-lapse between successive video frames is short relative to the time-scale over which cells migrate, then the velocities

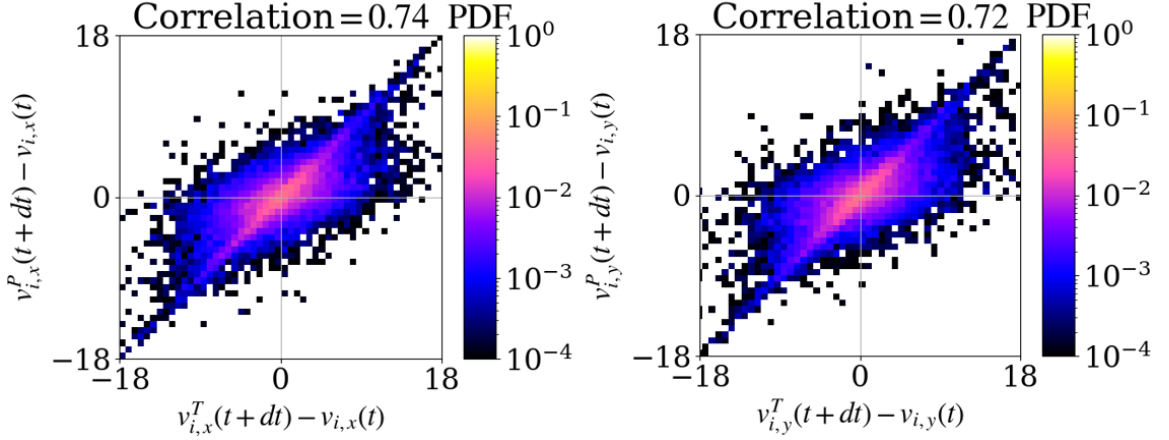


Figure 5.9: **Correlation between model predictions and observed values.** The ability of performance of a model (Eq. 5.17) at predicting in a cell’s velocity within a time-interval dt is shown. Predicted values are shown on the y -axis, and true values on the x -axis.

and accelerations of the centroid that one measures using a value of $dt = 1$ will be dominated by noisy changes in cell shape outputted by the segmentation model rather than true cell displacements. Alternatively, at time-scales that are long relative to the characteristic time-scale over which cells exchange neighbors then the observed velocities and accelerations can no longer be attributed to the interaction of their instantaneous set of neighbors. There should exist though, some optimal value of dt that resolves cell-cell interactions that produce changes in cell dynamics that are discernible from random noisy motion. In Fig. 5.10a I show preliminary data that such an optimal time-scale does indeed exist, and in Fig. 5.10b I show an example of the dynamics it predicts.

Having shown that a graph neural network can be trained to learn pair-wise interactions between cells that predicts their collective motion, we can turn to the question of exactly what interaction it learned? Here I write this interaction as

$$\mathbf{f}_{ij} = \phi(\mathbf{r}_i(t), \mathbf{v}_i(t), \mathbf{r}_j(t), \mathbf{v}_j(t)) . \quad (5.14)$$

In 2D, this interaction a function of eight parameters. However, we can invoke the

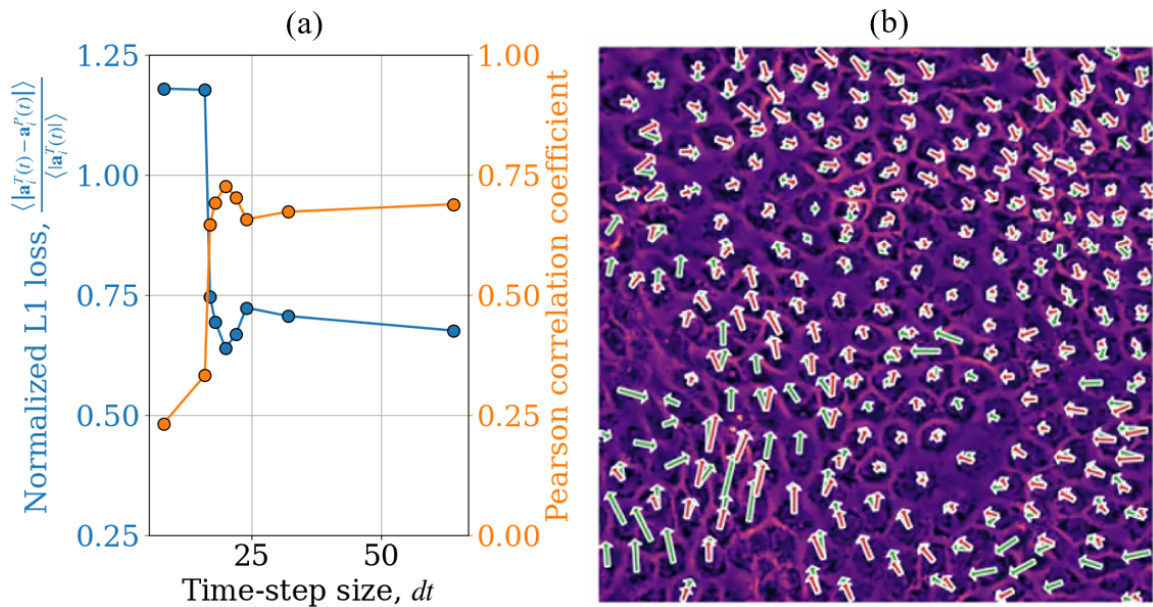


Figure 5.10: **Results of training GNNs on experimental data.** (a) The loss function and correlation coefficients of models trained via Eq. 5.17 are shown as a function of time-step size; correlation coefficients correspond to the same type of measurements as in Fig. 5.9. (b) A plot of the true cell velocities (green) and the predicted cell velocities (red) for the model with a value of $dt = 20$ that had the lowest loss value in (a). Note that cells which do not have red arrows correspond to cells that the segmentation and tracking packages were unable to track for the duration of the time interval $[t - dt, t + dt]$.

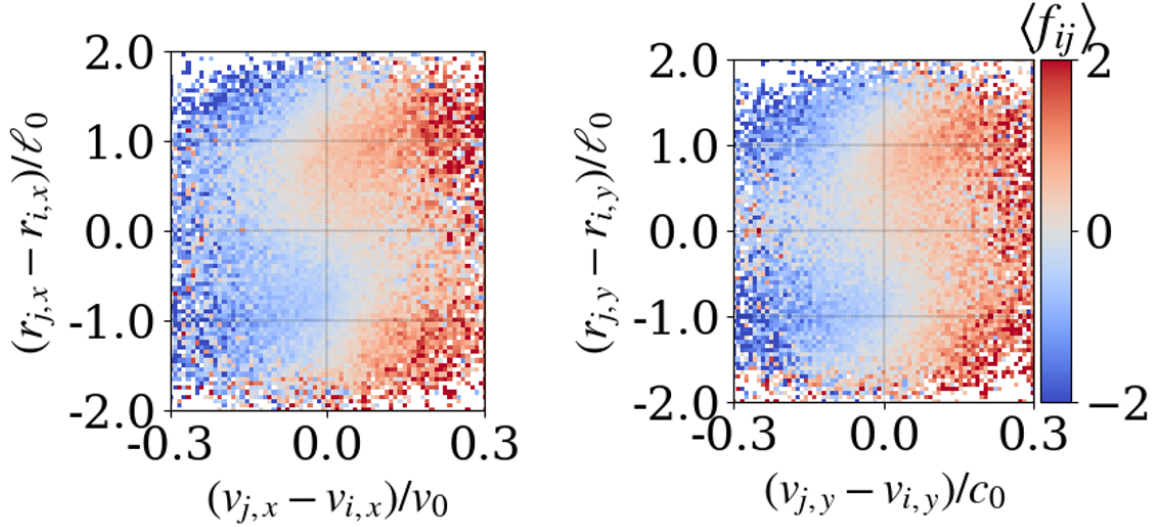


Figure 5.11: **Learned pair-wise interaction.** The x and y components of the learned force (Eq. 5.15) for the optimal value of dt in Fig. 5.10 is shown on the left and right respectively. The y -axis is scaled by the average linear size of a cell (ℓ_0), and the x -axis is scaled by the characteristic speed $v_0 = \ell/dt$.

isotropy of space to separate the x and y Cartesian components of our vectors, and we can invoke the homogeneity of space to demand that interaction depend only on the relative separation distance between cells and not on their absolute positions. Therefore, we can reduce the learned model to a function of only three variables,

$$f_{ij,k} = f_{ij,k}(r_{j,k} - r_{i,k}, v_{i,k}, v_{j,k}), \quad (5.15)$$

where $k = x, y$ denotes the Cartesian axes. In Fig. 5.11 I show the average value of $f_{ij,k}$ for the optimal value of dt in Fig. 5.10. While noisy, the data shows that there are two distinct regimes of interactions, attractive and repulsive. There is not sufficient data to fully resolve the interaction, but these results demonstrate that such inference is possible.

5.2.4 Application To Heterogeneous Follower and Leader Cell Populations

The method detailed here can be easily extended to the case of interactions between heterogeneous species of particles. For the case of collective invasion by cooperatively interaction follower and leader cells, we can denote species types by an integer $s_i = \{-1, +1\}$ and extend the feature vector in Eq. 5.13 to

$$\mathbf{n}_i(t) = \{s_i, \mathbf{r}_i(t), \mathbf{v}_i(t)\}. \quad (5.16)$$

This way, the neural network can make predictions

$$\mathbf{a}_i^{\text{predicted}}(t) = \sum_{j \in \mathcal{N}} \phi(s_i, \mathbf{r}_i(t), \mathbf{v}_i(t), s_j, \mathbf{r}_j(t), \mathbf{v}_j(t)), \quad (5.17)$$

based on interactions that depend on the combination (s_i, s_j) .

5.3 Phenotypic Heterogeneity of Follower and Leader Cells

The ideal setting in which to apply the force inference graph neural network model to study the heterogeneous interactions between follower and leader cells is the case of cells crawling in 2D on a dilute substrate. In collaboration with the Winship Cancer Institute, we conducted a series of these experiments on non-small lung cancer cells, varying the proportion of follower-to-leader cells in each experiment. After extracting cell trajectories from all experiments, we found that the data was collected at improper time-scales for a force inference analysis. Over the 15 hour interval that data was collected for, cells had migrated, on average, only half a cell diameter. This meant that we could not acquire sufficiently large datasets with reliable velocities

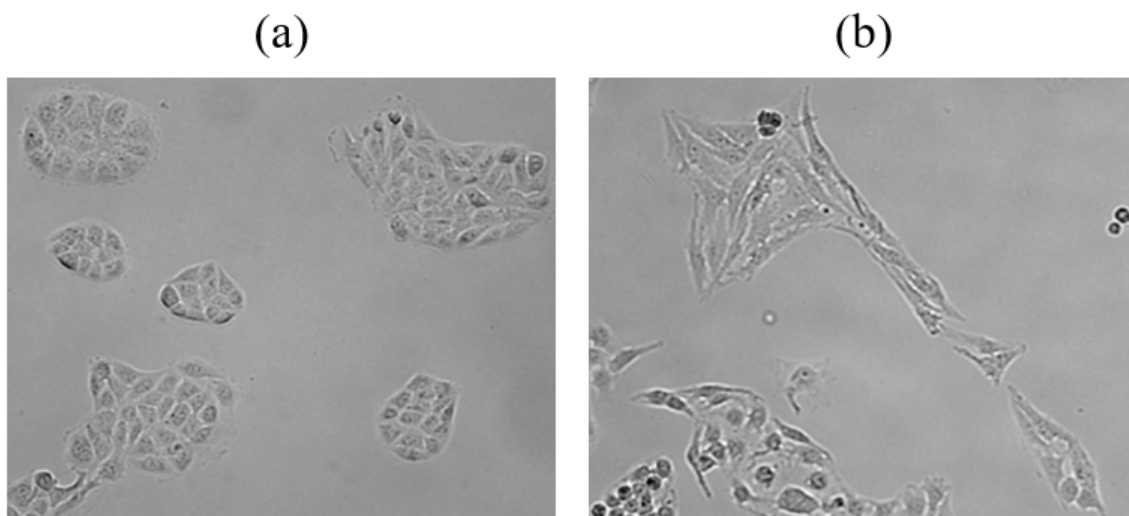


Figure 5.12: **Heterogeneity in follower and leader cell shapes.** Representative snapshots of follower and leader cells in pure, isolated populations are shown in (a) and (b) respectively. Note that leaders in (b) tend to be more elongated on average. Figure taken from Ref. [62].

and accelerations for model training. Although we could not study the cell dynamics, the experiments did provide us with a wealth of static image data to study the heterogeneity of follower and leader cell phenotypes.

As shown in Fig. 5.12, follower and leader cells do not only have heterogeneous interactions with one another, but also tend to have different morphologies. Leaders tend to be elongated and display a mesenchymal phenotype, whereas followers tend to be more round and display an epithelial phenotype [101]. Currently, this heterogeneity is not used to distinguish follower and leader cells and instead a labor-intensive genetic labeling process is used [62]. Is it possible though to build a classification model that – given only the static image data of a cell – can identify which sub-species it belongs to? In the remainder of this section I discuss some of the preliminary research I have done to explore this question.

5.3.1 Population Statistics

As a first pass at examining the differences in follower and leader cell shape in our experiments, I first look at the probability distributions of shape parameters. In Fig. 5.13 I show the distributions of cell size and shape in dilute, pure populations of follower and leaders. Separate distributions are shown for different configurations of cells: singlets, doublets, and triplets, which correspond to the number of cells interacting with each other. Data is separated this way in order to study both the shape of isolated followers and leaders and the shape differences that arise from their interactions with each other. I find that the distribution of cell areas for all configurations conforms to a Gamma distribution,

$$p(x; \alpha, \beta) = \frac{x^{\alpha-1} e^{-\beta x} \beta^\alpha}{\Gamma(\alpha)}, \quad (5.18)$$

and the distribution of cell eccentricities conforms to a Weibull distribution

$$p(x; \alpha, \beta) = \frac{\beta}{\alpha} \left(\frac{x}{\alpha}\right)^{\beta-2} e^{-(x/\alpha)^\beta}. \quad (5.19)$$

The fitted values of (α, β) clearly differ between follower and leader cells for both these distributions, and thus based purely on measuring these coarse-grained shape parameters we have some predictive ability for classifying a cell.

These distributions have currently only been measured in isolated follower and leader cell populations. Do characteristic cell shapes change co-cultures in a manner that causes the two species' distributions to converge or diverge? Or are these phenotypic differences an intrinsic property of follower and leader cells that do not in the presence of other cell species? The raw experimental data required to answer these questions has already been collected.

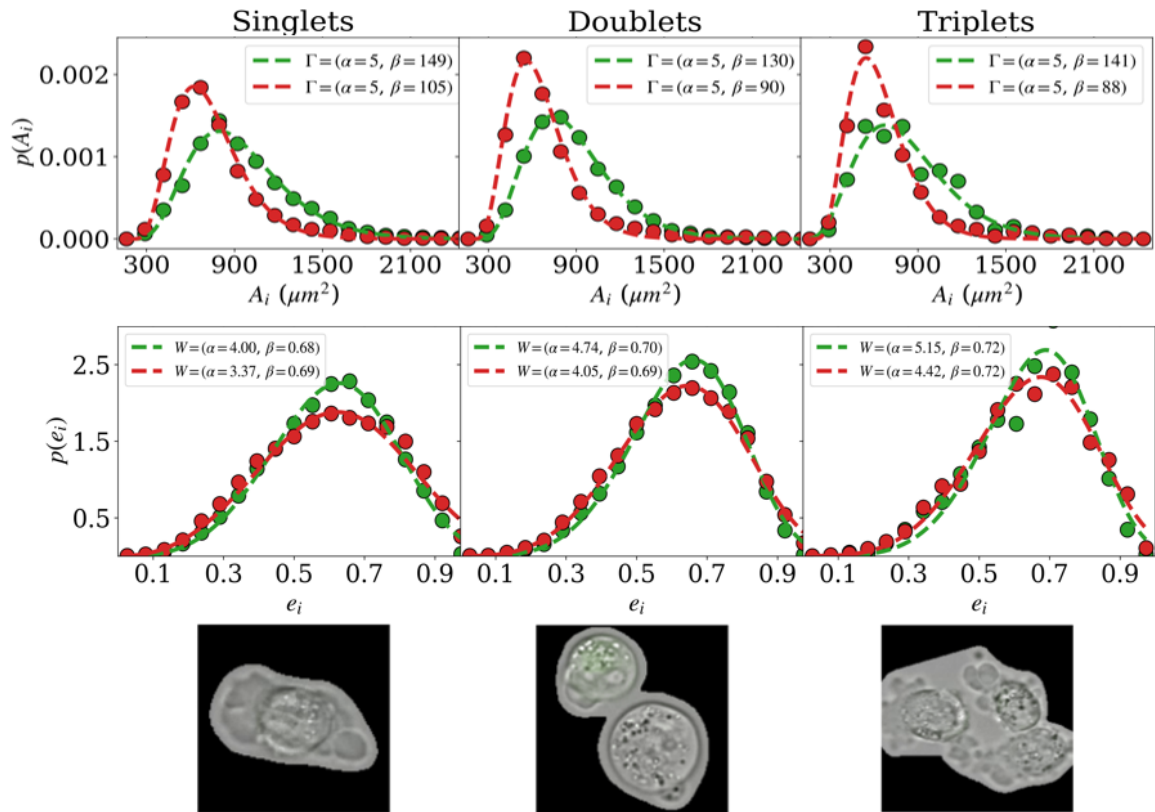


Figure 5.13: **Area and eccentricity statistics.** Data shown was collected from pure populations of either entirely follower (green) or entirely leader (red) cells. Top row shows data for the cross sectional areas of cells, where solid circles denote experimental data and dashed lines denote fits to Eq. 5.18. Middle row shows data for the eccentricity of cells, as defined in Fig. 5.8. The bottom row shows representative examples of the different cell configurations.

5.3.2 Image-Based Classification

Comparing statistical differences between populations is a very old technique in analysis of biological systems. The image data that we have collected in our experiments is also highly amenable to modern image classification neural network models. Using a pre-trained image classifier as a feature extractor, as shown in Fig. 5.14, we fine-tune the model for the task of binary classification of leader and follower cells. The model takes a 224×224 image of a single cell as input, and outputs a 2D vector, $\{p_1, p_2\}$, denoting the probability belongs to one of the two image classes (follower or leader). In our experiments, leader cells are labeled by a fluorescent chemical that we use to assign cells truth labels. The model is given gray-scaled image data without the fluorescent label so that it learns to predict cell type from the structural properties of the cell.

To test the ability of the image classifier to consistently identify cell types across multiple experiments, we train a different model for each of the seven experiments we perform, and test the performance of each one on all other datasets. In each experiment, the ratio of follower to leader cells is varied (see Table 5.1 for details). The resulting cross validation matrix is shown in Fig. 5.15. The lower bound of

Date	N_F	N_L	% leaders ^a	N_{train}^b
2023/05/08	190719	126025	N/A	252050
2023/05/30	199629	235184	N/A	399258
2023/12/04	105605	124520	54.1%	211210
2024/01/31	381109	16585	4.2%	33170
2024/02/09	26674	191731	87.8%	53348
2024/03/08	272336	135159	33.2%	270318
2024/03/12	115189	279443	70.8%	230378

Table 5.1: The number of follower (N_F) and leader (N_L) cell images collected each experiment are shown. For co-culture experiments, the experiment-averaged percentage of leader cells present is listed.

^a Defined by $N_L/(N_F + N_L) \times 100\%$; N/A for pure cultures.

^b Assuming balanced training data, $N_{\text{train}} = 2 \times \min(N_F, N_L)$.

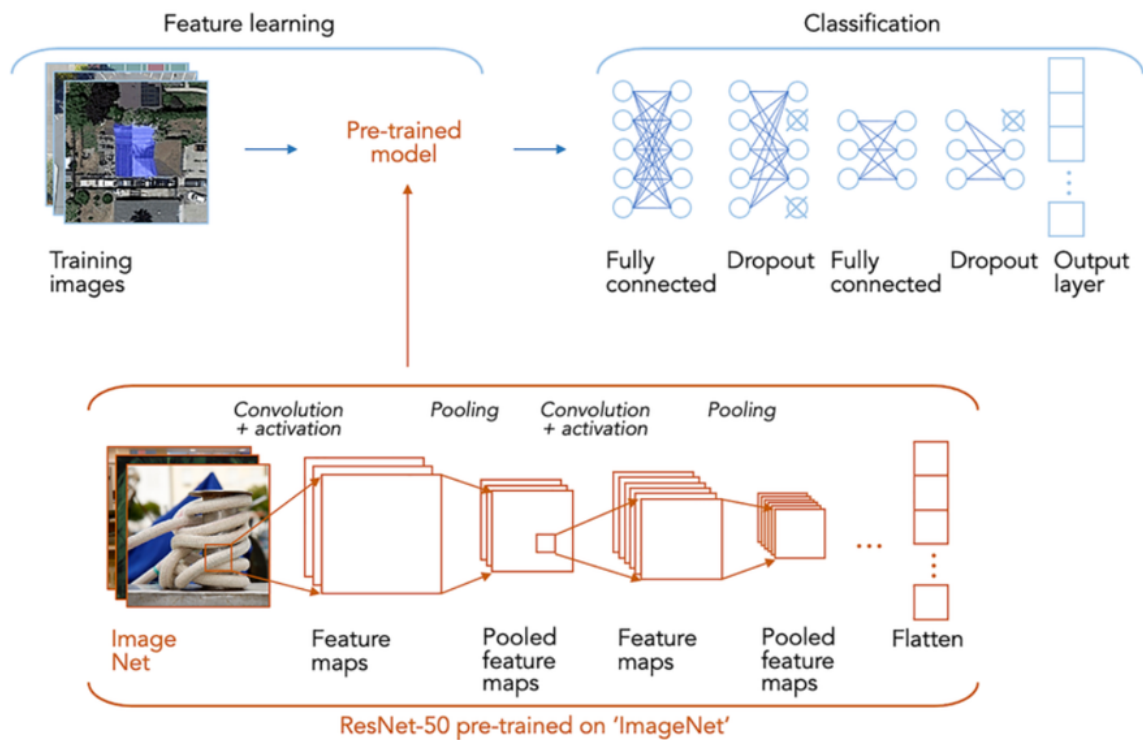


Figure 5.14: **Schematic diagram of classifier model.** We use a ResNet50 backbone that has been pre-trained on the *imagenet* dataset to detect a diverse range of features. Dense, fully-connected layers are then appended to the model to learn how to combine the features to predict the species of a cell. Figure taken from Ref. [126].

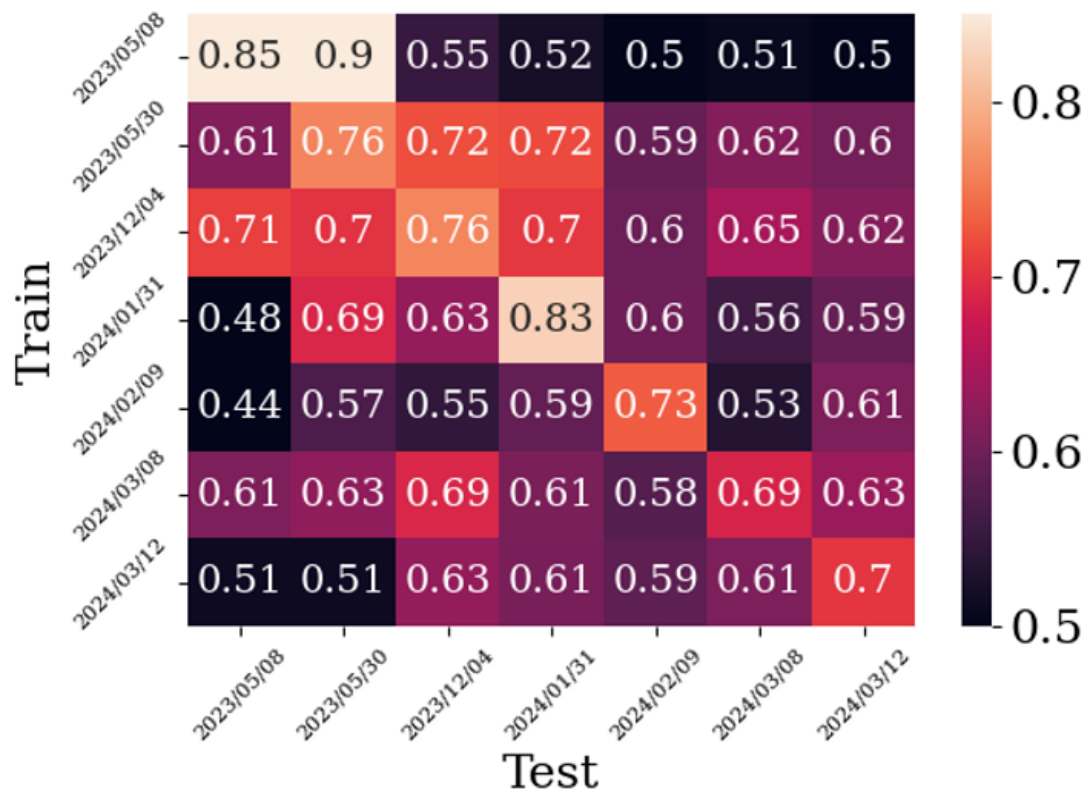


Figure 5.15: **Cross validation of image classifier model.** The classification accuracy of a model trained on one day and tested on another day is listed for all possible pairs. Training accuracy is denoted by the diagonal elements.

accuracy values is set to 0.5, i.e. the probability one would obtain if randomly guessing cell types. Diagonal elements of the matrix, denote upper bounds of accuracy since it is the accuracy achieved on the training dataset. Our results demonstrate that the generic classification model we employed here can consistently identify structural features of follower and leader cells in both pure populations and co-cultures of cells. The specific classification model we employ here was chosen as a convenient, low computational cost option for a preliminary study. More advanced architectures like EfficientNet [115] may improve overall accuracy scores.

5.4 Conclusion

In this chapter, I reviewed the phenomenon of collective invasion via multi-cellular streaming that is observed in diverse populations of cancer cells throughout the body. Although this mode of migration, and the leader cell heterogeneity that gives rise to it, are well-known to be associated with metastasis and poor clinical outcome [84, 61], the mechanical interactions between the cells that gives rise to it remain elusive. Here, I outlined a computational pipeline – from trajectory extraction to force inference – for discovering a symbolic expressions for the pair-wise interactions between cells, and gave a simple demonstration for the case of a fluid-like epithelial monolayer. With additional data, a future exploratory study could investigate what cell-cell interactions are consistently learned across multiple experiments, and how those interactions depend on the cell properties that are included in the feature vectors of nodes in the graph.

There are other open questions about force inference graph networks that could be studied without experimental data though. For example, we know that the dynamics our model learns is strongly dependent on the time-scale (dt) that we resolve velocities and accelerations at. It is not obvious though whether varying dt leads to entirely new functional forms being predicted for the interactions between particles, or whether parameter values simply get re-scaled. A simple test one could perform is to generate synthetic particle trajectory data from numerical simulation in which one knows the true underlying interaction, as in Ref. [29]. Rather than using exact velocities and accelerations as input into the force inference model though, models would be trained on velocities and accelerations obtained from finite-difference calculations as in Section 5.2.2. By varying dt , one could directly observe how the true pair-wise interaction transforms as forces are inferred at longer and longer time-scales. This work would provide an incredibly important frame of reference when later choosing a time-scale to study the dynamics of cellular monolayers.

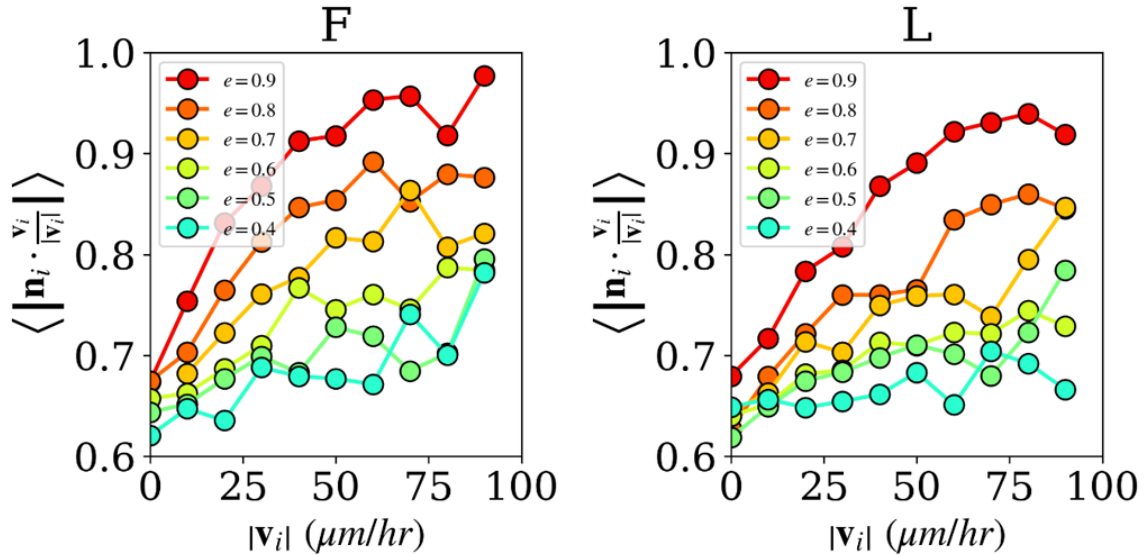


Figure 5.16: **Correlation between shape and dynamics.** The average orientational alignment between a cell's axis of elongation (\mathbf{n}_i) with its instantaneous velocity vector (\mathbf{v}_i) for follower (F) and leader (L) cells at different values of eccentricity (as defined in Fig. 5.8).

I also showed how the segmentation and tracking pieces of the pipeline can be used to extract vast amounts of single-cell shape and image data that can be used to study population statistics as well as train image classification neural networks. A preliminary analysis of this data showed that there are phenotypic heterogeneities between followers and leaders that is consistent across experiments spaced months apart. A straight-forward extension of this work would be to test d

Chapter 6

Conclusions

This dissertation explores the collective behavior of active matter systems through the lens of minimal models, where complex interactions between self-propelled agents are distilled into a few fundamental rules, allowing us to identify universal behaviors across a wide range of systems.

In Chapter 2, we investigated the phase transition in the Vicsek model, a fundamental agent-based model of flocking. We provided numerical evidence that both metric and topological flocks exhibit the same macroscopic phase behavior at the order-disorder transition. This result supports the hypothesis that the large-scale behavior of a system is independent of microscopic details and instead governed by key properties like dimensionality and symmetry.

In Chapter 3, we studied the effects of hierarchical reaction times on flocking dynamics. We introduced a model that incorporates time-delayed interactions between agents and demonstrated the emergence of a novel PT-symmetric phase can be attributed to the presence of microscopic non-reciprocal forces that self-organized in space to drive the spatial-temporal patterning we observe.

In Chapter 4, we examined the collective behavior of *Bos Taurus* sperm cells. Using machine learning techniques, we identified a density-dependent transition between

vortex and flocking states. We showed that the flocking state exhibits giant number fluctuations and transverse density correlation statistics consistent with Toner-Tu theory, and that the transition to the vortex state can be attributed to an intrinsic persistent turning behavior of the cells.

In Chapter 5, we developed a deep learning framework to infer the heterogeneous dynamics and morphologies of follower/leader cancer cells. We demonstrated that a graph neural network can be used to predict collective cell motion from pair-wise interactions and outlined a strategy to collect trajectory data from heterogeneous populations of cells and apply this method to identify dynamical and phenotypic differences.

These studies demonstrate the power of minimal models to capture essential features of flocking phenomena across different biological systems. By simplifying complex interactions, we can gain insights into the fundamental principles governing collective behavior and identify potential universality classes.

There are several avenues for future research. One direction is to further explore the role of non-reciprocal interactions in active matter systems. While Chapter 3 focused on time-delayed interactions, other forms of non-reciprocity, such as those arising from hydrodynamic interactions or substrate coupling, could be investigated. It would also be interesting to examine how different types of non-reciprocity influence the stability and dynamics of flocking phases.

Another promising area is to extend the deep learning framework developed in Chapter 5. The current model could be refined to incorporate more detailed cell features, such as cell shape and internal dynamics. This could lead to a more comprehensive understanding of cell-cell interactions and the emergence of collective behavior in cellular systems. Additionally, the framework could be applied to other biological systems, such as bacterial colonies or tissues, to investigate the role of heterogeneity in collective dynamics.

Appendix A

Hidden Non-Reciprocity In The Vicsek Model

In these notes, I show that the Vicsek model has an implicit non-reciprocity in the interactions between particles, which is not accounted for in Toner-Tu theory. The polar alignment interaction in the Vicsek model (Eq. 1.2) is written here explicitly as an alignment with the mean orientation of its neighboring particles,

$$\langle \mathbf{v}_j(t) \rangle_{j \in \mathcal{N}_i(t)} \equiv \frac{1}{|\mathcal{N}_i(t)|} \sum_{j \in \mathcal{N}_i(t)} \mathbf{v}_j(t) \quad (\text{A.1})$$

This many-body alignment interaction can be expressed as the sum of pair-wise, Newtonian-like forces by considering the case of a (binary) interaction between two particles where

$$\mathbf{v}_i^b(t + \Delta t) \equiv \frac{1}{2} [\mathbf{v}_i(t) + \mathbf{v}_j(t)]$$

If we define the ‘force’ exerted on particle i within a time-interval Δt as

$$\mathbf{f}_i(t) \equiv \frac{\Delta \mathbf{p}_i(t)}{\Delta t} = m \frac{\Delta \mathbf{v}_i}{\Delta t} = m \frac{\mathbf{v}_i(t + \Delta t) - \mathbf{v}_i(t)}{\Delta t},$$

then the force exerted by particle j on particle i in a binary collision is

$$\mathbf{f}_{ij}^b(t) = \frac{m}{2\Delta t}(\mathbf{v}_j^t - \mathbf{v}_i^t) \quad (\text{A.2})$$

which obeys Newton's third with $\mathbf{f}_{ij}^b = -\mathbf{f}_{ji}^b$.

Having defined the reciprocal force (Eq. A.2) exerted between two interacting Vicsek particles, the many-body alignment interaction (Eq. A.1) can be written in terms of these forces by a simple re-arrangement of terms

$$\langle \mathbf{v}_j(t) \rangle_{j \in \mathcal{N}_i(t)} = \frac{1}{|\mathcal{N}_i|} \sum_{j \in \mathcal{N}_i} [(\mathbf{v}_j - \mathbf{v}_i) + \mathbf{v}_i] \quad (\text{A.3})$$

$$\langle \mathbf{v}_j(t) \rangle_{j \in \mathcal{N}_i(t)} = \frac{1}{|\mathcal{N}_i|} \sum_{j \in \mathcal{N}_i} \mathbf{v}_i + \frac{1}{|\mathcal{N}_i|} \sum_{j \in \mathcal{N}_i} (\mathbf{v}_j - \mathbf{v}_i) \quad (\text{A.4})$$

$$\langle \mathbf{v}_j(t) \rangle_{j \in \mathcal{N}_i(t)} = \mathbf{v}_i + \frac{2\Delta t}{m|\mathcal{N}_i|} \sum_{j \in \mathcal{N}_i} \mathbf{f}_{ij}^b \quad (\text{A.5})$$

This can be more readily seen to resemble Newton's second law, $\mathbf{F} = m\mathbf{a} = m\frac{\Delta v}{\Delta t}$, by defining the total force exerted by all neighboring particles on particle i within the time interval Δt as

$$\mathbf{F}_i(t) \equiv m \frac{\langle \mathbf{v}_j(t) \rangle_{j \in \mathcal{N}_i(t)} - \mathbf{v}_i(t)}{\Delta t} \quad (\text{A.6})$$

such that

$$\mathbf{F}_i(t) = \frac{2}{|\mathcal{N}_i|} \sum_{j \in \mathcal{N}_i} \mathbf{f}_{ij}^b \quad (\text{A.7})$$

This expression provides a completely equivalent description of the particle dynamics as Eq. A.1, but is written explicitly in terms of binary reciprocal interactions \mathbf{f}_{ij}^b and a potentially non-reciprocal weighting $|\mathcal{N}_i|^{-1}$ of those forces.

While the binary collision force (Eq. A.2) obeys Newton's third law - with $\mathbf{f}_{ij}^b + \mathbf{f}_{ji}^b = 0$ - when the many-body weighting $|\mathcal{N}_i|^{-1}$ in Eq. A.7 is taken into account, the Vicsek

model allows this relationship to be violated, and the non-reciprocity of an interaction can be defined as

$$\psi_{ij} \equiv \frac{2}{|\mathcal{N}_i|} \mathbf{f}_{ij}^b + \frac{2}{|\mathcal{N}_j|} \mathbf{f}_{ji}^b \quad (\text{A.8})$$

such that $\psi_{ij} = 0$ when $|\mathcal{N}_i| = |\mathcal{N}_j|$. Written explicitly in terms of the velocities of particles i and j , this non-reciprocity vector takes the form

$$\psi_{ij} = \left(\frac{1}{|\mathcal{N}_i|} - \frac{1}{|\mathcal{N}_j|} \right) (\mathbf{v}_j^t - \mathbf{v}_i^t) \quad (\text{A.9})$$

for $m, \Delta t = 1$.

Appendix B

Coarse-Graining The Vicsek Model

In the previous section I showed that non-reciprocal forces in the Vicsek model arise from unequal numbers of interacting neighbors, and that the magnitude of the non-reciprocity is directly proportional to the difference in the inverse neighbor-number

$$u_i = |\mathcal{N}_i|^{-1} \quad (\text{B.1})$$

Here I calculate how gradients in u_i couple to particle velocities and coarse-grain into macroscopic interactions. First I consider the term $\sum_j \mu_{ij} \mathbf{v}_i$, and write

$$\mu_{ij} = u_i - u_j \quad (\text{B.2})$$

A particle i sitting at the origin of the 2D square lattice shown in Fig. ?? then experiences the total interaction

$$-\sum_j \mu_{ij} = \left[(u_{\epsilon,0} - u_{0,0}) + (u_{-\epsilon,0} - u_{0,0}) \right] + \left[(u_{0,\epsilon} - u_{0,0}) + (u_{0,-\epsilon} - u_{0,0}) \right] \quad (\text{B.3})$$

where the minus sign on the l.h.s. is introduced to write the expression as deviations from particle i located at $(x, y) = (0, 0)$. Further re-arranging the terms on the r.h.s.

as

$$-\sum_j \mu_{ij} = \left[(u_{\epsilon,0} - u_{0,0}) - (u_{0,0} - u_{-\epsilon,0}) \right] + \left[(u_{0,\epsilon} - u_{0,0}) - (u_{0,0} - u_{0,-\epsilon}) \right] \quad (\text{B.4})$$

allows the quantities in parentheses to be re-written as forward finite differences by taking

$$\lim_{\epsilon \rightarrow 0} \frac{-\sum_j \mu_{ij}}{\epsilon} = \left[\partial_x^\dagger u_{0,0} - \partial_x^\dagger u_{-\epsilon,0} \right] + \left[\partial_y^\dagger u_{0,0} - \partial_y^\dagger u_{0,-\epsilon} \right]$$

Applying the forward finite difference operator again, we obtain the final result

$$\lim_{\epsilon \rightarrow 0} \frac{-\sum_j \mu_{ij}}{\epsilon^2} = \partial_x^{\dagger 2} u_{-\epsilon,0} + \partial_y^{\dagger 2} u_{0,-\epsilon} \quad (\text{B.5})$$

Summing this microscopic interaction over all particles in the system, we obtain the coarse-grained hydrodynamic interaction

$$\sum_{i=1}^N \left[\lim_{\epsilon \rightarrow 0} \frac{\sum_j \mu_{ij}}{\epsilon^2} \mathbf{v}_i \right] \delta(\mathbf{r} - \mathbf{r}_i(t)) = -\nabla^2 \frac{1}{\mathcal{N}(\mathbf{r}, t)} \mathbf{m}(\mathbf{r}) \quad (\text{B.6})$$

which is accurate to $\mathcal{O}(\epsilon)$.

This approximation is actually accurate to $\mathcal{O}(\epsilon^2)$ though, which can be shown by instead using the central difference operator defined by

$$\partial_x^\dagger u(x, y) = \frac{u(x + \epsilon, y) - u(x - \epsilon, y)}{2\epsilon} \quad (\text{B.7})$$

$$\partial_x^{\dagger 2} u(x, y) = \frac{u(x + \epsilon, y) - 2u(x, y) + u(x - \epsilon, y)}{\epsilon^2} \quad (\text{B.8})$$

Applying Eq. B.8 to both bracketed terms in Eq. B.4, leads to the exact same result Eq. B.6 as obtained with the forward difference operator.

We can gain a physical intuition for Eq. B.6 by recognizing it as a diffusive term

for the quantity $\mathcal{N}(\mathbf{r})^{-1}$ that senses the net flux of $\mathcal{N}(\mathbf{r})^{-1}$ through a boundary via $\int_V dV \nabla \cdot (\nabla \frac{1}{\mathcal{N}}) = \int_{\partial V} d\mathbf{S} \cdot (\nabla \frac{1}{\mathcal{N}})$. Loosely speaking, the term measures the local non-reciprocity - proportional to $\nabla \frac{1}{\mathcal{N}}$ - and then compares it with the non-reciprocity of the surrounding region. The response of the system to such gradients in non-reciprocity is determined by the coupling constant associated with it for a specific system of particles.

Repeating the above procedure, here I coarse-grain the ‘true’ non-reciprocal interaction $\psi_i = \sum_j \psi_{ij} = \sum_j \mu_{ij}(\mathbf{v}_j - \mathbf{v}_i)$ into an approximate continuum interaction. Once again using the definition Eq. B.1 for the inverse neighbor number, we have

$$\sum_j \mu_{ij} \mathbf{v}_{ij} = - \sum_j (u_j - u_i)(\mathbf{v}_j - \mathbf{v}_i) \quad (\text{B.9})$$

Coarse-graining this interaction is less straight-forward than $\sum_j \mu_{ij} \mathbf{v}_i$ since the scalar and vector quantity at each lattice point is varying. But, we may proceed in the same manner as above by explicitly writing the interaction for a lattice system as

$$\begin{aligned} - \sum_j \mu_{ij} \mathbf{v}_{ij} = & \left[(u_{\epsilon,0} - u_{0,0})(\mathbf{v}_{\epsilon,0} - \mathbf{v}_{0,0}) + (u_{-\epsilon,0} - u_{0,0})(\mathbf{v}_{-\epsilon,0} - \mathbf{v}_{0,0}) \right] \\ & + \left[(u_{0,\epsilon} - u_{0,0})(\mathbf{v}_{0,\epsilon} - \mathbf{v}_{0,0}) + (u_{0,-\epsilon} - u_{0,0})(\mathbf{v}_{0,-\epsilon} - \mathbf{v}_{0,0}) \right] \end{aligned} \quad (\text{B.10})$$

The second-order central difference operator (Eq. B.8) cannot be as easily applied here as it was in Eq. B.4 due to the mixed u and \mathbf{v} terms.

Considering first the forward-difference operator, the above expression simplifies to

$$\lim_{\epsilon \rightarrow 0} \frac{- \sum_j \mu_{ij} \mathbf{v}_{ij}}{\epsilon^2} = \left[(\partial_x^\dagger u_{0,0})(\partial_x^\dagger \mathbf{v}_{0,0}) + (\partial_x^\dagger u_{-\epsilon,0})(\partial_x^\dagger \mathbf{v}_{-\epsilon,0}) \right] + \left[(\partial_y^\dagger u_{0,0})(\partial_y^\dagger \mathbf{v}_{0,0}) + (\partial_y^\dagger u_{0,-\epsilon})(\partial_y^\dagger \mathbf{v}_{0,-\epsilon}) \right]$$

Note that after applying ∂_i^\dagger to both u and \mathbf{v} , we have run out of opposite signed

terms with which to take further differences, so we will once again obtain a term of $\mathcal{O}(\nabla^2)$. Seeking then to simplify the above expression in terms of the differences already present, we can regroup terms according to

$$\lim_{\epsilon \rightarrow 0} \frac{-\sum_j \mu_{ij} \mathbf{v}_{ij}}{\epsilon^2} = \left[(\partial_x^\dagger u_{0,0}) \partial_x^\dagger + (\partial_y^\dagger u_{0,0}) \partial_y^\dagger \right] \mathbf{v}_{0,0} + \left[(\partial_x^\dagger u_{-\epsilon,0}) (\partial_x^\dagger \mathbf{v}_{-\epsilon,0}) + (\partial_y^\dagger u_{0,-\epsilon}) (\partial_y^\dagger \mathbf{v}_{0,-\epsilon}) \right] \quad (\text{B.11})$$

from which we see that the first bracketed term has the continuum form $(\nabla u \cdot \nabla) \mathbf{m}$. The second bracketed term can be worked into the same form by noting that $\partial_x^\dagger f_{-\epsilon,0} = \partial_x^\dagger f_{0,0}$. Making this substitution for all terms in the second brackets, we obtain the continuum approximation

$$\sum_{i=1}^N \left[\lim_{\epsilon \rightarrow 0} \frac{\sum_j \mu_{ij} \mathbf{v}_{ij}}{\epsilon^2} \right] \delta(\mathbf{r} - \mathbf{r}_i(t)) \rightarrow - \left(\nabla \frac{1}{\mathcal{N}} \cdot \nabla \right) \mathbf{m} \quad (\text{B.12})$$

This completes the coarse-graining of the microscopic neighbor-number-difference terms into hydrodynamic interactions.

Appendix C

Non-Reciprocal Fluctuation

Renormalization

Here I apply the fluctuation renormalization technique outlined by Martin & Tailleur in Ref. [71] to determine the effect of neighbor-number induced non-reciprocity on the non-linear hydrodynamics of a one-dimensional metric active polar fluid. A large amount of this section is lifted directly from Ref. [71], since our work follows an identical analytical path, but with a few extra steps scattered throughout.

C.1 Introduction

Let $\rho(x, t)$ and $m(x, t)$ be the density and orientation fields of a 1D active Ising model with the hydrodynamics

$$\partial_t \rho = D \partial_x^2 \rho - v \partial_x m \tag{C.1}$$

$$\partial_t m = D \partial_x^2 m - v \partial_x \rho - F[\rho, m] - D_\rho \left(\partial_x^2 \frac{1}{\mathcal{N}} \right) m - g \left(\partial_x \frac{1}{\mathcal{N}} \partial_x \right) m + \sqrt{2\sigma\rho} \eta. \tag{C.2}$$

Here $F \equiv \delta U / \delta m$ is the gradient of the Landau potential

$$U[\rho(x, t), m(x, t)] = \int_{-\infty}^{\infty} dx \left[\frac{\alpha}{2} m^2 + \frac{\gamma}{4} \frac{m^4}{\rho^2} \right]. \quad (\text{C.3})$$

The ρ dependence of the quartic term in Eq. C.3 is a consequence of assuming metric alignment. Note that $\alpha > 0$ corresponds to the ‘high-temperature’ disordered phase.

C.2 Perturbation expansion of equations of motion

Let ρ_0 and m_0 be the homogeneous solution to Eqs. C.1-C.2 in the absence of noise ($\sigma = 0$), where

$$m_0 = \rho_0 \sqrt{\frac{-\alpha}{\gamma}}, \quad (\text{C.4})$$

and define deviations from these deterministic, mean-field solutions to be given by

$$\Delta\rho(x, t) \equiv \rho(x, t) - \rho_0 = \sigma^{\frac{1}{2}} \delta\rho_1 + \sigma \delta\rho_2 + \dots \quad (\text{C.5})$$

$$\Delta m(x, t) \equiv m(x, t) - m_0 = \sigma^{\frac{1}{2}} \delta m_1 + \sigma \delta m_2 + \dots \quad (\text{C.6})$$

With this perturbation scheme, the free energy gradient, $F(\rho, m)$, in Eq. C.2 can be expanded about (ρ_0, m_0) as

$$\begin{aligned} F(\rho, m) = & F(\rho_0, m_0) + \sigma^{\frac{1}{2}} \frac{\partial F}{\partial \rho} \delta\rho_1 + \sigma^{\frac{1}{2}} \frac{\partial F}{\partial m} \delta m_1 + \sigma \frac{\partial F}{\partial \rho} \delta\rho_2 + \sigma \frac{\partial F}{\partial m} \delta m_2 \\ & + \sigma \frac{\partial^2 F}{\partial \rho^2} \frac{\delta\rho_1^2}{2} + \sigma \frac{\partial^2 F}{\partial m^2} \frac{\delta m_1^2}{2} + \sigma \frac{\partial^2 F}{\partial \rho \partial m} \delta\rho_1 \delta m_1 + \mathcal{O}(\sigma^{\frac{3}{2}}), \end{aligned} \quad (\text{C.7})$$

where the derivatives in Eq. C.7 are evaluated at (ρ_0, m_0) . Inserting Eqs. C.5-C.6 into Eqs. C.1-C.2 one obtains two sets of equations of motion for the fluctuations at

the scale of $\sigma^{1/2}$ and σ^1 , given by

$$\partial_t \delta \rho_1 = D \partial_x^2 \delta \rho_1 - v \partial_x \delta m_1 \quad (\text{C.8})$$

$$\partial_t \delta m_1 = D \partial_x^2 \delta m_1 - v \partial_x \delta \rho_1 - \frac{\partial F}{\partial \rho} \delta \rho_1 - \frac{\partial F}{\partial m} \delta m_1 + \sqrt{2\rho_0} \eta + C_1. \quad (\text{C.9})$$

and

$$\partial_t \delta \rho_2 = D \partial_x^2 \delta \rho_2 - v \partial_x \delta m_2 \quad (\text{C.10})$$

$$\begin{aligned} \partial_t \delta m_2 = D \partial_x^2 \delta m_2 - v \partial_x \delta \rho_2 - \frac{\partial F}{\partial \rho} \delta \rho_2 - \frac{\partial F}{\partial m} \delta m_2 \\ - \frac{\partial^2 F}{\partial \rho^2} \frac{\delta \rho_1^2}{2} - \frac{\partial^2 F}{\partial m^2} \frac{\delta m_1^2}{2} - \frac{\partial^2 F}{\partial \rho \partial m} \delta \rho_1 \delta m_1 + \frac{\delta \rho_1}{\sqrt{2\rho_0}} \eta + C_2. \end{aligned} \quad (\text{C.11})$$

The C_1 and C_2 terms denote the non-reciprocal hydrodynamic corrections to Martin & Tailleur's theory, which will be computed later.

C.3 Renormalized field dynamics

Averaging the dynamics of the fluctuations fields over different noise realizations of Eqs. C.8-C.9 gives the first-order equations of motion

$$\partial_t \langle \delta \rho_1 \rangle = D \partial_x^2 \langle \delta \rho_1 \rangle - v \partial_x \langle \delta m_1 \rangle \quad (\text{C.12})$$

$$\partial_t \langle \delta m_1 \rangle = D \partial_x^2 \langle \delta m_1 \rangle - v \partial_x \langle \delta \rho_1 \rangle - \frac{\partial F}{\partial \rho} \langle \delta \rho_1 \rangle - \frac{\partial F}{\partial m} \langle \delta m_1 \rangle + \langle C_1 \rangle, \quad (\text{C.13})$$

and averaging Eqs. C.10-C.11 gives the second-order equations of motion

$$\partial_t \langle \delta \rho_2 \rangle = D \partial_x^2 \langle \delta \rho_2 \rangle - v \partial_x \langle \delta m_2 \rangle \quad (\text{C.14})$$

$$\begin{aligned} \partial_t \langle \delta m_2 \rangle = & D \partial_x^2 \langle \delta m_2 \rangle - v \partial_x \langle \delta \rho_2 \rangle - \frac{\partial F}{\partial \rho} \langle \delta \rho_2 \rangle - \frac{\partial F}{\partial m} \langle \delta m_2 \rangle \\ & - \frac{\partial^2 F}{\partial \rho^2} \frac{\langle \delta \rho_1^2 \rangle}{2} - \frac{\partial^2 F}{\partial m^2} \frac{\langle \delta m_1^2 \rangle}{2} - \frac{\partial^2 F}{\partial \rho \partial m} \langle \delta \rho_1 \delta m_1 \rangle + \langle C_2 \rangle. \end{aligned} \quad (\text{C.15})$$

Now if we define

$$\tilde{\rho}(x, t) \equiv \langle \rho \rangle \approx \rho_0 + \sigma^{\frac{1}{2}} \langle \delta \rho_1 \rangle + \sigma \langle \delta \rho_2 \rangle \quad (\text{C.16})$$

$$\tilde{m}(x, t) \equiv \langle m \rangle \approx m_0 + \sigma^{\frac{1}{2}} \langle \delta m_1 \rangle + \sigma \langle \delta m_2 \rangle, \quad (\text{C.17})$$

then the summing of Eqs. C.12 and C.14, as well as Eqs. C.13 and C.15, yields the evolution of $\tilde{\rho}$ and \tilde{m} up to order σ ,

$$\partial_t \tilde{\rho} = D \partial_x^2 \tilde{\rho} - v \partial_x \tilde{m} \quad (\text{C.18})$$

$$\begin{aligned} \partial_t \tilde{m} = & D \partial_x^2 \tilde{m} - v \partial_x \tilde{\rho} - \sigma^{\frac{1}{2}} \frac{\partial F}{\partial \rho} \langle \delta \rho_1 \rangle - \sigma^{\frac{1}{2}} \frac{\partial F}{\partial m} \langle \delta m_1 \rangle - \sigma \frac{\partial F}{\partial \rho} \langle \delta \rho_2 \rangle - \sigma \frac{\partial F}{\partial m} \langle \delta m_2 \rangle \\ & - \sigma \frac{\partial^2 F}{\partial \rho^2} \frac{\langle \delta \rho_1^2 \rangle}{2} - \sigma \frac{\partial^2 F}{\partial m^2} \frac{\langle \delta m_1^2 \rangle}{2} - \sigma \frac{\partial^2 F}{\partial \rho \partial m} \langle \delta \rho_1 \delta m_1 \rangle + \sigma^{\frac{1}{2}} \langle C_1 \rangle + \langle C_2 \rangle. \end{aligned} \quad (\text{C.19})$$

Eqs. C.18-C.19 constitute the renormalized hydrodynamics for the fields $\tilde{\rho}$ and \tilde{m} .

In Eqs. C.18-C.19, averages of individual fluctuation fields evaluate to zero since the white noise field (η) in Eq C.2 that produces them is equally likely to give rise to a positive or negative fluctuation. That is,

$$\langle \delta \rho_k \rangle = \langle \delta m_k \rangle = 0. \quad (\text{C.20})$$

The non-vanishing correlations between the fluctuations in Eqs. C.18-C.19 though

make it so that Eqs. C.16-C.17 do *not* reduce to $\tilde{\rho} = \rho_0$ and $\tilde{m} = m_0$. That is, the correlators renormalize the noisy, fluctuating dynamics of Eqs. C.1-C.2 into a set of averaged equations of motion with a new homogeneous steady-state. A convenient way to express this renormalization is through a modified free energy for the system, which I construct in the following section.

C.4 Renormalized free energy

The free energy terms already appearing in Eqs. C.18-C.19 were obtained from

$$\langle F[\rho(x, t), m(x, t)] \rangle = \left\langle F \left[\rho_0 + \sum_{k=1}^{\infty} \sigma^{k/2} \delta \rho_k(x, t), m_0 + \sum_{k=1}^{\infty} \sigma^{k/2} \delta m_k(x, t) \right] \right\rangle. \quad (\text{C.21})$$

In this expression, m_0 is assumed to vary on time-scales much longer than δm_k , and we say that the δm_k are fluctuations on top of an effectively fixed energy minimum, $F(\rho_0, m_0)$. We wish now though to re-express F solely in terms of the renormalized fields, $\tilde{\rho}$ and \tilde{m} . To do so, we write

$$F[\tilde{\rho}(x, t), \tilde{m}(x, t)] = F \left[\rho_0 + \sum_{k=1}^{\infty} \sigma^{k/2} \langle \delta \rho_k(x, t) \rangle, m_0 + \sum_{k=1}^{\infty} \sigma^{k/2} \langle \delta m_k(x, t) \rangle \right]. \quad (\text{C.22})$$

Expanding this expression to order $\mathcal{O}(\sigma)$ gives

$$\begin{aligned} F[\tilde{\rho}, \tilde{m}] &= F(\rho_0, m_0) + \sigma^{1/2} \frac{\partial F}{\partial \rho} \langle \delta \rho_1 \rangle + \sigma^{1/2} \frac{\partial F}{\partial m} \langle \delta m_1 \rangle + \sigma \frac{\partial F}{\partial \rho} \langle \delta \rho_2 \rangle + \sigma \frac{\partial F}{\partial m} \langle \delta m_2 \rangle \\ &\quad + \sigma \frac{\partial^2 F}{\partial \rho^2} \frac{\langle \delta \rho_1 \rangle^2}{2} + \sigma \frac{\partial^2 F}{\partial m^2} \frac{\langle \delta m_1 \rangle^2}{2} + \sigma \frac{\partial^2 F}{\partial \rho \partial m} \langle \delta \rho_1 \rangle \langle \delta m_1 \rangle + \mathcal{O}(\sigma^{3/2}), \end{aligned} \quad (\text{C.23})$$

where the derivatives of F here are evaluated at $(\tilde{\rho}, \tilde{m})$; in Eq. C.19, they are evaluated at (ρ_0, m_0) . Noting that the constant term, $F(\rho_0, m_0)$, can be freely added to Eq. C.19 since it defines the solution to the mean-field equation $\partial_t m = F(\rho, m) = 0$, we can

insert Eq. C.23 into Eq. C.19 to obtain

$$\begin{aligned} \partial_t \tilde{m} = & -F(\tilde{\rho}, \tilde{m}) - \sigma \frac{\partial^2 F}{\partial \rho^2} \left(\frac{\langle \delta \rho_1^2 \rangle - \langle \delta \rho_1 \rangle^2}{2} \right) - \sigma \frac{\partial^2 F}{\partial m^2} \left(\frac{\langle \delta m_1^2 \rangle - \langle \delta m_1 \rangle^2}{2} \right) \\ & - \sigma \frac{\partial^2 F}{\partial \rho \partial m} (\langle \delta \rho_1 \delta m_1 \rangle - \langle \delta \rho_1 \rangle \langle \delta m_1 \rangle) + D \partial_x^2 \tilde{m} - v \partial_x \tilde{\rho} + \sigma^{\frac{1}{2}} \langle C_1 \rangle + \langle C_2 \rangle. \end{aligned} \quad (\text{C.24})$$

In writing Eq. C.24, we implicitly re-establish the dependency of ρ_0 and m_0 on x and t and (following Martin & Tailleur) have taken

$$\rho_0 \rightarrow \tilde{\rho}(x, t) \quad \text{and} \quad m_0 \rightarrow \tilde{m}(x, t). \quad (\text{C.25})$$

This is mathematically valid since we are restating Eqs. C.16-C.17 while using Eq. C.20. From the renormalized dynamics of Eq. C.24, one can compute new steady-state values of ρ_0 and m_0 though, and iteratively apply this perturbative renormalization technique.

Finally, I note that from Eq. C.3 on has

$$F(\rho, m) = \alpha m + \gamma \frac{m^3}{\rho^2}, \quad (\text{C.26})$$

or equivalently

$$F(\tilde{\rho}, \tilde{m}) = \alpha \tilde{m} + \gamma \frac{\tilde{m}^3}{\tilde{\rho}^2}. \quad (\text{C.27})$$

The derivatives of F appearing in Eq. C.24 are then given by

$$\frac{\partial^2 F}{\partial \rho^2} = 6\gamma \frac{\tilde{m}^3}{\tilde{\rho}^4} \quad (\text{C.28})$$

$$\frac{\partial^2 F}{\partial m^2} = 6\gamma \frac{\tilde{m}}{\tilde{\rho}^2} \quad (\text{C.29})$$

$$\frac{\partial^2 F}{\partial \rho \partial m} = -6\gamma \frac{\tilde{m}^2}{\tilde{\rho}^3}. \quad (\text{C.30})$$

Inserting Eqs. C.27-C.30 into Eq. C.24 and enforcing Eq. C.20 then yields

$$\begin{aligned} \partial_t \tilde{m} = & D \partial_x^2 \tilde{m} - v \partial_x \tilde{\rho} - \alpha \tilde{m} - \gamma \frac{\tilde{m}^3}{\tilde{\rho}^2} \\ & - 3\sigma\gamma \frac{\tilde{m}^3}{\tilde{\rho}^4} \langle \delta \rho_1^2 \rangle - 3\sigma\gamma \frac{\tilde{m}}{\tilde{\rho}^2} \langle \delta m_1^2 \rangle + 6\sigma\gamma \frac{\tilde{m}^2}{\tilde{\rho}^3} \langle \delta \rho_1 \delta m_1 \rangle + \sigma^{\frac{1}{2}} \langle C_1 \rangle + \langle C_2 \rangle . \end{aligned} \quad (\text{C.31})$$

Note that setting $\sigma = 0$ here restores the mean-field dynamics of Eq. C.2. With $\sigma \neq 0$ though, the non-linear terms on the second line of Eq. C.31 lead to fluctuation-induced renormalized dynamics.

C.5 Fluctuation expansion of non-reciprocal hydrodynamic corrections

Here I compute (in tedious detail) the non-reciprocal correction terms appearing in Eq. C.31,

$$C_{1,2} \equiv -D_\rho \left(\partial_x^2 \frac{1}{\mathcal{N}} \right) m - g \left(\partial_x \frac{1}{\mathcal{N}} \partial_x \right) m . \quad (\text{C.32})$$

With Eq. ??, we can compute the derivatives appearing in Eq. C.32 to be

$$\mu \frac{\partial}{\partial x} \frac{1}{\mathcal{N}} = \frac{-Q}{\rho^{Q+1}} (\partial_x \rho) \quad (\text{C.33})$$

$$\mu \frac{\partial^2}{\partial x^2} \frac{1}{\mathcal{N}} = \frac{Q}{\rho^{Q+2}} \left[(Q+1) (\partial_x \rho)^2 - \rho (\partial_x^2 \rho) \right] . \quad (\text{C.34})$$

The correctness of these expressions has been double-checked using *Mathematica*. Now we expand these derivatives in terms of density field fluctuations by inserting

Eq. C.5 into Eqs. C.33-C.34 to obtain

$$\mu \frac{\partial}{\partial x} \frac{1}{\mathcal{N}} \approx -Q \left(\rho_0 + \sigma^{\frac{1}{2}} \delta \rho_1 + \sigma \delta \rho_2 \right)^{-Q-1} \partial_x \left(\sigma^{\frac{1}{2}} \delta \rho_1 + \sigma \delta \rho_2 \right) \quad (\text{C.35})$$

$$\begin{aligned} \mu \frac{\partial^2}{\partial x^2} \frac{1}{\mathcal{N}} \approx Q \left(\rho_0 + \sigma^{\frac{1}{2}} \delta \rho_1 + \sigma \delta \rho_2 \right)^{-Q-2} & \left[\sigma(Q+1)(\partial_x \delta \rho_1)^2 - \sigma^{\frac{1}{2}} \rho_0 \partial_x^2 \delta \rho_1 \right. \\ & \left. - \sigma \left(\rho_0 \partial_x^2 \delta \rho_2 + \delta \rho_1 \partial_x^2 \delta \rho_1 \right) \right], \end{aligned} \quad (\text{C.36})$$

where in Eq. C.36 I have used the intermediate result

$$(\partial_x \rho)^2 = \left(\partial_x \left(\sigma^{\frac{1}{2}} \delta \rho_1 + \sigma \delta \rho_2 \right) \right)^2 \quad (\text{C.37})$$

$$= \sigma (\partial_x \delta \rho_1)^2 + \mathcal{O}(\sigma^{\frac{3}{2}}) \quad (\text{C.38})$$

and

$$\rho (\partial_x^2 \rho) = \left(\rho_0 + \sigma^{\frac{1}{2}} \delta \rho_1 + \sigma \delta \rho_2 \right) \left(\partial_x^2 \left(\sigma^{\frac{1}{2}} \delta \rho_1 + \sigma \delta \rho_2 \right) \right) \quad (\text{C.39})$$

$$= \sigma^{\frac{1}{2}} \rho_0 \partial_x^2 \delta \rho_1 + \sigma \left(\rho_0 \partial_x^2 \delta \rho_2 + \delta \rho_1 \partial_x^2 \delta \rho_1 \right) + \mathcal{O}(\sigma^{\frac{3}{2}}). \quad (\text{C.40})$$

The correctness of these expressions has also been double-checked using *Mathematica*. I handle the prefactors in Eqs. C.35-C.36 (with Q appearing in the exponent) by rewriting them as

$$\left(\rho_0 + \sigma^{\frac{1}{2}} \delta \rho_1 + \sigma \delta \rho_2 \right)^{-Q-1} = \rho_0^{-Q-1} \left(1 + \frac{\sigma^{\frac{1}{2}} \delta \rho_1 + \sigma \delta \rho_2}{\rho_0} \right)^{-Q-1} \quad (\text{C.41})$$

$$\left(\rho_0 + \sigma^{\frac{1}{2}} \delta \rho_1 + \sigma \delta \rho_2 \right)^{-Q-2} = \rho_0^{-Q-2} \left(1 + \frac{\sigma^{\frac{1}{2}} \delta \rho_1 + \sigma \delta \rho_2}{\rho_0} \right)^{-Q-2}, \quad (\text{C.42})$$

and then making the *binomial approximation*, $(1+x)^\alpha \approx 1 + \alpha x$ for $|\alpha x| \ll 1$,

$$\left(\rho_0 + \sigma^{\frac{1}{2}}\delta\rho_1 + \sigma\delta\rho_2\right)^{-Q-1} \approx \rho_0^{-Q-1} \left[1 - (Q+1)\frac{\sigma^{\frac{1}{2}}\delta\rho_1 + \sigma\delta\rho_2}{\rho_0}\right] \quad (\text{C.43})$$

$$\left(\rho_0 + \sigma^{\frac{1}{2}}\delta\rho_1 + \sigma\delta\rho_2\right)^{-Q-2} \approx \rho_0^{-Q-2} \left[1 - (Q+2)\frac{\sigma^{\frac{1}{2}}\delta\rho_1 + \sigma\delta\rho_2}{\rho_0}\right]. \quad (\text{C.44})$$

Inserting Eqs. C.43-C.44 back into Eqs. C.35-C.36 then yields

$$\mu \frac{\partial}{\partial x} \frac{1}{\mathcal{N}} \approx \frac{-Q}{\rho_0^{Q+1}} \left[1 - (Q+1)\frac{\sigma^{\frac{1}{2}}\delta\rho_1 + \sigma\delta\rho_2}{\rho_0}\right] \partial_x \left(\sigma^{\frac{1}{2}}\delta\rho_1 + \sigma\delta\rho_2\right) \quad (\text{C.45})$$

$$\begin{aligned} \mu \frac{\partial^2}{\partial x^2} \frac{1}{\mathcal{N}} \approx \frac{Q}{\rho_0^{Q+2}} \left[1 - (Q+2)\frac{\sigma^{\frac{1}{2}}\delta\rho_1 + \sigma\delta\rho_2}{\rho_0}\right] & \left[\sigma(Q+1)(\partial_x\delta\rho_1)^2 - \sigma^{\frac{1}{2}}\rho_0\partial_x^2\delta\rho_1 \right. \\ & \left. - \sigma(\rho_0\partial_x^2\delta\rho_2 + \delta\rho_1\partial_x^2\delta\rho_1) \right]. \end{aligned} \quad (\text{C.46})$$

We now discard from Eqs. C.45-C.46 all terms greater than $\mathcal{O}(\sigma)$ to obtain

$$\mu \frac{\partial}{\partial x} \frac{1}{\mathcal{N}} \approx \frac{-Q}{\rho_0^{Q+1}} \left[\sigma^{\frac{1}{2}}\partial_x\delta\rho_1 + \sigma \left(\partial_x\delta\rho_2 - \frac{Q+1}{\rho_0}\delta\rho_1\partial_x\delta\rho_1 \right) \right] \quad (\text{C.47})$$

$$\mu \frac{\partial^2}{\partial x^2} \frac{1}{\mathcal{N}} \approx \frac{Q}{\rho_0^{Q+2}} \left[-\sigma^{\frac{1}{2}}\rho_0\partial_x^2\delta\rho_1 + \sigma \left((Q+1)(\partial_x\delta\rho_1)^2 - \rho_0\partial_x^2\delta\rho_2 + (Q+1)\delta\rho_1\partial_x^2\delta\rho_1 \right) \right]. \quad (\text{C.48})$$

With the gradients of the inverse neighbor-number field now fully calculated, we can insert Eqs. C.47-C.48 into the original correction term, Eq. C.32, to obtain

$$C_1 \equiv -\frac{D_\rho}{\mu} \left[\frac{-Q\sigma^{1/2}}{\rho_0^{Q+2}}\rho_0\partial_x^2\delta\rho_1 \right] m_0 - \frac{g}{\mu} \left[\frac{-Q\sigma^{1/2}}{\rho_0^{Q+1}}\partial_x\delta\rho_1 \right] (\sigma^{1/2}\partial_x\delta m_1 + \sigma\partial_x\delta m_2) \quad (\text{C.49})$$

The non-reciprocal g term vanishes from the first-order correction since the lowest order contribution from that term (in a state where m_0 is homogeneous) is $\mathcal{O}(\sigma^1)$.

Now, for convenience I define a modified diffusion coefficient

$$D_Q \equiv \frac{D_\rho Q}{\mu \rho_0^{Q+1}} \quad (\text{C.50})$$

that is indexed by Q , such that

$$C_1 = \sigma^{1/2} m_0 D_Q \partial_x^2 \delta \rho_1 + \mathcal{O}(\sigma). \quad (\text{C.51})$$

The correction Eq. C.51 will be the new term that enters Martin & Tailleur's calculation of the correlators that renormalize the free energy. Lastly, I note here that although the g term in Eq. C.49 does not enter into the calculation of the correlators, it is present in the non-linear dynamics. That is, the correction term to order $\mathcal{O}(\sigma)$ is given by

$$C_2 = -\sigma D_Q \left[\frac{Q+1}{\rho_0} (\partial_x \delta \rho_1)^2 - \partial_x^2 \delta \rho_2 + \frac{Q+1}{\rho_0} \delta \rho_1 \partial_x^2 \delta \rho_1 \right] m_0 \quad (\text{C.52})$$

$$+ \sigma g_Q (\partial_x \delta \rho_1 \partial_x \delta m_1) + \mathcal{O}(\sigma^{3/2}).$$

where I have defined the modified advection strength

$$g_Q \equiv \frac{gQ}{\mu \rho_0^{Q+1}} \quad (\text{C.53})$$

in analogy with Eq. C.50.

C.6 Non-reciprocal corrections to renormalized hydrodynamics

Having finally obtained Eqs. C.51- C.52, we can return to the renormalized hydrodynamics of Eq. C.31 and write

$$\sigma^{\frac{1}{2}}\langle C_1 \rangle = \sigma m_0 D_Q \partial_x^2 \langle \delta \rho_1 \rangle \quad (\text{C.54})$$

$$\langle C_2 \rangle = -\sigma D_Q \left[\frac{Q+1}{\rho_0} (\langle (\partial_x \delta \rho_1)^2 \rangle + \langle \delta \rho_1 \partial_x^2 \delta \rho_1 \rangle) - \partial_x^2 \langle \delta \rho_2 \rangle \right] m_0 + \sigma g_Q \langle \partial_x \delta \rho_1 \partial_x \delta m_1 \rangle. \quad (\text{C.55})$$

Inserting these results back into Eq. C.31 and taking $m_0 \rightarrow \tilde{m}$ in Eq. C.55 (as previously described in Eq. C.25), we obtain

$$\begin{aligned} \partial_t \tilde{m} = & -\alpha \tilde{m} - \gamma \frac{\tilde{m}^3}{\tilde{\rho}^2} + D \partial_x^2 \tilde{m} - v \partial_x \tilde{\rho} \\ & - \sigma \left[3\gamma \frac{\tilde{m}^3}{\tilde{\rho}^4} \langle \delta \rho_1^2 \rangle - 3\gamma \frac{\tilde{m}}{\tilde{\rho}^2} \langle \delta m_1^2 \rangle + 6\gamma \frac{\tilde{m}^2}{\tilde{\rho}^3} \langle \delta \rho_1 \delta m_1 \rangle \right. \\ & \left. - D_Q \frac{Q+1}{\rho_0} [\langle \partial_x \delta \rho_1 \partial_x \delta \rho_1 \rangle + \langle \delta \rho_1 \partial_x^2 \delta \rho_1 \rangle] \tilde{m} + g_Q \langle \partial_x \delta \rho_1 \partial_x \delta m_1 \rangle \right]. \end{aligned} \quad (\text{C.56})$$

All that remains to close the renormalized hydrodynamics is to compute the correlators appearing in Eq. C.81.

C.6.1 Computation of correlators near the critical point

In order to compute the correlators $\langle \delta \rho_1^2 \rangle$, $\langle \delta m_1^2 \rangle$, and $\langle \delta \rho_1 \delta m_1 \rangle$ appearing in Eq. C.81 (as well as their associated derivatives), we Fourier transform the linear fluctuating

hydrodynamics in Eqs. C.8-C.9 with modes e^{iqx} to obtain the system of equations

$$\frac{d}{dt} \begin{bmatrix} \delta\rho_1^q \\ \delta m_1^q \end{bmatrix} = \begin{bmatrix} M_{11}^q & M_{12}^q \\ M_{21}^q & M_{22}^q \end{bmatrix} \begin{bmatrix} \delta\rho_1^q \\ \delta m_1^q \end{bmatrix} + \begin{bmatrix} 0 \\ \sqrt{2\rho_0}\eta^q \end{bmatrix} \quad (\text{C.57})$$

where the matrix elements are copied below from Ref. [?], except for M_{21}^q which has a non-reciprocal contribution from Eq. C.51 such that

$$M_{11}^q = -Dq^2 \quad (\text{C.58})$$

$$M_{12}^q = -ivq \quad (\text{C.59})$$

$$M_{21}^q = -ivq + 2\gamma \frac{m_0^3}{\rho_0^3} - m_0 D_Q q^2 \quad (\text{C.60})$$

$$M_{22}^q = -Dq^2 - \alpha - 3\gamma \frac{m_0^2}{\rho_0^2} \quad (\text{C.61})$$

From Eq. C.57, one obtains the following system of equations for the Fourier-space correlators

$$\frac{d}{dt} \langle \delta\rho_1^q \delta\rho_1^{q'} \rangle = \left(M_{11}^q + M_{11}^{q'} \right) \langle \delta\rho_1^q \delta\rho_1^{q'} \rangle + M_{12}^q \langle \delta m_1^q \delta\rho_1^{q'} \rangle + M_{12}^{q'} \langle \delta\rho_1^q \delta m_1^{q'} \rangle \quad (\text{C.62})$$

$$\frac{d}{dt} \langle \delta m_1^q \delta\rho_1^{q'} \rangle = \left(M_{22}^q + M_{11}^{q'} \right) \langle \delta m_1^q \delta\rho_1^{q'} \rangle + M_{21}^q \langle \delta\rho_1^q \delta\rho_1^{q'} \rangle + M_{12}^{q'} \langle \delta m_1^q \delta m_1^{q'} \rangle \quad (\text{C.63})$$

$$\frac{d}{dt} \langle \delta\rho_1^q \delta m_1^{q'} \rangle = \left(M_{22}^{q'} + M_{11}^q \right) \langle \delta\rho_1^q \delta m_1^{q'} \rangle + M_{21}^{q'} \langle \delta\rho_1^q \delta\rho_1^{q'} \rangle + M_{12}^q \langle \delta m_1^q \delta m_1^{q'} \rangle \quad (\text{C.64})$$

$$\frac{d}{dt} \langle \delta m_1^q \delta m_1^{q'} \rangle = \left(M_{22}^q + M_{22}^{q'} \right) \langle \delta m_1^q \delta m_1^{q'} \rangle + M_{21}^q \langle \delta\rho_1^q \delta m_1^{q'} \rangle + M_{21}^{q'} \langle \delta m_1^q \delta\rho_1^{q'} \rangle + \frac{2\rho_0}{L} \delta_{q+q',0}. \quad (\text{C.65})$$

Now I take $q' = -q$ and solve the system of equations in the steady-state such that

$$0 = (M_{11}^q + M_{11}^{-q}) \langle \delta\rho_1^q \delta\rho_1^{-q} \rangle + M_{12}^q \langle \delta m_1^q \delta\rho_1^{-q} \rangle + M_{12}^{-q} \langle \delta\rho_1^q \delta m_1^{-q} \rangle \quad (\text{C.66})$$

$$0 = (M_{22}^q + M_{11}^{-q}) \langle \delta m_1^q \delta\rho_1^{-q} \rangle + M_{21}^q \langle \delta\rho_1^q \delta\rho_1^{-q} \rangle + M_{12}^{-q} \langle \delta m_1^q \delta m_1^{-q} \rangle \quad (\text{C.67})$$

$$0 = (M_{22}^{-q} + M_{11}^q) \langle \delta\rho_1^q \delta m_1^{-q} \rangle + M_{21}^{-q} \langle \delta\rho_1^q \delta\rho_1^{-q} \rangle + M_{12}^q \langle \delta m_1^q \delta m_1^{-q} \rangle \quad (\text{C.68})$$

$$0 = (M_{22}^q + M_{22}^{-q}) \langle \delta m_1^q \delta m_1^{-q} \rangle + M_{21}^q \langle \delta\rho_1^q \delta m_1^{-q} \rangle + M_{21}^{-q} \langle \delta m_1^q \delta\rho_1^{-q} \rangle + \frac{2\rho_0}{L}. \quad (\text{C.69})$$

Directly solving this system of equations yields the following solutions

$$\langle \delta\rho_1^q \delta\rho_1^{-q} \rangle = \frac{\rho_0 v^2}{L(\alpha + 2Dq^2)(\alpha D + D^2q^2 + v^2)} + \mathcal{O}(m_0^2) \quad (\text{C.70})$$

$$\langle \delta\rho_1^q \delta m_1^{-q} \rangle = \frac{-iqD\rho_0 v}{L(\alpha + 2Dq^2)(\alpha D + D^2q^2 + v^2)} - m_0 \frac{q^2 D_Q \rho_0 v^2}{L(\alpha + 2Dq^2)^2(\alpha D + D^2q^2 + v^2)} + \mathcal{O}(m_0^2) \quad (\text{C.71})$$

$$\langle \delta m_1^q \delta m_1^{-q} \rangle = \frac{\rho_0(\alpha D + 2D^2q^2 + v^2)}{L(\alpha + 2Dq^2)(\alpha D + D^2q^2 + v^2)} + \mathcal{O}(m_0^2). \quad (\text{C.72})$$

The solutions here are reported to linear order in m_0 as we assume that we are in the vicinity of the critical point where global order is weak. In the limit $D_Q \rightarrow 0$, these correlators reduce to the result obtained in Ref. [71]. Their real-space counter-parts are straight-forwardly obtained by integrating over all q modes, yielding

$$\langle \delta\rho_1^2 \rangle = \frac{\rho_0 v^2}{2} \frac{\sqrt{\frac{2}{\alpha D} - \frac{1}{\sqrt{\alpha D + v^2}}}}{\alpha D + 2v^2} \quad (\text{C.73})$$

$$\langle \delta\rho_1 \delta m_1 \rangle = -m_0 \frac{D_Q \rho_0 v^2}{8} \frac{3\sqrt{2}\alpha D - 4\sqrt{\alpha D(\alpha D + v^2)} + 2\sqrt{2}v^2}{\sqrt{\alpha D}^{3/2}(\alpha D + 2v^2)^2} + \mathcal{O}(m_0^3) \quad (\text{C.74})$$

$$\langle \delta m_1^2 \rangle = \frac{\rho_0}{2} \frac{\sqrt{2}v^2 + \sqrt{\alpha D(\alpha D + v^2)}}{\sqrt{\alpha D}(\alpha D + 2v^2)}. \quad (\text{C.75})$$

Eqs. C.73 and C.75 are identical to Martin & Tailleur's results in Ref. [?], while Eq. C.74 is only non-zero due to the presence of the non-reciprocal D_Q term. Still remaining is the task of computing the correlators for the fluctuation field gradients

appearing in Eq. C.81. To do so, we use the Fourier-transform definition to write as

$$\lim_{L \rightarrow \infty} \langle f(x)^2 \rangle = \lim_{L \rightarrow \infty} \sum_{q, q'} \langle f^q f^{q'} \rangle e^{iqx+iq'x} = \lim_{L \rightarrow \infty} \sum_q \langle f^q f^{-q} \rangle = \frac{1}{L} \int_{-\infty}^{\infty} \frac{dq}{2\pi} \langle f^q f^{-q} \rangle. \quad (\text{C.76})$$

From this identity, we can also obtain the relations

$$\lim_{L \rightarrow \infty} \langle \partial_x f(x) \partial_x f(x) \rangle = \lim_{L \rightarrow \infty} \sum_{q, q'} (q q') \langle f^q f^{q'} \rangle e^{iqx+iq'x} = \frac{-1}{L} \int_{-\infty}^{\infty} \frac{dq}{2\pi} q^2 \langle f^q f^{-q} \rangle. \quad (\text{C.77})$$

$$\lim_{L \rightarrow \infty} \langle f(x) \partial_x^2 f(x) \rangle = \lim_{L \rightarrow \infty} \sum_{q, q'} (q'^2) \langle f^q f^{q'} \rangle e^{iqx+iq'x} = \frac{1}{L} \int_{-\infty}^{\infty} \frac{dq}{2\pi} q^2 \langle f^q f^{-q} \rangle. \quad (\text{C.78})$$

Therefore, the $\langle \partial_x \delta \rho_1 \partial_x \delta \rho_1 \rangle$ term and $\langle \delta \rho_1 \partial_x^2 \delta \rho_1 \rangle$ term in Eq. C.81 will cancel, and we are left only with the non-linear, truly non-reciprocal term

$$\langle \partial_x \delta \rho_1 \partial_x \delta m_1 \rangle = \frac{-1}{L} \int_{-\infty}^{\infty} \frac{dq}{2\pi} q^2 \langle \delta \rho_1^q \delta m_1^{-q} \rangle \quad (\text{C.79})$$

$$= m_0 D_Q \frac{\rho_0 v^2}{16D^3} \frac{-5\sqrt{2}(\alpha D)^{3/2} - 6v^2\sqrt{2\alpha D} + 8v^2\sqrt{\alpha D + v^2} + 8\alpha D\sqrt{\alpha D + v^2}}{(\alpha D + 2v^2)^2} + \mathcal{O}(m_0^3) \quad (\text{C.80})$$

Collecting the results in Eqs. C.73-C.75 and Eq. C.80 and inserting them into Eq. C.81, the renormalized hydrodynamics become

$$\partial_t \tilde{m} = -\tilde{\alpha} \tilde{m} - \tilde{\gamma} \frac{\tilde{m}^3}{\tilde{\rho}^2} + D \partial_x^2 \tilde{m} - v \partial_x \tilde{\rho} \quad (\text{C.81})$$

where

$$\tilde{\alpha} = \alpha - \frac{\sigma}{\tilde{\rho}^2} \left[3\gamma \langle \delta m_1^2 \rangle - \frac{g_Q}{m_0} \langle \partial_x \delta \rho_1 \partial_x \delta m_1 \rangle \right] \quad (\text{C.82})$$

$$\tilde{\gamma} = \gamma - \frac{\sigma}{\tilde{\rho}^2} \left[3\gamma \langle \delta \rho_1^2 \rangle - \frac{6\gamma}{m_0} \langle \delta \rho_1 \delta m_1 \rangle \right] \quad (\text{C.83})$$

are the renormalized transport coefficients. Below in Fig. C.1 I plot the value of each of the correlators appearing in Eqs. C.82-C.83 as a function of distance to the critical point ($\alpha = 0$). We see that the $\langle \partial_x \delta \rho_1 \partial_x \delta m_1 \rangle$ correlator is sub-dominant to $\langle \delta m_1^2 \rangle$ in the vicinity of the critical point, while $\langle \delta \rho_1 \delta m_1 \rangle$ remains competitive with $\langle \delta \rho_1^2 \rangle$ and thus may affect critical dynamics.

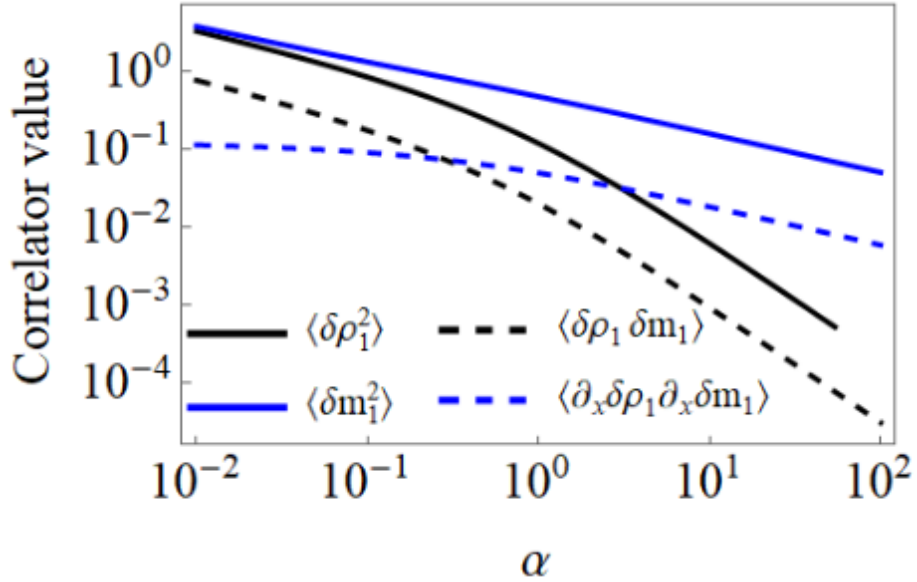


Figure C.1: The correlators in Eqs. C.73 and C.75 are plotted here to leading order in α .

Bibliography

- [1] R. Aditi Simha and Sriram Ramaswamy. *Phys. Rev. Lett.*, 89:058101, Jul 2002.
doi: 10.1103/PhysRevLett.89.058101. URL <https://link.aps.org/doi/10.1103/PhysRevLett.89.058101>.
- [2] R Aditi Simha and Sriram Ramaswamy. Hydrodynamic fluctuations and instabilities in ordered suspensions of self-propelled particles. *Physical review letters*, 89(5):058101, 2002.
- [3] Zsuzsa Ákos, Róbert Beck, Máté Nagy, Tamás Vicsek, and Enikő Kubinyi. Leadership and path characteristics during walks are linked to dominance order and individual traits in dogs. *PLoS computational biology*, 10(1):e1003446, 2014.
- [4] Ricard Alert, Carles Blanch-Mercader, and Jaume Casademunt. Active fingering instability in tissue spreading. *Physical review letters*, 122(8):088104, 2019.
- [5] Igor S Aranson. Bacterial active matter. *Reports on Progress in Physics*, 85(7):076601, 2022.
- [6] Alessandro Attanasi, Andrea Cavagna, Lorenzo Del Castello, Irene Giardina, Tomas S Grigera, Asja Jelić, Stefania Melillo, Leonardo Parisi, Oliver Pohl, Edward Shen, et al. Information transfer and behavioural inertia in starling flocks. *Nature physics*, 10(9):691–696, 2014.

- [7] Youmna Attieh, Andrew G Clark, Carina Grass, Sophie Richon, Marc Pocard, Pascale Mariani, Nadia Elkhatib, Timo Betz, Basile Gurchenkov, and Danijela Matic Vignjevic. Cancer-associated fibroblasts lead tumor invasion through integrin- β 3-dependent fibronectin assembly. *Journal of Cell Biology*, 216(11):3509–3520, 2017.
- [8] Avraham Be’er, Shinji K Strain, Roberto A Hernández, Eshel Ben-Jacob, and E-L Florin. Periodic reversals in *paenibacillus dendritiformis* swarming. *Journal of bacteriology*, 195(12):2709–2717, 2013.
- [9] Eric Bertin, Michel Droz, and Guillaume Grégoire. Boltzmann and hydrodynamic description for self-propelled particles. *Physical Review E*, 74(2):022101, 2006.
- [10] Avraham Be’er, Bella Ilkanaiv, Renan Gross, Daniel B Kearns, Sebastian Heidenreich, Markus Bär, and Gil Ariel. A phase diagram for bacterial swarming. *Communications Physics*, 3(1):66, 2020.
- [11] Arjan Blokland. Reaction time responding in rats. *Neuroscience & Biobehavioral Reviews*, 22(6):847–864, 1998.
- [12] Martin Bock, Amit Kumar Tyagi, Jan-Ulrich Kreft, and Wolfgang Alt. Generalized voronoi tessellation as a model of two-dimensional cell tissue dynamics. *Bulletin of mathematical biology*, 72:1696–1731, 2010.
- [13] Michał J Bogdan and Thierry Savin. Fingering instabilities in tissue invasion: an active fluid model. *Royal Society open science*, 5(12):181579, 2018.
- [14] Alicia Boymelgreen, Jarrod Schiffbauer, Boris Khusid, and Gilad Yossifon. Synthetic electrically driven colloids: a platform for understanding collective behavior in soft matter. *Current Opinion in Colloid & Interface Science*, 60:101603, 2022.

- [15] William G Breed. Evolution of the spermatozoon in muroid rodents. *Journal of Morphology*, 265(3):271–290, 2005.
- [16] Antoine Bricard, Jean-Baptiste Caussin, Nicolas Desreumaux, Olivier Dauchot, and Denis Bartolo. Emergence of macroscopic directed motion in populations of motile colloids. *Nature*, 503(7474):95–98, 2013.
- [17] Shawn P Carey, Alina Starchenko, Alexandra L McGregor, and Cynthia A Reinhart-King. Leading malignant cells initiate collective epithelial cell invasion in a three-dimensional heterotypic tumor spheroid model. *Clinical & experimental metastasis*, 30(5):615–630, 2013.
- [18] Andrea Cavagna, Alessio Cimarrelli, Irene Giardina, Giorgio Parisi, Raffaele Santagati, Fabio Stefanini, and Raffaele Tavarone. From empirical data to inter-individual interactions: unveiling the rules of collective animal behavior. *Mathematical Models and Methods in Applied Sciences*, 20(supp01):1491–1510, 2010.
- [19] Andrea Cavagna, Alessio Cimarrelli, Irene Giardina, Giorgio Parisi, Raffaele Santagati, Fabio Stefanini, and Massimiliano Viale. Scale-free correlations in starling flocks. *Proceedings of the National Academy of Sciences*, 107(26):11865–11870, 2010.
- [20] Hugues Chaté. Dry aligning dilute active matter. *Annual Review of Condensed Matter Physics*, 11(1):189–212, 2020.
- [21] Hugues Chaté, Francesco Ginelli, Guillaume Grégoire, and Franck Raynaud. Collective motion of self-propelled particles interacting without cohesion. *Physical Review E—Statistical, Nonlinear, and Soft Matter Physics*, 77(4):046113, 2008.

- [22] Chong Chen, Song Liu, Xia-qing Shi, Hugues Chaté, and Yilin Wu. Weak synchronization and large-scale collective oscillation in dense bacterial suspensions. *Nature*, 542(7640):210–214, 2017.
- [23] Duxin Chen, Mingyu Kang, and Wenwu Yu. Probabilistic causal inference for coordinated movement of pigeon flocks. *Europhysics Letters*, 130(2):28004, 2020.
- [24] Qiu-shi Chen, Aurelio Patelli, Hugues Chaté, Yu-qiang Ma, and Xia-qing Shi. Fore-aft asymmetric flocking. *Physical Review E*, 96(2):020601, 2017.
- [25] Xiao Chen, Xiang Yang, Mingcheng Yang, and HP Zhang. Dynamic clustering in suspension of motile bacteria. *Europhysics Letters*, 111(5):54002, 2015.
- [26] Oleksandr Chepizhko, David Saintillan, and Fernando Peruani. Revisiting the emergence of order in active matter. *Soft Matter*, 17(11):3113–3120, 2021.
- [27] Steven J Chisolm, Emily Guo, Vignesh Subramaniam, Kyle D Schulze, and Thomas E Angelini. Transitions between cooperative and crowding-dominated collective motion in non-jammed mdck monolayers. *Cells & Development*, page 203989, 2024.
- [28] Yen-Liang Chou, Rylan Wolfe, and Thomas Ihle. Kinetic theory for systems of self-propelled particles with metric-free interactions. *Physical Review E*, 86(2):021120, 2012.
- [29] Miles Cranmer, Alvaro Sanchez Gonzalez, Peter Battaglia, Rui Xu, Kyle Cranmer, David Spergel, and Shirley Ho. Discovering symbolic models from deep learning with inductive biases. *Advances in neural information processing systems*, 33:17429–17442, 2020.

- [30] Adama Creppy, Olivier Praud, Xavier Druart, Philippa L Kohnke, and Franck Plouraboué. Turbulence of swarming sperm. *Physical Review E*, 92(3):032722, 2015.
- [31] Lokrshi Prawar Dadhichi, Jitendra Kethapelli, Rahul Chajwa, Sriram Ramaswamy, and Ananyo Maitra. Nonmutual torques and the unimportance of motility for long-range order in two-dimensional flocks. *Physical Review E*, 101(5):052601, 2020.
- [32] Ingrid David, Philippa Kohnke, Gilles Lagriffoul, Olivier Praud, Franck Plouraboué, Pierre Degond, and Xavier Druart. Mass sperm motility is associated with fertility in sheep. *Animal reproduction science*, 161:75–81, 2015.
- [33] Zachary S Dean, Nima Jamilpour, Marvin J Slepian, and Pak Kin Wong. Decreasing wound edge stress enhances leader cell formation during collective smooth muscle cell migration. *Acs Biomaterials Science & Engineering*, 5(8):3864–3875, 2019.
- [34] Knut Drescher, Jörn Dunkel, Luis H Cisneros, Sujoy Ganguly, and Raymond E Goldstein. Fluid dynamics and noise in bacterial cell–cell and cell–surface scattering. *Proceedings of the National Academy of Sciences*, 108(27):10940–10945, 2011.
- [35] Mihir Durve, Arnab Saha, and Ahmed Sayeed. Active particle condensation by non-reciprocal and time-delayed interactions. *The European Physical Journal E*, 41:1–9, 2018.
- [36] Jens Elgeti, Roland G Winkler, and Gerhard Gompper. Physics of microswimmers—single particle motion and collective behavior: a review. *Reports on progress in physics*, 78(5):056601, 2015.

- [37] Begum Erdogan, Mingfang Ao, Lauren M White, Anna L Means, Bryson M Brewer, Lijie Yang, M Kay Washington, Chanjuan Shi, Omar E Franco, Alissa M Weaver, et al. Cancer-associated fibroblasts promote directional cancer cell migration by aligning fibronectin. *Journal of Cell Biology*, 216(11):3799–3816, 2017.
- [38] Michel Fruchart, Ryo Hanai, Peter B Littlewood, and Vincenzo Vitelli. Non-reciprocal phase transitions. *Nature*, 592(7854):363–369, 2021.
- [39] Simon Garcia, Edouard Hannezo, Jens Elgeti, Jean-François Joanny, Pascal Silberzan, and Nir S Gov. Physics of active jamming during collective cellular motion in a monolayer. *Proceedings of the National Academy of Sciences*, 112(50):15314–15319, 2015.
- [40] Daniel Geiß, Klaus Kroy, and Viktor Holubec. Signal propagation and linear response in the delay vicsek model. *Physical Review E*, 106(5):054612, 2022.
- [41] Delphine Geyer, Alexandre Morin, and Denis Bartolo. Sounds and hydrodynamics of polar active fluids. *Nature materials*, 17(9):789–793, 2018.
- [42] Fabio Giavazzi, Chiara Malinverno, Salvatore Corallino, Francesco Ginelli, Giorgio Scita, and Roberto Cerbino. Giant fluctuations and structural effects in a flocking epithelium. *Journal of Physics D: Applied Physics*, 50(38):384003, 2017.
- [43] Francesco Ginelli. The physics of the vicsek model. *The European Physical Journal Special Topics*, 225:2099–2117, 2016.
- [44] Francesco Ginelli and Hugues Chaté. Relevance of metric-free interactions in flocking phenomena. *Physical review letters*, 105(16):168103, 2010.

- [45] Luca Giuggioli, Thomas J McKetterick, and Marc Holderied. Delayed response and biosonar perception explain movement coordination in trawling bats. *PLoS computational biology*, 11(3):e1004089, 2015.
- [46] Luis Gómez-Nava, Richard Bon, and Fernando Peruani. Intermittent collective motion in sheep results from alternating the role of leader and follower. *Nature Physics*, 18(12):1494–1501, 2022.
- [47] Robert Großmann, Pawel Romanczuk, Markus Bär, and Lutz Schimansky-Geier. Vortex arrays and mesoscale turbulence of self-propelled particles. *Physical review letters*, 113(25):258104, 2014.
- [48] Daniel R Gurevich, Matthew R Golden, Patrick AK Reinbold, and Roman O Grigoriev. Learning fluid physics from highly turbulent data using sparse physics-informed discovery of empirical relations (spider). *Journal of Fluid Mechanics*, 996:A25, 2024.
- [49] Brian M Haines, Andrey Sokolov, Igor S Aranson, Leonid Berlyand, and Dmitry A Karpeev. Three-dimensional model for the effective viscosity of bacterial suspensions. *Physical Review E—Statistical, Nonlinear, and Soft Matter Physics*, 80(4):041922, 2009.
- [50] Seth Haney, Jessica Konen, Adam I Marcus, and Maxim Bazhenov. The complex ecosystem in non small cell lung cancer invasion. *PLoS computational biology*, 14(5):e1006131, 2018.
- [51] Sebastian Heidenreich, Jörn Dunkel, Sabine HL Klapp, and Markus Bär. Hydrodynamic length-scale selection in microswimmer suspensions. *Physical Review E*, 94(2):020601, 2016.
- [52] Viktor Holubec, Daniel Geiss, Sarah AM Loos, Klaus Kroy, and Frank Cichos.

- Finite-size scaling at the edge of disorder in a time-delay vicsek model. *Physical review letters*, 127(25):258001, 2021.
- [53] Kristin A Hook and Heidi S Fisher. Methodological considerations for examining the relationship between sperm morphology and motility. *Molecular reproduction and development*, 87(6):633–649, 2020.
- [54] Junxiang Huang, Herbert Levine, and Dapeng Bi. Bridging the gap between collective motility and epithelial–mesenchymal transitions through the active finite voronoi model. *Soft Matter*, 19(48):9389–9398, 2023.
- [55] Cristián Huepe and Maximino Aldana. Intermittency and clustering in a system of self-driven particles. *Physical review letters*, 92(16):168701, 2004.
- [56] Kenta Ishimoto and Eamonn A Gaffney. Hydrodynamic clustering of human sperm in viscoelastic fluids. *Scientific Reports*, 8(1):15600, 2018.
- [57] Junichiro Iwasawa, Daiki Nishiguchi, and Masaki Sano. Algebraic correlations and anomalous fluctuations in ordered flocks of janus particles fueled by an ac electric field. *Physical Review Research*, 3(4):043104, 2021.
- [58] Katherine A Jones, John R Krebs, and Mark J Whittingham. Heavier birds react faster to predators: individual differences in the detection of stalking and ambush predators. *Behavioral Ecology and Sociobiology*, 63:1319–1329, 2009.
- [59] Hamid Karani, Gerardo E Pradillo, and Petia M Vlahovska. Tuning the random walk of active colloids: From individual run-and-tumble to dynamic clustering. *Physical review letters*, 123(20):208002, 2019.
- [60] Mehran Kardar. *Statistical physics of fields*. Cambridge University Press, 2007.
- [61] Nazanin Karimnia, Amy L Wilson, Emma Green, Amelia Matthews, Thomas W Jobling, Magdalena Plebanski, Maree Bilandzic, and Andrew N Stephens.

- Chemoresistance is mediated by ovarian cancer leader cells in vitro. *Journal of Experimental & Clinical Cancer Research*, 40:1–13, 2021.
- [62] J Konen, E Summerbell, B Dwivedi, K Galior, Y Hou, L Rusnak, A Chen, J Saltz, W Zhou, LH Boise, et al. Image-guided genomics of phenotypically heterogeneous populations reveals vascular signalling during symbiotic collective cancer invasion. *Nature communications*, 8(1):15078, 2017.
- [63] J.H. Koziol and C.L. Armstrong. Manual for breeding soundness examination of bulls. *Soc Theriogenology*, pages 1–147, 2018.
- [64] Yau Meng Kuan, Nurul Atikah Zuhairi, FA Manan, Victor Feizal Knight, and Rokiah Omar. Visual reaction time and visual anticipation time between athletes and non-athletes. *Malaysian Journal of Public Health Medicine*, 1:135–141, 2018.
- [65] Rüdiger Kürsten and Thomas Ihle. Dry active matter exhibits a self-organized cross sea phase. *Physical Review Letters*, 125(18):188003, 2020.
- [66] Shao-Zhen Lin, Bo Li, Guang-Kui Xu, and Xi-Qiao Feng. Collective dynamics of cancer cells confined in a confluent monolayer of normal cells. *Journal of Biomechanics*, 52:140–147, 2017.
- [67] Bodong Liu, Yanting Zhu, Zhenye Yang, Helen HN Yan, Suet Yi Leung, and Jue Shi. Deep learning-based 3d single-cell imaging analysis pipeline enables quantification of cell-cell interaction dynamics in the tumor microenvironment. *Cancer Research*, 84(4):517–526, 2024.
- [68] Zhengyang Liu, Wei Zeng, Xiaolei Ma, and Xiang Cheng. Density fluctuations and energy spectra of 3d bacterial suspensions. *Soft Matter*, 17(48):10806–10817, 2021.

- [69] Héctor Matías López, Jérémie Gachelin, Carine Douarche, Harold Auradou, and Eric Clément. Turning bacteria suspensions into superfluids. *Physical review letters*, 115(2):028301, 2015.
- [70] Benoît Mahault, Francesco Ginelli, and Hugues Chaté. Quantitative assessment of the toner and tu theory of polar flocks. *Physical review letters*, 123(21):218001, 2019.
- [71] David Martin, Hugues Chaté, Cesare Nardini, Alexandre Solon, Julien Tailleur, and Frédéric Van Wijland. Fluctuation-induced phase separation in metric and topological models of collective motion. *Physical Review Letters*, 126(14):148001, 2021.
- [72] Vincent A Martinez, Eric Clément, Jochen Arlt, Carine Douarche, Angela Dawson, Jana Schwarz-Linek, Adama K Creppy, Viktor Škultéty, Alexander N Morozov, Harold Auradou, et al. A combined rheometry and imaging study of viscosity reduction in bacterial suspensions. *Proceedings of the National Academy of Sciences*, 117(5):2326–2331, 2020.
- [73] Shradha Mishra, Aparna Baskaran, and M Cristina Marchetti. Fluctuations and pattern formation in self-propelled particles. *Physical Review E—Statistical, Nonlinear, and Soft Matter Physics*, 81(6):061916, 2010.
- [74] Siddhartha Mukherjee, Rahul K Singh, Martin James, and Samridhi Sankar Ray. Anomalous diffusion and lévy walks distinguish active from inertial turbulence. *Physical Review Letters*, 127(11):118001, 2021.
- [75] Ken H Nagai, Yutaka Sumino, Raul Montagne, Igor S Aranson, and Hugues Chaté. Collective motion of self-propelled particles with memory. *Physical review letters*, 114(16):168001, 2015.

- [76] Máté Nagy, Zsuzsa Ákos, Dora Biro, and Tamás Vicsek. Hierarchical group dynamics in pigeon flocks. *Nature*, 464(7290):890–893, 2010.
- [77] Máté Nagy, Gábor Vásárhelyi, Benjamin Pettit, Isabella Roberts-Mariani, Tamás Vicsek, and Dora Biro. Context-dependent hierarchies in pigeons. *Proceedings of the National Academy of Sciences*, 110(32):13049–13054, 2013.
- [78] Reza Nosrati, Amine Driouchi, Christopher M. Yip, and David Sinton. *Nature Commun*, 6:8703, 2015. doi: 10.1038/ncomms9703.
- [79] Aimilia Nousi, Maria Tangen Sjøgaard, Mélanie Audoin, and Liselotte Jauffred. Single-cell tracking reveals super-spreading brain cancer cells with high persistence. *Biochemistry and Biophysics Reports*, 28:101120, 2021.
- [80] Tatiana Omelchenko, Jury M Vasiliev, IM Gelfand, HH Feder, and EM Bonder. Rho-dependent formation of epithelial “leader” cells during wound healing. *Proceedings of the National Academy of Sciences*, 100(19):10788–10793, 2003.
- [81] Charles Packard and Daniel Marc Sussman. Banded phases in topological flocks. *Soft Matter*, 2025.
- [82] Charles R Packard, Shobitha Unnikrishnan, Shiva Phuyal, Soon Hon Cheong, M Lisa Manning, Chih-Kuan Tung, and Daniel M Sussman. Self-organized vortex phases and hydrodynamic interactions in bos taurus sperm cells. *Physical Review E*, 110(1):014407, 2024.
- [83] Fatemeh Pakpour and Tamás Vicsek. Delay-induced phase transitions in active matter. *Physica A: Statistical Mechanics and its Applications*, 634:129453, 2024.
- [84] Antonia Patsialou, Jose Javier Bravo-Cordero, Yarong Wang, David Entenberg, Huiping Liu, Michael Clarke, and John S Condeelis. Intravital multiphoton

- imaging reveals multicellular streaming as a crucial component of in vivo cell migration in human breast tumors. *Intravital*, 2(2):e25294, 2013.
- [85] Daniel JG Pearce, LA Hoogerbrugge, Kristin A Hook, Heidi S Fisher, and Luca Giomi. Cellular geometry controls the efficiency of motile sperm aggregates. *Journal of the Royal Society Interface*, 15(148):20180702, 2018.
- [86] Louisiane Perrin, Elizaveta Belova, Battuya Bayarmagnai, Erkan Tüzel, and Bojana Gligorijevic. Invadopodia enable cooperative invasion and metastasis of breast cancer cells. *Communications Biology*, 5(1):758, 2022.
- [87] Fernando Peruani, Jörn Starruß, Vladimir Jakovljevic, Lotte Søgaard-Andersen, Andreas Deutsch, and Markus Bär. Collective motion and nonequilibrium cluster formation in colonies of gliding bacteria. *Physical review letters*, 108(9):098102, 2012.
- [88] Anton Peshkov, Sandrine Ngo, Eric Bertin, Hugues Chaté, and Francesco Ginelli. Continuous theory of active matter systems with metric-free interactions. *Physical review letters*, 109(9):098101, 2012.
- [89] David M Phillips. Comparative analysis of mammalian sperm motility. *The Journal of cell biology*, 53(2):561–573, 1972.
- [90] Shiva Phuyal, Susan S Suarez, and Chih-Kuan Tung. Biological benefits of collective swimming of sperm in a viscoelastic fluid. *Frontiers in Cell and Developmental Biology*, 10:961623, 2022.
- [91] Lei Qin, Dazhi Yang, Weihong Yi, Huiling Cao, and Guozhi Xiao. Roles of leader and follower cells in collective cell migration. *Molecular Biology of the Cell*, 32(14):1267–1272, 2021.

- [92] Md Hamidur Rahman and Muhammad Shahidul Islam. Investigation of audio-visual simple reaction time of university athletes and non-athletes. *Journal of Advances in Sports and Physical Education*, 4(3):24–29, 2021.
- [93] Sriram Ramaswamy, R Aditi Simha, and John Toner. Active nematics on a substrate: Giant number fluctuations and long-time tails. *Europhysics Letters*, 62(2):196, 2003.
- [94] Arja Ray, Rachel K Morford, Nima Ghaderi, David J Odde, and Paolo P Provenzano. Dynamics of 3d carcinoma cell invasion into aligned collagen. *Integrative biology*, 10(2):100–112, 2018.
- [95] Craig W Reynolds. Flocks, herds and schools: A distributed behavioral model. In *Proceedings of the 14th annual conference on Computer graphics and interactive techniques*, pages 25–34, 1987.
- [96] Ingmar H Riedel, Karsten Kruse, and Jonathon Howard. A self-organized vortex array of hydrodynamically entrained sperm cells. *Science*, 309(5732):300–303, 2005.
- [97] Laila Ritsma, Saskia IJ Ellenbroek, Anoeck Zomer, Hugo J Snippert, Frederic J de Sauvage, Benjamin D Simons, Hans Clevers, and Jacco van Rheenen. *Nature*, 507(7492):362–365, 2014.
- [98] Suropriya Saha, Sriram Ramaswamy, and Ramin Golestanian. Pairing, waltzing and scattering of chemotactic active colloids. *New Journal of Physics*, 21(6):063006, 2019.
- [99] Debarati Sarkar, Gerhard Gompper, and Jens Elgeti. A minimal model for structure, dynamics, and tension of monolayered cell colonies. *Communications Physics*, 4(1):36, 2021.

- [100] Volker Schaller and Andreas R Bausch. Topological defects and density fluctuations in collectively moving systems. *Proceedings of the National Academy of Sciences*, 110(12):4488–4493, 2013.
- [101] Néstor Sepúlveda, Laurence Petitjean, Olivier Cochet, Erwan Grasland-Mongrain, Pascal Silberzan, and Vincent Hakim. Collective cell motion in an epithelial sheet can be quantitatively described by a stochastic interacting particle model. *PLoS computational biology*, 9(3):e1002944, 2013.
- [102] Suraj Shankar, Mark J Bowick, and M Cristina Marchetti. Topological sound and flocking on curved surfaces. *Physical Review X*, 7(3):031039, 2017.
- [103] Rastko Sknepnek and Silke Henkes. Active swarms on a sphere. *Physical Review E*, 91(2):022306, 2015.
- [104] Alexandre P Solon, Jean-Baptiste Caussin, Denis Bartolo, Hugues Chaté, and Julien Tailleur. Pattern formation in flocking models: A hydrodynamic description. *Physical Review E*, 92(6):062111, 2015.
- [105] Carsen Stringer, Tim Wang, Michalis Michaelos, and Marius Pachitariu. *Nature methods*, 18(1):100–106, 2021.
- [106] Takuma Sugi, Hiroshi Ito, Masaki Nishimura, and Ken H Nagai. *C. elegans* collectively forms dynamical networks. *Nature communications*, 10(1):683, 2019.
- [107] Yutaka Sumino, Ken H Nagai, Yuji Shitaka, Dan Tanaka, Kenichi Yoshikawa, Hugues Chaté, and Kazuhiro Oiwa. Large-scale vortex lattice emerging from collectively moving microtubules. *Nature*, 483(7390):448–452, 2012.
- [108] Emily R Summerbell, Janna K Mouw, Joshua SK Bell, Christina M Knippler, Brian Pedro, Jamie L Arnst, Tala O Khatib, Rachel Commander, Benjamin G Barwick, Jessica Konen, et al. Epigenetically heterogeneous tumor cells direct

- collective invasion through filopodia-driven fibronectin micropatterning. *Science Advances*, 6(30):eaaz6197, 2020.
- [109] Yongzheng Sun, Wei Lin, and Radek Erban. Time delay can facilitate coherence in self-driven interacting-particle systems. *Physical Review E*, 90(6):062708, 2014.
- [110] Rohit Supekar, Boya Song, Alasdair Hastewell, Gary PT Choi, Alexander Mietke, and Jörn Dunkel. Learning hydrodynamic equations for active matter from particle simulations and experiments. *Proceedings of the National Academy of Sciences*, 120(7):e2206994120, 2023.
- [111] Daniel M Sussman. cellgpu: Massively parallel simulations of dynamic vertex models. *Computer Physics Communications*, 219:400–406, 2017.
- [112] Daniel M Sussman, JM Schwarz, M Cristina Marchetti, and M Lisa Manning. Soft yet sharp interfaces in a vertex model of confluent tissue. *Physical review letters*, 120(5):058001, 2018.
- [113] Balint Szabo, GJ Szöllösi, B Gönci, Zs Jurányi, David Selmecezi, and Tamás Vicsek. Phase transition in the collective migration of tissue cells: experiment and model. *Physical Review E—Statistical, Nonlinear, and Soft Matter Physics*, 74(6):061908, 2006.
- [114] Klementyna Szwaykowska, Ira B Schwartz, Luis Mier-y Teran Romero, Christopher R Heckman, Dan Mox, and M Ani Hsieh. Collective motion patterns of swarms with delay coupling: Theory and experiment. *Physical Review E*, 93(3):032307, 2016.
- [115] Mingxing Tan and Quoc Le. Efficientnet: Rethinking model scaling for convolutional neural networks. In *International conference on machine learning*, pages 6105–6114. PMLR, 2019.

- [116] Victoria Tarle, Andrea Ravasio, Vincent Hakim, and Nir S Gov. Modeling the finger instability in an expanding cell monolayer. *Integrative Biology*, 7(10):1218–1227, 2015.
- [117] John Toner. Giant number fluctuations in dry active polar fluids: A shocking analogy with lightning rods. *The Journal of chemical physics*, 150(15), 2019.
- [118] John Toner and Yuhai Tu. Long-range order in a two-dimensional dynamical xy model: how birds fly together. *Physical review letters*, 75(23):4326, 1995.
- [119] Peter Torab, Yue Yan, Hironobu Yamashita, Joshua I Warrick, Jay D Raman, David J DeGraff, and Pak Kin Wong. Three-dimensional microtumors for probing heterogeneity of invasive bladder cancer. *Analytical Chemistry*, 92(13):8768–8775, 2020.
- [120] Rémy Torro, Beatriz Díaz-Bello, Dalia El Arawi, Ksenija Dervanova, Lorna Ammer, Florian Dupuy, Patrick Chames, Kheya Sengupta, and Laurent Limozin. Celldetective: an ai-enhanced image analysis tool for unraveling dynamic cell interactions. *bioRxiv*, pages 2024–03, 2024.
- [121] Carolina Trenado, Luis L Bonilla, and Alejandro Martínez-Calvo. Fingering instability in spreading epithelial monolayers: roles of cell polarisation, substrate friction and contractile stresses. *Soft Matter*, 17(36):8276–8290, 2021.
- [122] Yuhai Tu, John Toner, and Markus Ulm. Sound waves and the absence of galilean invariance in flocks. *Physical review letters*, 80(21):4819, 1998.
- [123] Chih-kuan Tung, Florencia Ardon, Anubhab Roy, Donald L Koch, Susan S Suarez, and Mingming Wu. Emergence of upstream swimming via a hydrodynamic transition. *Physical review letters*, 114(10):108102, 2015.

- [124] Chih-kuan Tung, Chungwei Lin, Benedict Harvey, Alyssa G Fiore, Florencia Ardon, Mingming Wu, and Susan S Suarez. Fluid viscoelasticity promotes collective swimming of sperm. *Scientific reports*, 7(1):3152, 2017.
- [125] Kristina Ulicna, Giulia Vallardi, Guillaume Charras, and Alan R. Lowe. Automated deep lineage tree analysis using a bayesian single cell tracking approach. *Frontiers in Computer Science*, 3:92, 2021. ISSN 2624-9898. doi: 10.3389/fcomp.2021.734559. URL <https://www.frontiersin.org/article/10.3389/fcomp.2021.734559>.
- [126] Emma Velterop, Burak Uz Kent, and Jenny Suckale. Safe shelter: a case for prioritizing housing quality in climate adaptation policy by remotely sensing roof tarps in the san francisco bay area. *Earth's Future*, 10(8):e2022EF002789, 2022.
- [127] Tamás Vicsek, András Czirók, Eshel Ben-Jacob, Inon Cohen, and Ofer Shochet. Novel type of phase transition in a system of self-driven particles. *Physical review letters*, 75(6):1226, 1995.
- [128] Samuel A Vilchez Mercedes, Federico Bocci, Herbert Levine, José N Onuchic, Mohit Kumar Jolly, and Pak Kin Wong. Decoding leader cells in collective cancer invasion. *Nature Reviews Cancer*, 21(9):592–604, 2021.
- [129] Ulf von Barth. Basic density-functional theory—an overview. *Physica Scripta*, 2004(T109):9, 2004.
- [130] Haoran Xu and Yilin Wu. Self-enhanced mobility enables vortex pattern formation in living matter. *Nature*, 627(8004):553–558, 2024.
- [131] Sadato Yamanaka and Takao Ohta. Formation and collision of traveling bands in interacting deformable self-propelled particles. *Physical Review E*, 89(1):012918, 2014.

- [132] Ou Yang, Yi Peng, Zhengyang Liu, Chao Tang, Xinliang Xu, and Xiang Cheng. Dynamics of ellipsoidal tracers in swimming algal suspensions. *Physical Review E*, 94(4):042601, 2016.
- [133] Yanjun Yang and Herbert Levine. Leader-cell-driven epithelial sheet fingering. *Physical biology*, 17(4):046003, 2020.
- [134] Yingzi Yang, Feng Qiu, and Gerhard Gompper. Self-organized vortices of circling self-propelled particles and curved active flagella. *Physical Review E*, 89(1):012720, 2014.
- [135] Julia M Yeomans, Dmitri O Pushkin, and Henry Shum. An introduction to the hydrodynamics of swimming microorganisms. *The European Physical Journal Special Topics*, 223(9):1771–1785, 2014.
- [136] Meisam Zaferani and Alireza Abbaspourrad. Biphasic chemokinesis of mammalian sperm. *Physical Review Letters*, 130(24):248401, 2023.
- [137] Steven M Zehnder, Melanie Suaris, Madisonclaire M Bellaire, and Thomas E Angelini. Cell volume fluctuations in mdck monolayers. *Biophysical journal*, 108(2):247–250, 2015.
- [138] He-Peng Zhang, Avraham Be'er, E-L Florin, and Harry L Swinney. Collective motion and density fluctuations in bacterial colonies. *Proceedings of the National Academy of Sciences*, 107(31):13626–13630, 2010.
- [139] Jian Zhang, Kayla F Goliwas, Wenjun Wang, Paul V Taufalele, Francois Bordeleau, and Cynthia A Reinhart-King. Energetic regulation of coordinated leader–follower dynamics during collective invasion of breast cancer cells. *Proceedings of the National Academy of Sciences*, 116(16):7867–7872, 2019.

- [140] Yinong Zhao, Thomas Ihle, Zhangang Han, Cristián Huepe, and Pawel Romanczuk. Phases and homogeneous ordered states in alignment-based self-propelled particle models. *Physical Review E*, 104(4):044605, 2021.